University Of Oxford

Mathematical, Physical and Life Science Division,
Department Of Physics,
Atomic And Laser Physics

2016

D.Phil. Thesis

X-ray Diffraction Studies of Laser-Shocked Crystals

David R. McGonegle

Supervisor: Prof. J.S. Wark

X-ray Diffraction Studies of Laser-Shocked Crystals

David McGonegle
St. Anne's College

Thesis submitted for the Degree of Doctor of Philosophy
Trinity Term 2016

Abstract

When materials are shock compressed, they undergo changes in microstructure that act to relieve the large shear stresses associated with the compression. The plasticity mechanisms that mediate this transition such as slip and twinning remain poorly understood, especially in the case of polycrystals, which make up the majority of real world materials. This work presents a theoretical outline for analysing Debye-Scherrer diffraction experiments under large strains. A method is demonstrated to measure both the components of strain in the normal and transverse directions, as well as crystal orientation using highly textured samples. These theoretical predictions are compared with simulated diffraction patterns from molecular dynamics simulations. This technique is applied to two different experiments on tantalum. The first provides a measurement of the timescale for plastic deformation, which we find similar to comparable experiments in copper, while the second provides the first *in situ* of observation of twinning in shock compressed metal.

Acknowledgements

There are a number of people I would like for helping me with this work. Firstly, I'd like to thank Justin Wark for his patient supervision and guidance throughout my graduate work. I'd also like to thank all members of the Wark group, but in particular Andy Higginbotham who has helped me immensely at the beginning of my scientific career and whose ongoing collaboration is invaluable. My immense thanks goes out to all my collaborators, especially Chris Wehrenberg, Bruce Remington and Despina Milathianaki, without whom the experiments described in this work would not have been possible. I'd like to thank my friends and family, who have helped me through the ups and downs of the last five years. My parents, for their love and support and to Amy, for always being there for me. I am forever grateful.

The author is grateful to the LLNS for support under contract B595954. Use of the Linac Coherent Light Source (LCLS), SLAC National Accelerator Laboratory, is supported by the U.S. Department of Energy, Office of Science, Office of Basic Energy Sciences under Contract No. DE-AC02-76SF00515

Contents

List of Figures

Nomenclature

$\mathbf{a_1}, \mathbf{a_2}, \mathbf{a_3}$	Lattice vectors of the conventional unit cell
$\alpha_{\mathbf{ij}}$	Deformation gradient in the sample coordinate system
$\mathbf{b_1}, \mathbf{b_2}, \mathbf{b_3}$	Lattice vectors of the reciprocal unit cell
$\mathbf{b}$	Burgers vector
B	Bland number
β	Slip direction
C_0	Ambient sound speed
C_{ij}, C_{ijkl}	Elastic stiffness tensor
χ	Angle between the sample normal and incoming x-ray beam
d	Interplanar spacing

$\perp$	Dislocation
ϵ_{ij}	Strain tensor
e_{ij}	Relative displacement tensor
E	Internal energy
F_{ij}	Deformation gradient
$\mathbf{G_{hkl}}$	Reciprocal lattice vector
γ	Shear strain
γ	Lorentz factor
h, k, i, l	Miller-Bravais indices for hexagonal systems
h, k, l	Miller indices in non-hexagonal systems
I	Intensity
$\mathbf{k}$	Wavevector
λ	Wavelength
$\mathbf{n}$	Sample normal
N	Dislocation density
P	Hydrostatic pressure
ϕ	Azimuthal angle
ψ	Angle between the sample normal and the reciprocal lattice vector
$\mathbf{R}$	Rotation matrix

ρ	Density
r	Lattice translation vector
S_{ij}, S_{ijkl}	Elastic compliance tensor
σ_{ij}	Stress tensor
$\sigma_{n,t}$	Stress components in the normal (shock) and transverse directions
θ_B	Bragg angle
τ	Shear stress
U_p	Particle velocity
U_s	Shock velocity
V	Potential
V	Specific volume
bcc	Body-centred cubic
CSPAD	Cornell Stanford Pixel Array Detector
CXI	Coherent X-ray Imaging
DAC	Diamond Anvil Cell
EOS	Equation of state
EAM	Embedded atom model
fcc	Face-centred cubic
FEL	Free Electron Laser

FT	Fourier Transform
hcp	Hexagonal close-packed
HEL	Hugoniot Elastic Limit
LAMMPS	Large-scale Atomic/Molecular Massively Parallel Simulator
LCLS	Linac Coherent Light Source
MD	Molecular dynamics
MEC	Matter in Extreme Conditions
MGPT	Model Generalized Pseudopotential Theory
ODF	Orientational Distribution Function
OR	Orientational Relationship
PASF	Per atom structure factor
VISAR	Velocity System for Any Reflector
XFEL	X-ray Free Electron Laser

CHAPTER 1

Introduction

1.1 Historical Context

1.1.1 Shock compression

The initial theoretical framework behind the theory of shocks can be traced back to as early as the late 19$^{\mathrm{th}}$ century. Studies by William Rankine [2] in 1870 and Pierre Henri Hugoniot [3] in 1887 into discontinuities in fluid flows later led to the creation of the Rankine-Hugoniot equations, which describe the evolution of shock waves. These equations can also be used to find the locus of states (of pressure, density and temperature) achievable via compression of a material by a single shock. While originally derived for fluids, these equations are also applicable for shock within solids, when the shock strength exceeds the yield strength and the material begins to plastically flow.

The first concerted effort to experimentally study shocks in solids began in the 1940s and 1950s, with the advent of the Second World War. In particular, the Manhattan Project required a detailed study of material response during an implosion. This led to the development of explosive lenses, a type of shaped explosive charge, which were used to create higher pressure states than achievable by static techniques of the time. Early experiments by Walsh demonstrated pressures of up to 50 GPa using this method [4] and was used to obtain equation of state (EOS) data in a number of different metals [5]. These experiments were limited in the ultimate pressure they could achieve, as the particle velocity reached could not exceed the detonation velocity of the explosives used ($\sim 5\,\mathrm{km/s}$). The development of light gas guns provided a complementary method for obtaining EOS data [6]. These use an explosive charge to drive a piston into a tube containing a light gas (usually H or He). The compressed gas will then rupture a diaphragm at the desired pressure and accelerate a flyer plate up to 15 km/s, allowing for pressures up to 1 TPa to be reached. The late 1960s and early 1970s saw the use of laser compression to drive shocks. Many of these high power last systems were initially designed for inertial confinement fusion research, with shocks created as a by-product of the laser-matter interaction. By modifying the intensity of the drive laser it is possible to control the pressure of the shocked sample, with the relationship between laser intensity (I_L) and drive pressure (P) found experimentally to scale as $P \sim {I_L}^{\frac{2}{3}}$ [7]. Laser ablation of solid targets has been used to create pressure states from 10 GPa up to 5 TPa [8]. The relatively fast rise times of laser pulses result in orders of magnitude higher strain rate than are achievable on gas guns, allowing for the study of material response in these extreme conditions. The use of lasers also saw the development of diagnostics such as the Velocity System for Any Reflector (VISAR), which provided time-resolved rear surface velocity measurements and has remained a key diagnostic of the field [9]. This is often used in conjunction with EOS data to provide a measurement of the sample pressure.

1.1.2 Short-pulse sources

The use of high power lasers also sparked the generation of new bright x-ray sources with pulse lengths short enough to probe shocked states. The first work using a flash x-ray source to diagnose shock compressed samples was undertaken by Johnson in 1970 [10], and was used to produce the first evidence that solids remained crystalline under shock compression [11, 12]. The desire for diagnostics for ICF experiments led to the development of a number of laser plasma sources, which were bright enough to record single-shot diffraction but had pulse lengths as short as 100 ps [13, 14]. Later work by Wark pioneered the use of these laser plasma x-ray sources for the use of studying shocked samples via *in situ* diffraction [15, 16], providing measurements of material response on the lattice level. These experiments used a quasi-monochromatic source with a single crystal target and concentrated on a single diffraction line. A later extension of this work using a wide angle detector to record multiple reflections was made by Kalantar [17, 18]. More recently, the advent X-ray Free Electron Lasers (XFELs), such as the Linac Coherent Light Source (LCLS) at SLAC National Accelerator Laboratory has resulted in a dramatic improvement in x-ray sources for diffraction experiments. These machines offer extremely bright, tuneable, hard x-ray pulses perfect for *in situ* diffraction studies and have already been used in a number of dynamic compression experiments [1, 19, 20].

1.1.3 Deformation mechanisms at high strain rates

Different methods of compression will not necessarily result in the same material response, even if the pressures attained are the same. Many diamond anvil cell (DAC) experiments use a pressure transmitting medium to ensure the sample is compressed hydrostatically. However, planar shock compression experiments result in uniaxial compression of the sample, resulting in the build up of high shear stresses that are relieved either by plastic flow or the onset of a phase transition.

Such a phase transition was discovered in iron by Walsh and Bancroft in the 1950s [21, 22]. They postulated that wave splitting in shock experiments was due to the presence of a phase transition at 13 GPa [21, 22]. Later static work by Davison confirmed the $\alpha-\epsilon$ (body centred cubic to hexagonal close-packed) phase transition at the same pressure. This was a particularly important result given the geophysical importance of iron's role in the Earth's core, and also demonstrated that shock compression could complement the more established field of static research. In the 2000s, molecular dynamics simulations by Kadau [23], and then experimental studies using *in situ* diffraction by Kalantar [17], demonstrated that both the static and shocked phases where in fact the same. This was later extended to polycrystalline samples, both in simulations by Kadau [24] and experimentally by Hawreliak [25]. This experiment also sought to measure the residual shear strain in HCP iron as a function of a pressure. While materials shocked above their strength will start to deform plastically, they retain some resistance to this deformation known as material strength that prevents them returning to the hydrostat. However, this deviation from hydrostatic compression is usually small, making it difficult to observe using laser plasma x-ray sources due to their reasonably wide bandwidth. The transition from

1D to 3D compression via plastic deformation has been extensively studying via molecular dynamics simulations, and the advent of 4th generation light sources has allowed this phenomenon to be captured in Cu through the use of femtosecond diffraction [1]. Other work using single crystal copper has observing rotation of the crystal lattice and related their direction and magnitude to dislocation glide along certain slip systems [26]. However, these techniques have so far not been used on polycrystalline samples. Lastly, a large amount of work has been dedicated to understanding body-centred cubic (BCC) materials such as tantalum owing to their multiple competing plasticity mechanisms and inhibited dislocation mobility compared to face-centred cubic (FCC) materials like copper. However, most existing *in situ* diffraction work investigating plasticity in Ta has concentrated on single crystals [27, 28]. There is, therefore, an interest in extending these studies to polycrystalline samples. The techniques outlined in the thesis describe a way of accessing this information and provide significant advances in the understanding of material response in shocked polycrystals.

1.2 Structure of thesis and role of the author

As with most scientific research, the work contained within this thesis is a collaborative effort. The purpose of this section is to provide an outline of the work presented in each chapter and to clarify the contributions of the author. Work performed by other researchers in deriving these results will be clearly referenced or explicitly labelled.

Chapter 2 gives an outline of the relevant background theory, split into the following sections: theory of shock waves, crystal structure, x-ray diffraction, molecular dynamics simulations and x-ray free electron lasers. The theory covered is drawn from a variety of sources and the relevant authors are clearly identified.

Chapter 3 describes the theory of diffraction from polycrystals under an arbitrary strain tensor. This work was developed jointly between the author and Andrew Higginbotham and is published in Journal of Applied Physics [29]. The theoretical predictions are visualised using the LP-Diffract code, written by Andrew Higginbotham.

Chapter 4 provides a description of the theory of diffraction from highly textured polycrystals under uniaxial compression and is published in Journal of Applied Physics [30]. We demonstrate how azimuthal variations in intensity around the Debye-Scherrer ring can be used to gain information about lattice orientation. This technique is applied to simulations of the α–ϵ phase transition in iron, the α–ω transition in titanium, and deformation due to twinning in tantalum. The simulations and theoretical predictions are the work of the author, while the FT rotation code is the work of Andrew Higginbotham.

Chapter 5 outlines an experiment undertaken to find the plastic relaxation time in Ta. This experiment was led by Despina Milathianaki, while the analysis is the work of the author.

Chapter 6 outlines an experiment to measure the twin fraction of shock compressed Ta as a function of pressure. This experiment was planned jointly between Chris Wehrenberg and the author, while the analysis has been a joint effort by the author Chris Wehrenberg, Andrew Higginbotham, Marcin Sliwa, Rob Rudd and Bruce Remington.

Chapter 7 provides an overview of the results and suggests possible areas for future work.

CHAPTER 2

Background Theory

This section gives a brief overview of the theory underpinning the work within this thesis. For a more comprehensive introduction, the reader is referred to one of the several textbooks on solid state physics [31, 32, 33, 34, 35, 36, 37].

2.1 Shock waves

For almost all materials, sound speed increases as a function of pressure. As a result, when a disturbance occurs in a medium, the disturbance front will steepen up, as the higher amplitude regions of the front will travel faster and catch up to the lower amplitude regions. The result is a shock wave, defined as a discontinuity in pressure, temperature and density.

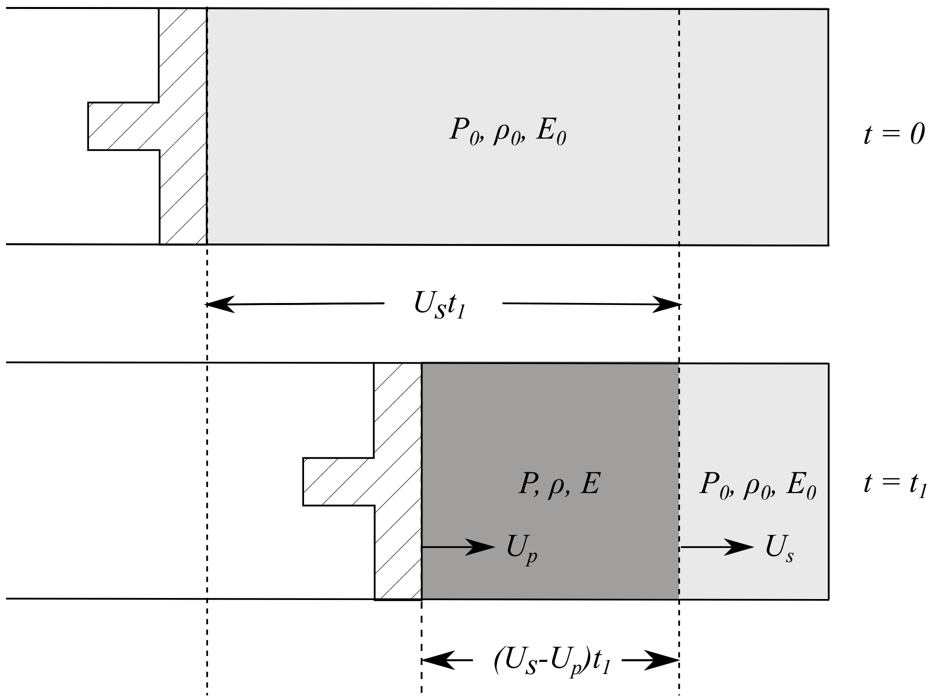

Figure 2.1: An idealised piston moving into a compressible fluid.

2.1.1 The Rankine-Hugoniot equations

The equations governing the behaviour of shock waves are known as the Rankine-Hugoniot equations, which are valid in shocks in fluids and in solids in which their stress exceeds their yield strength. To understand how these equations come about, we can consider a cylinder of cross-sectional area A, containing a compressible fluid of density ρ_0 being pushed on by a piston (Figure 2.1). At $t = 0$ the piston begins moving at U_p towards the fluid, generating a shock front moving at U_s. After a time t_1, a region of compressed fluid of density ρ of length $(U_s - U_p)t_1$ is formed in front of the piston. We can now consider how mass, momentum and energy are conserved. Firstly, the mass in the compressed region must be equal to that of the uncompressed region of length $U_s t_1$.

$$\rho_0 U_s t_1 A = \rho(U_s - U_p) t_1 A, \tag{2.1}$$

$$\rho_0 U_s = \rho(U_s - U_p). \tag{2.2}$$

We can also equate the change in momentum of the compressed region to the impulse provided by the piston. The piston accelerates the compressed region of $\rho_0 U_s t_1 A$ to a velocity U_p as a results of experiencing a net force of $(P - P_0)A$ for a time of t_1. We therefore find–

$$\rho_0 U_s t_1 A U_p = (P - P_0) A t_1, \tag{2.3}$$

$$\rho_0 U_s U_p = (P - P_0). \tag{2.4}$$

Lastly, we consider the change in energy. The work done by the piston will be equal to the change in total energy of the system, that is the change in kinetic and internal energy. This work will be the product of the velocity of the piston and the pressure it applies. The kinetic energy of the shocked region is given by $\frac{1}{2}\rho_0 U_s {U_p}^2 A t_1$. If the internal energy per unit mass of the compressed region is given by E, the change in internal energy will be $\rho_0 U_s (E - E_0) A t_1$. Thus we have–

$$P U_s A t_1 = \frac{1}{2}\rho_0 U_s {U_p}^2 A t_1 + \rho_0 U_s (E - E_0) A t_1, \tag{2.5}$$

$$P U_p = \frac{1}{2}\rho_0 U_s {U_p}^2 + \rho_0 U_s (E - E_0). \tag{2.6}$$

By substituting Equations 2.2 and 2.4 into 2.6, we get–

$$E - E_0 = \frac{1}{2}(P + P_0)(V_0 - V), \tag{2.7}$$

where V is $1/\rho$. The set of Equations 2.2, 2.4, and 2.7 are known as the Rankine-Hugoniot equations [38] or the Rankine-Hugoniot jump conditions.

2.1.2 The Hugoniot curve

The Rankine-Hugoniot equations provide three relationships between five thermodynamic variables: pressure (P), particle velocity (U_p), shock velocity (U_s), specific volume (V), and energy (E). Therefore if we want to find how all the parameters depend on any one of them, an extra relationship is needed. This is usually expressed as an equation relating the shock and particle velocities, and is known as the equation of state (EOS), and is material dependent. For most metals, the EOS can be well approximated as a linear relationship, and is valid over a wide range of pressures. We therefore have–

$$U_s = C_0 + S_1 U_p, \tag{2.8}$$

where S_1 is an experimentally determined constant and C_0 is the sound speed at zero pressure. By combining the conservation equations and the EOS, we can find the relationship between pressure and specific volume, known as the Hugoniot. The Hugoniot describes the locus of all points in P-V space which are possible to reach with a single shock. Rather than a material travelling along the line during a shock until it reaches its peak pressure, it will instead move discontinuously from its initial to its final point on the Hugoniot. The theoretical line which joins these two points is called the Rayleigh line, and by rearranging Equations 2.2 and 2.4, we can find its gradient as–

$$\frac{P - P_0}{V - V_0} = -{\rho_0}^2 {U_s}^2. \tag{2.9}$$

We see from Equation 2.9 that at higher pressures the shock speed will

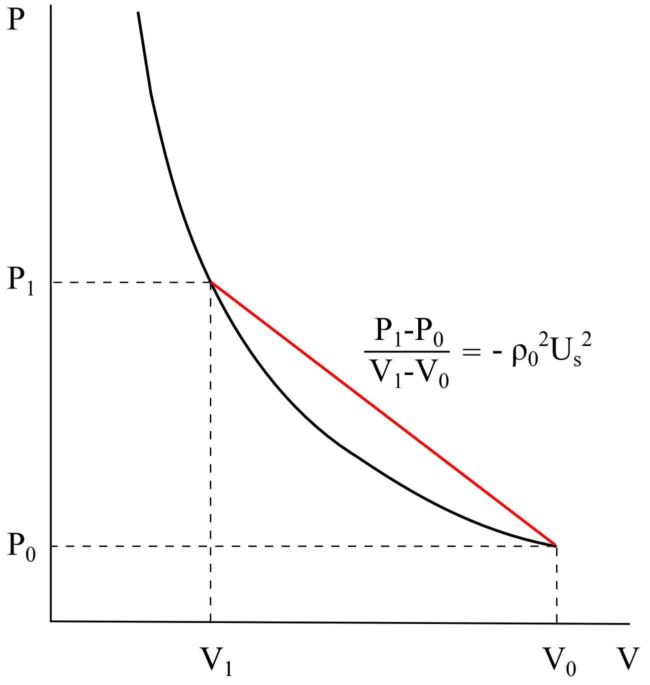

Figure 2.2: The Hugoniot curve in P-V space, shown in black. The Rayleigh line is also shown in red, connecting the initial and final states.

be higher, resulting in a steeper negative gradient for the Rayleigh line, meaning we get a concave Hugoniot curve. By combining the conservation equations with the EOS, we can obtain U_s as a function of V, C_0 and S_1–

$$U_s = \frac{C_0 V_0}{V_0 - S_1(V_0 - V_1)}. \tag{2.10}$$

By substituting Equation 2.10 into 2.9, and noting $\rho = 1/V$ we can obtain pressure as a function of volume–

$$P - P_0 = \frac{{C_0}^2(V_0 - V_1)}{(V_0 - S_1(V_0 - V_1))^2}, \tag{2.11}$$

and this relationship is shown in Figure 2.2. Plots of pressure versus another variable, such as particle velocity, are often also referred to as Hugoniots. It should be noted that Equation 2.11 describes a series of curves in P-V space, since P_0 does not necessarily have to be at ambient pressure. Where this is the case, the curve is called the principal Hugoniot. However, in the case of a double shock, a secondary Hugoniot will describe the reshocked state.

2.1.3 Real shock waves in solids

The theoretical treatment above is valid for fluids which do not support shear stresses. However real materials initially deform elastically until the hydrostatic stress exceeds the sample's flow stress. Below this stress, known as the Hugoniot Elastic Limit (HEL), materials only deform elastically by compressing uniaxially. However, above this point, materials begin to deform plastically, acting to reduce their shear stress and returning towards a hydrostatic state. Upon the onset of plastic deformation, energy is used to perform plastic work within the sample, thus the compressed region must

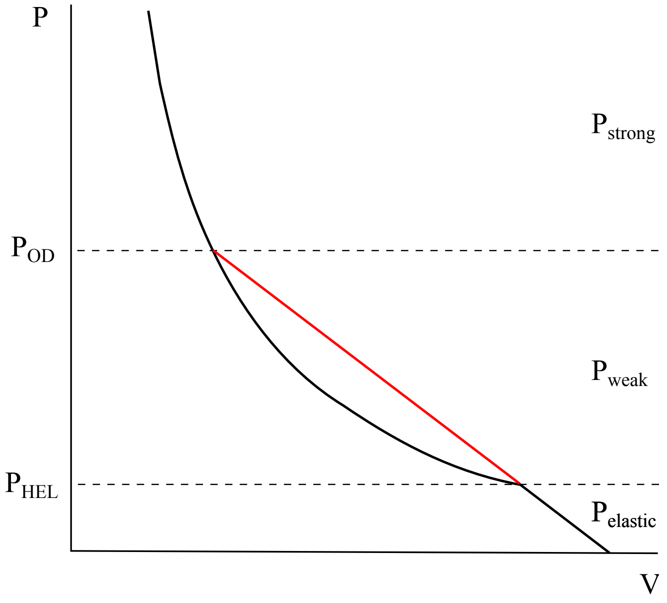

Figure 2.3: A schematic of the Hugoniot for a solid material. Since a shock will become overdriven when the plastic and elastic waves have the same shock speed, this means the Rayleigh line for P_{OD} can be found by extending the elastic part of the Hugoniot. The pressures P_{HEL} and P_{OD} are the boundaries which separate the three types of shock: elastic, weak and strong.

have less kinetic energy and the shock slows down. From Equation 2.9, we see that if there is a discontinuity in the shock velocity, there must also be a sharp change in the gradient of the Hugoniot. However, in a shocked material, the shock velocity increases as a function of pressure, so there must be a pressure at which the plastic wave will have the same shock velocity as the elastic wave. At this pressure the sample is said to be "overdriven". Since both waves will have the same shock velocity, Equation 2.9 shows they must have a Rayleigh line with the same gradient. Thus it is possible to find the overdriven pressure (P_{OD}) by extending the Rayleigh line to the HEL until it crosses the Hugoniot again, shown in Figure 2.3. As a result, there are three different regions of pressure each with a different physical behaviour. While $P < P_{\mathrm{HEL}}$, the material exhibits a single elastic wave. For $P_{\mathrm{HEL}} < P < P_{\mathrm{OD}}$, the elastic wave will have a higher velocity than the plastic wave, resulting in a splitting of the wave profile into an elastic wave (known as an elastic precursor), followed by a slower plastic wave. In this regime, the shocks are known as weak. Lastly, if $P > P_{\mathrm{OD}}$, known as the strong shock regime, the plastic wave would be faster than an elastic wave, and so the sample only exhibits a single plastic wave. The profiles of the three different types of waves are shown in Figure 2.4.

These wave profiles are slightly oversimplified, as many factors can affect the shape of the profile. The length of the plateau region is controlled by the duration of the applied drive pulse in a laser shock experiment, or by the thickness of the impactor plate in an impact experiment. Additionally, a number of materials undergo rapid polymorphic phase transitions [39, 22, 40, 41]. These phase transitions also result in an abrupt change in the shock velocity of the sample, thus creating a splitting of the wave profile, and this technique has been used to identify phase transitions in velocimetry data.

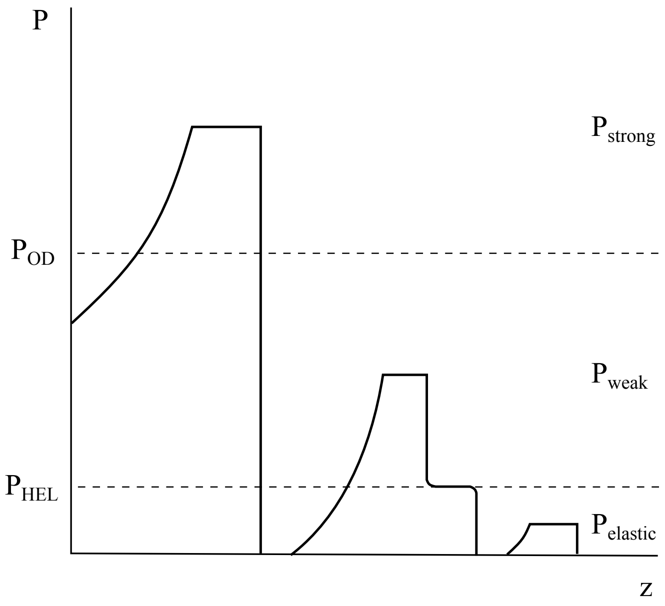

Figure 2.4: Simplified versions of the wave profiles for elastic, weak and strong shocks, travelling from left to right. For the case of weak shocks, the splits into a faster elastic precursor and a slower plastic wave. Each profile consists of a sharp rise, a flat plateau region, and then slow release back to ambient pressure. For the case of weak shocks, there is an additional elastic precursor that runs out in front of the main plastic wave.

A shock is said to be steady if the shape if its wave profile does not change as a function of time. A shock is assumed to have reached a steady state by the time it traverses a sample if it meets the Bland condition–

$$B = \frac{3LS_1\dot{\epsilon}}{8C_0} \geq 1, \tag{2.12}$$

where L is the sample thickness, C_0 and S_1 are coefficients in a linear EOS, as defined in Equation 2.8 and $\dot{\epsilon}$ is the strain rate. It has been experimentally shown for a wide range of materials that strain rate scales with peak pressure to the fourth power, and this is known as the Swegle-Grady relation [42]–

$$\dot{\epsilon} = kP^4, \tag{2.13}$$

where k is an experimentally measured constant. By substituting Equation 2.13 into 2.12 we can obtain the Bland condition in terms of pressure. For the parameters of tantalum ($C_0 = 3.414\,\mu\text{m/ns}$, $S = 1.2$, $k = 27.34\,\text{s}^{-1}\text{GPa}^{-4}$) at 100 GPa, the Bland condition is met for targets over 3 μm, demonstrating that steady shocks can be achieved in thin foil targets with laser drives of a couple of nanoseconds duration [28]. In general weak shocks will not be steady, since the elastic precursor will be travelling faster than the plastic wave and thus the distance between the two shock fronts will grow over time. However, be treating each of the waves separately, they can individually be thought of as steady.

2.2 Crystal Structure

2.2.1 Bravais Lattices

Crystals are formed of a series of one or more atoms repeated at each point of a periodic array known as a lattice. While these repeated units may have a different symmetry to the crystal as a whole, the Bravais lattice is used to describe the underlying symmetry of the periodic structure, independent of what the repeat units might be. The (three-dimensional) Bravais lattice can therefore be defined as the all the position vectors $\mathbf{R}$ that can be written as–

$$\mathbf{R} = h\mathbf{a_1} + k\mathbf{a_2} + l\mathbf{a_3}, \tag{2.14}$$

where $\mathbf{a_1}$, $\mathbf{a_2}$ and $\mathbf{a_3}$ are three non-coplanar vectors, known as primitive vectors and h, k and l take integer values. This definition means that our choice of primitive vectors is somewhat arbitrary, and therefore although many lattices will have an obvious choice of primitive vectors, any set of non-coplanar vectors can be chosen as primitive vectors (Figure 2.5 shows two different choices).

Any region that when transposed by all the vector in a Bravais lattice exactly tessellate is called a primitive unit cell. Usually, the most obvious choice for the primitive unit cell is the parallelepiped (or parallelogram in two dimensions). However, this is not the only choice, and other primitive unit cells, such as the Weigner-Seitz cell (shown in Figure 2.6b), are sometimes used. This cell is constructed by finding the volume bounded by planes (or in this case lines) that bisect a lattice point and its nearest neighbours. Each primitive unit cell will contain exactly one lattice point and will have a volume of $a_1 \cdot (a_2 \times a_3)$. It can often be more convenient to use a larger

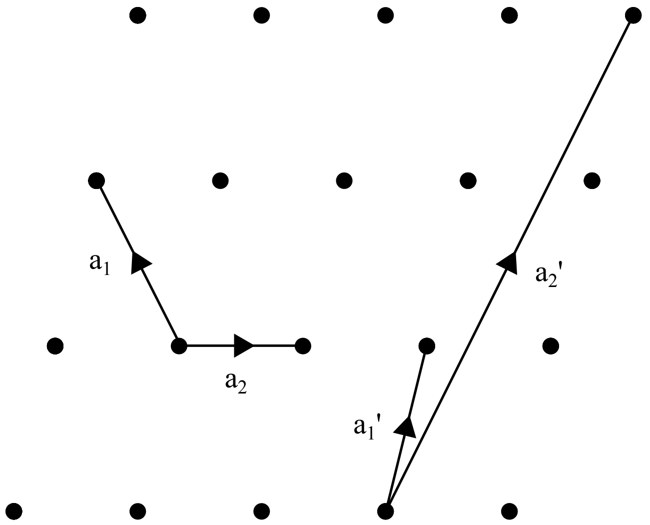

Figure 2.5: A two-dimensional Bravais lattice. Two different choices of primitive vectors are shown.

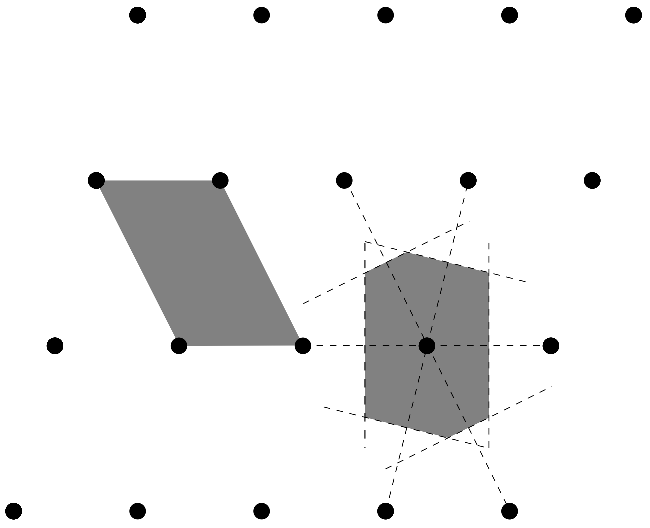

Figure 2.6: Two different choices of primitive unit cell. Cell (a) shows a parallelogram, with each of the corners contributing so that the total cell encompasses a single lattice point. Cell (b) is a Weigner-Seitz cell, with a lattice point at its centre. However, any tessellating cell that contains a single lattice point is a primitive cell.

unit cell, known as a conventional unit cell, which contains more than one lattice point. For the case of bcc and fcc materials, the conventional cell is cubic, containing two and four lattice points respectively.

Any crystal can be described by its underlying Bravais lattice, as well as the arrangement of the repeated units at each lattice point. This repeated structure is known as the crystal basis, and a crystal can be thought of as the convolution of a basis with a lattice. It can be beneficial to describe the Bravais lattice using a non-primitive unit cell. This is often used to emphasise a particular symmetry of the crystal. For example, both fcc and bcc materials are usually described as a simple cubic lattice spanned by the primitive vectors $a\hat{\mathbf{x}}$, $a\hat{\mathbf{y}}$, and $a\hat{\mathbf{z}}$, with a two-point and four-point basis respectively–

$$\mathbf{0}, \qquad \frac{a}{2}(\hat{\mathbf{x}}+\hat{\mathbf{y}}+\hat{\mathbf{z}}) \qquad (bcc) \tag{2.15}$$

$$\mathbf{0}, \qquad \frac{a}{2}(\hat{\mathbf{x}}+\hat{\mathbf{y}}), \qquad \frac{a}{2}(\hat{\mathbf{y}}+\hat{\mathbf{z}}), \qquad \frac{a}{2}(\hat{\mathbf{z}}+\hat{\mathbf{x}}) \qquad (fcc). \tag{2.16}$$

Another common structure is hexagonal close-packed (hcp). This structure has hexagonal symmetry and is therefore often represented as simple hexagonal lattice with a three-point basis–

$$\mathbf{a_1} = [a, 0, 0], \qquad \mathbf{a_2} = \left[-\frac{a}{2}, \frac{\sqrt{3}a}{2}, 0\right], \qquad \mathbf{a_3} = [0, 0, c] \tag{2.17}$$

$$\mathbf{0}, \qquad \frac{2}{3}\mathbf{a_1} + \frac{1}{3}\mathbf{a_2} + \frac{1}{2}\mathbf{a_3}, \qquad \frac{1}{3}\mathbf{a_1} + \frac{2}{3}\mathbf{a_2} + \frac{1}{2}\mathbf{a_3} \qquad (hcp). \tag{2.18}$$

2.2.2 Directions and planes

It can be useful to define particular directions and planes within a crystal. Lattice directions are specified using integer multiples of primitive vectors and is written as the three integers contained within square brackets. For

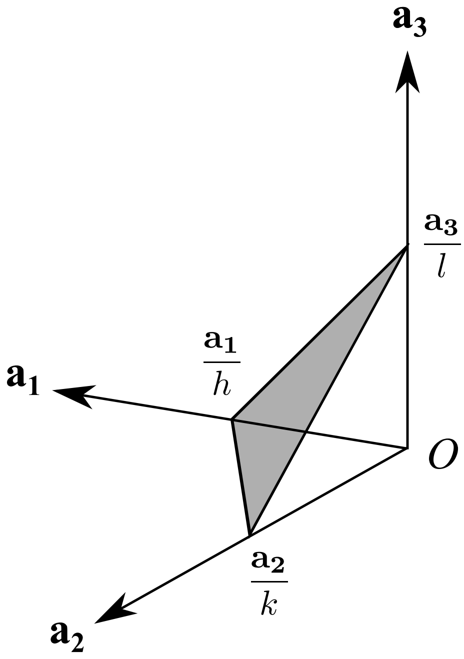

Figure 2.7: A figure demonstrating how planes are defined by Miller indices.

example the direction $\mathbf{R} = m_1\mathbf{a_1} + m_2\mathbf{a_2} + m_3\mathbf{a_3}$ is written as $[m_1m_2m_3]$. To avoid confusion, negative values are denoted with a bar, $\bar{m}$, instead of with a minus sign $-m$. Families of equivalent direction, e.g. [111], $[11\bar{1}]$, $[1\bar{1}1]$, etc. are denoted by angled bracket, i.e. $\langle 111\rangle$.

Three non-perpendicular lattice vectors can be used to define a lattice plane. We denote the orientation of plane using the Miller indices h, k, l. If a plane passes through the origin, then the next plane will intercept the lattice axes at a_1/h, a_2/k and a_3/l. Unlike directions, planes are represent using round bracket, (hkl). In a similar way to lattice direction, families of similar lattice planes are denoted using curly brackets, $\{hkl\}$.

2.2.3 The reciprocal lattice

A useful concept for understanding crystal structure is that of a reciprocal lattice. Let $\mathbf{R}$ the set of points defined by a Bravais lattice. Given the plane wave $e^{i\mathbf{k}\cdot\mathbf{R}}$, only specific values of wave vector $\mathbf{k}$ will result in the plane wave having the same periodicity as the lattice. The set of all wavevectors that satisfy this condition for given Bravais lattice are known as its reciprocal lattice. Mathematically, this condition can be represented as–

$$e^{i\mathbf{G}\cdot\mathbf{R}} = 1, \tag{2.19}$$

where $\mathbf{G}$ is a reciprocal lattice vector. Note that, in general, the right side of the equation above will include some constant phase, but we can set this to zero by ensuring one of the points of the lattice is at the origin. For a three dimensional set of lattice vectors, $\mathbf{a_1}$, $\mathbf{a_2}$, $\mathbf{a_3}$, a set of reciprocal lattice vectors, $\mathbf{b_1}$, $\mathbf{b_2}$, $\mathbf{b_3}$, can be constructed–

$$\mathbf{b_1} = 2\pi\frac{\mathbf{a_2}\times\mathbf{a_3}}{\mathbf{a_1}\cdot(\mathbf{a_2}\times\mathbf{a_3})}, \tag{2.20}$$

$$\mathbf{b_2} = 2\pi\frac{\mathbf{a_3}\times\mathbf{a_1}}{\mathbf{a_2}\cdot(\mathbf{a_3}\times\mathbf{a_1})}, \tag{2.21}$$

$$\mathbf{b_3} = 2\pi\frac{\mathbf{a_1}\times\mathbf{a_2}}{\mathbf{a_3}\cdot(\mathbf{a_1}\times\mathbf{a_2})}. \tag{2.22}$$

$$\tag{2.23}$$

Note that these vectors have been constructed such that–

$$\mathbf{a_i}\cdot\mathbf{b_j} = 2\pi\delta_{ij}, \tag{2.24}$$

where δ_{ij} is the Kronecker delta, defined by–

$$\delta_{ij} = 0, \qquad i \neq j, \tag{2.25}$$

$$\delta_{ij} = 1, \qquad i = j. \tag{2.26}$$

The reciprocal lattice vector, $\mathbf{G}$ is defined in a similar way to how position vectors are defined in the real lattice 2.14–

$$\mathbf{G} = h\mathbf{b_1} + k\mathbf{b_2} + l\mathbf{b_3}. \tag{2.27}$$

One of the properties of the reciprocal lattice vector is that $\mathbf{G_{hkl}}$ will be oriented normal to the (hkl) plane. We can demonstrate this by taking the dot product of two vectors in the plane and showing that their dot product with $\mathbf{G_{hkl}}$ is zero. From Figure 2.7, we can construct the vectors $\frac{\mathbf{a_2}}{k} - \frac{\mathbf{a_1}}{h}$ and $\frac{\mathbf{a_3}}{l} - \frac{\mathbf{a_1}}{h}$ to both be in the (hkl) plane. By considering 2.26, we find–

$$(h\mathbf{b_1} + k\mathbf{b_2} + l\mathbf{b_3}) \cdot \left(\frac{\mathbf{a_2}}{k} - \frac{\mathbf{a_1}}{h}\right) = 2\pi \left(\frac{k}{k} - \frac{h}{h}\right) = 0, \tag{2.28}$$

$$(h\mathbf{b_1} + k\mathbf{b_2} + l\mathbf{b_3}) \cdot \left(\frac{\mathbf{a_3}}{l} - \frac{\mathbf{a_1}}{h}\right) = 2\pi \left(\frac{l}{l} - \frac{h}{h}\right) = 0. \tag{2.29}$$

The distance between neighbouring (hkl) planes, $\mathbf{d_{hkl}}$, sometimes referred to as the d-spacing, can be found by taking the dot product of the plane normal vector, $\mathbf{\hat{n}}$, and a vector that connects points in neighbouring planes. By taking one of these planes to go through the origin, we can choose the vector to be $\frac{\mathbf{a_1}}{h}$. Since $\mathbf{G_{hkl}}$ is parallel to the plane normal, we can write $\mathbf{\hat{n}} = \mathbf{G}/\left|\mathbf{G}\right|$. We therefore find–

$$d_{hkl} = \mathbf{R} \cdot \mathbf{\hat{n}} = \left(\frac{\mathbf{a_1}}{h}\right) \cdot \left(\frac{h\mathbf{b_1} + k\mathbf{b_2} + l\mathbf{b_3}}{|\mathbf{G_{hkl}}|}\right) = \frac{2\pi}{|\mathbf{G_{hkl}}|}. \tag{2.30}$$

Since the equation above has h in the denominator, it will be invalid if $h = 0$. However, for any plane (hkl), it will always be possible to obtain the same result using either $\frac{\mathbf{a_2}}{k}$ or $\frac{\mathbf{a_3}}{l}$ instead of $\frac{\mathbf{a_1}}{h}$.

Equation 2.30 can be used to obtain the d-spacing for different crystal structures. For the simplest case of a cubic lattice, the reciprocal lattice vectors are orthogonal to each other, giving–

$$\begin{aligned} |\mathbf{G_{hkl}}| &= \left((h\mathbf{b_1} + k\mathbf{b_2} + l\mathbf{b_3}) \cdot (h\mathbf{b_1} + k\mathbf{b_2} + l\mathbf{b_3})\right)^{\frac{1}{2}}, && (2.31) \\ &= 2\pi d \left(h^2 + k^2 + l^2\right)^{\frac{1}{2}}, && (2.32) \\ d_{hkl} &= \frac{d}{\left(h^2 + k^2 + l^2\right)^{\frac{1}{2}}}. && (2.33) \end{aligned}$$

2.2.4 Stress and strain

During shock compressed, the large forces involved generate high stresses and strains within a material. This section lays outs the mathematical definition of these concepts.

Stress

Stress, σ, is defined as the force per unit area acting on an object. For the simple case where the stress is the same everywhere within a body, we find $\sigma = F/A$, where F is the force applied over an area A. Since stresses involve both forces and area, they are not a vector quantity, but instead represented by a second rank tensor, which in three dimensions, have nine components–

$$\sigma = \begin{pmatrix} \sigma_{11} & \sigma_{12} & \sigma_{13} \\ \sigma_{21} & \sigma_{22} & \sigma_{23} \\ \sigma_{31} & \sigma_{32} & \sigma_{33} \end{pmatrix}. \tag{2.34}$$

Each element σ_{ij} represents the force along the $\mathbf{x_i}$ direction felt by a

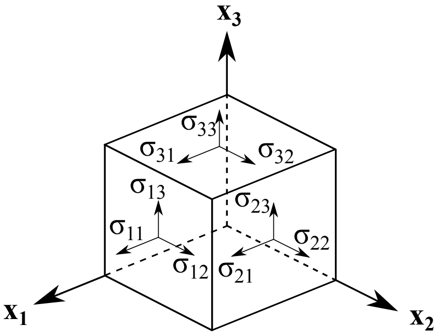

Figure 2.8: The nine components of the stress tensor.

plane with normal in the $\mathbf{x_j}$ direction, shown in Figure 2.8. The diagonal components represent normal stresses, where the forces act perpendicular to the surfaces, while the off-diagonal components represent shear stresses, where the force is applied perpendicular to the surface normals. Pairs of shear stresses with reversed indices are always equal ($\sigma_{12} = \sigma_{21}$, $\sigma_{13} = \sigma_{31}$, $\sigma_{23} = \sigma_{32}$) . If not, the moments acting on the body would be unequal, resulting in a constant rotational acceleration. Thus the stress tensor must be symmetric, and therefore there are only six independent components of the stress tensor, three normal stresses and three shear stresses.

The sign convention used suggests that positive forces are in the direction exiting the material, therefore tension is represented by a positive normal stress, while it will be negative for compression. The total pressure of a system, P, is given by the negative of the trace of the stress tensor, where a positive P will represent compression.

Strain

Strain is a measure of the deformation of a material responding to stress. The engineering strain of an object is one dimension given by–

$$e_e = \frac{l - l_0}{l}, \tag{2.35}$$

where l_0 is the original length of the sample and l is the length after deformation. By taking derivatives we find–

$$\mathrm{d}e_t = \frac{\mathrm{d}l}{l_0}, \tag{2.36}$$

$$e_t = \log\left(\frac{l}{l_0}\right). \tag{2.37}$$

This is known as true strain. Let P be a point with the coordinates (x_1, x_2) in the unstrained state, which after distortion of the body moves to the point P'. Let the coordinates of P' be $(x_1 + u_1, x_2 + u_2)$. Now consider a point Q, infinitesimally close to P, with coordinates $(x_1 + \mathrm{d}x_1, x_2 + \mathrm{d}x_2)$. After the distortion, this point moves to Q'. In the strained body, the displacement of Q will not be exactly the same as that of P. The displacement of Q to Q'. The displacement of Q to Q' has components $(u_1 + \mathrm{d}u_1, u_2 + \mathrm{d}u_2)$. We can write–

$$\mathrm{d}u_1 = \frac{\partial u_1}{\partial x_1}\mathrm{d}x_1 + \frac{\partial u_1}{\partial x_2}\mathrm{d}x_2, \tag{2.38}$$

$$\mathrm{d}u_2 = \frac{\partial u_2}{\partial x_1}\mathrm{d}x_1 + \frac{\partial u_2}{\partial x_2}\mathrm{d}x_2. \tag{2.39}$$

which can be compactly written as–

$$\mathrm{d}u_1 = \sum_{j=1}^{2} e_{ij}\mathrm{d}x_j m, \tag{2.40}$$

$$e_{11} = \frac{\partial u_1}{\partial x_1}, \qquad e_{12} = \frac{\partial u_1}{\partial x_2}, \qquad e_{21} = \frac{\partial u_2}{\partial x_1}, \qquad e_{22} = \frac{\partial u_2}{\partial x_2}. \tag{2.41}$$

The tensor e_{ij} is known as the relative displacement tensor. By setting either $\mathrm{d}x_1$ or $\mathrm{d}x_2$, we see that the diagonal components of the tensor represent normal strains, that is extension or compression along an axis, while off-diagonal components represent shear strains. We can express the tensor e_{ij} as the sum of a symmetric tensor, ϵ_{ij}, representing pure strain, and an antisymmetric tensor, ω_{ij} representing rotation–

$$e_{ij} = \epsilon_{ij} + \omega_{ij}, \tag{2.42}$$

$$\epsilon_{ij} = \frac{1}{2}\left(e_{ij} + e_{ji}\right), \tag{2.43}$$

$$\omega_{ij} = \frac{1}{2}\left(e_{ij} - e_{ji}\right). \tag{2.44}$$

In three dimensions the strain tensor will be–

$$\begin{pmatrix} \epsilon_{11} & \epsilon_{12} & \epsilon_{13} \\ \epsilon_{21} & \epsilon_{22} & \epsilon_{23} \\ \epsilon_{31} & \epsilon_{32} & \epsilon_{33} \end{pmatrix} = \begin{pmatrix} e_{11} & \frac{1}{2}\left(e_{12} + e_{21}\right) & \frac{1}{2}\left(e_{13} + e_{31}\right) \\ \frac{1}{2}\left(e_{21} + e_{12}\right) & e_{22} & \frac{1}{2}\left(e_{23} + e_{33}\right) \\ \frac{1}{2}\left(e_{31} + e_{13}\right) & \frac{1}{2}\left(e_{32} + e_{23}\right) & e_{33} \end{pmatrix}. \tag{2.45}$$

We can take advantage of the symmetry of the tensor by using the Voigt notation, which uses six components to represent the three normal strains

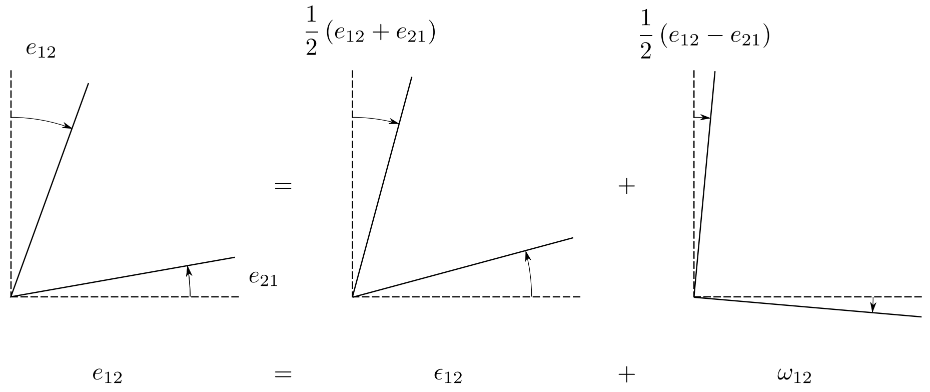

Figure 2.9: The stress tensor can be expressed as the sum of a pure strain (symmetric) and rotational (antisymmetric) tensor.

and three shear strains, shown in Equation 2.46.

$$\begin{pmatrix} \epsilon_{11} & \epsilon_{12} & \epsilon_{13} \\ \epsilon_{21} & \epsilon_{22} & \epsilon_{23} \\ \epsilon_{31} & \epsilon_{32} & \epsilon_{33} \end{pmatrix} = \begin{pmatrix} \epsilon_1 & \epsilon_6 & \epsilon_5 \\ \epsilon_6 & \epsilon_2 & \epsilon_4 \\ \epsilon_5 & \epsilon_4 & \epsilon_3 \end{pmatrix}. \tag{2.46}$$

In the limit of small strains, and assuming a linear elastic response, the stress and strain tensors can be related using elasticity theory–

$$\sigma_{ij} = c_{ijkl}\epsilon_{kl}, \tag{2.47}$$

$$\epsilon_{ij} = s_{ijkl}\sigma_{kl}. \tag{2.48}$$

where c is the stiffness tensor, and s its inverse, the compliance tensor. Both of these tensors are 3 dimensional, 4^{th} rank and thus have 81 components. However, as we have already explained, both the stress and strain tensors are symmetric, and therefore can be written with 6 components in the Voigt notation. We can now replace the stress and strain tensors with 6 dimensional vectors, and the stiffness and compliance tensor with a 6 dimensional,

2^{nd} rank tensor. The symmetry of the crystal system will usually reduce the number of independent components further. For example, cubic crystals only have three independent components–

$$c = \begin{pmatrix} c_{11} & c_{12} & c_{12} & 0 & 0 & 0 \\ c_{12} & c_{11} & c_{12} & 0 & 0 & 0 \\ c_{12} & c_{12} & c_{11} & 0 & 0 & 0 \\ 0 & 0 & 0 & c_{44} & 0 & 0 \\ 0 & 0 & 0 & 0 & c_{44} & 0 \\ 0 & 0 & 0 & 0 & 0 & c_{44} \end{pmatrix}. \qquad (2.49)$$

During compression, one may ask whether polycrystal grains will deform in a way to equalise stress or strain across grain boundaries. While stress continuity (Reuss limit [43] or iso-stress model) and strain continuity (Voigt limit [44] or iso-strain model) represent the two boundary cases, the real situation must be somewhere in between. Consider the case of a polycrystal under compression. If the grains deform via the Voigt limit, grains will experience different stresses based on their orientations (as the stiffness tensor is orientation dependent), resulting in an imbalance in stress at grain boundaries, causing them to move. However, if the grains deform via the Reuss limit, neighbouring grains would overlap or pull away from each other causing voids to form. To balance continuity of both stress and strain, statistically stored dislocations (SSDs) and geometrically necessary dislocations (GNDs) form. SSDs relieve bulk shear stresses in the grain and can be thought of as associated with the Reuss limit. GNDs accumulate in regions of high stress gradients and help grains to avoid overlapping with other grain or causing voids and thus are associated with the Voigt limit. There is no current experimental evidence to show whether either Reuss or

Voigt provides a closer approximation of material deformation under shock conditions.

2.2.5 Crystal defects

All real crystalline materials contain imperfections, which locally disturb the regular arrangement of atoms. These imperfections can be classified into several different types, based on their geometry: point, line, planar and volume defects, which are 0D, 1D, 2D and 3D respectively.

Dislocations

At the beginning of the 20th century, it was observed for many materials that the stress required to plastically deform a single crystal was several orders of magnitude lower than the theoretically predicted value (given by $\tau = \frac{G}{2\pi}$). In 1934 papers by Orowan, Polanyi and Taylor [45, 46, 47] separately proposed that this discrepancy could be accounted for the presence of defects. While it had originally been assumed slip occurred by one complete plane sliding past another, these authors postulated that pre-existing defects in the crystal would create boundaries between different regions of the crystal were already displaced by a unit of slip relative to each other. The boundaries are known as dislocations, and their movement allowed slip to occur. Successive movements of a dislocation along a slip plane result in the whole plane slipping, but since at any moment slip is only occurring at the dislocation, the critical stress for slip is much lower. The existence of dislocations was later observed in the 1950s by electron microscopy.

Figure 2.10 shows an edge dislocation, labelled as $\perp$, one of the two main types (the other being screw dislocations). A useful concept for understanding dislocations is the Burgers circuit. This is an atom-to-atom path which

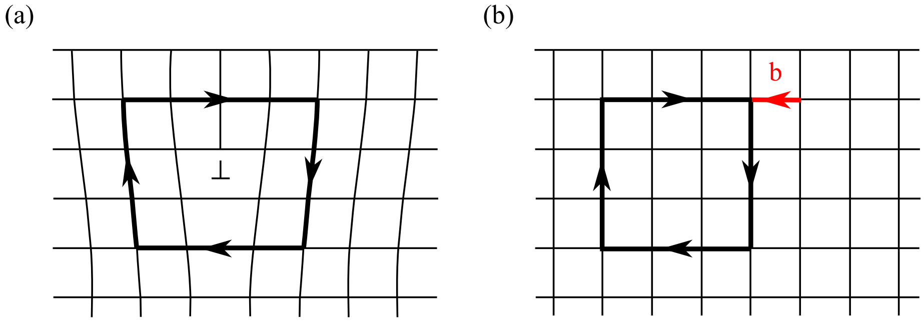

Figure 2.10: A Burger circuit around an edge dislocation.

forms a closed loop around a dislocation. Note that we require the circuit in Figure 2.10a to be large enough to only pass through relatively undisturbed parts of the crystal. If the same sequence is used in a dislocation free crystal, the circuit does not close, and the vector required to complete the circuit is known as the Burgers vector. This is the characteristic quantity that defines a dislocation, and while a dislocation may move through a crystal, its Burgers vector will remain unchanged. For an edge dislocation, the Burgers vector will be normal to the line of the dislocation while for a screw dislocation it will be parallel to the line of the dislocation. In the general case, dislocations will have mixed edge and screw character, with their Burgers vector forming an arbitrary angle to its Burgers vector.

The dislocation density, ρ_d, is defined as either the number of dislocations intersecting a plane of unit area, or the length of dislocation line per unit volume. It therefore has the dimensions of inverse area and units of m^{-2}, although it is often quoted in units of cm^{-2}. Typical values of dislocation density in metals vary between as low as $10^6\,\mathrm{cm}^{-2}$ for well annealed crystals to as high as $10^{11}\,\mathrm{cm}^{-2}$ for heavily cold-rolled samples.

When dislocations move within the surface that contains both the dis-

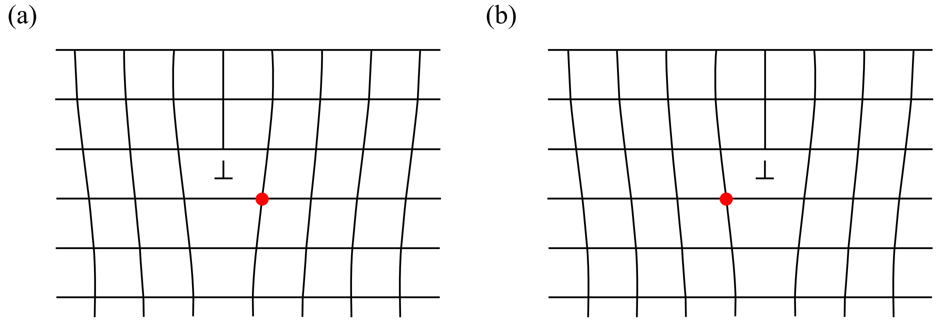

Figure 2.11: A demonstration of how glide occurs when a crystal experiences shear stress. The red circle represents is used to track the position of the same atom in both figures.

location line and Burgers vector it is known as glide. However, when a dislocation moves out of the glide surface, this is called climb. Glide of many dislocations results in slip, which is the most common mechanism for plastic deformation is crystalline materials. This can be thought of as series of successive displacements of one plane of atoms over another. The planes on which displacements occur are known as slip planes. The direction of slip is given by the Burgers vector, shown in Figure 2.11. Both the slip plane and direction are different depending on the crystal symmetry. In general, slip often occurs on the planes with the highest density of atoms, and the direction of slip is shortest translational vector within this slip plane. In the case of bcc crystals, the most common slip planes are either $\{110\}$ and $\{112\}$, and in both cases slip direction is $\langle 111 \rangle$. Together, a slip plane and slip direction form a slip system. For bcc crystals there are 12 $\{110\}\,\langle 111 \rangle$ and 12 $\{112\}\,\langle 111 \rangle$ slip systems.

A characteristic shear stress is required for slip to occur on a given slip system. Consider a cylindrical crystal with cross sectional area A being deformed by a tensile force F along its axis, illustrated in Figure 2.12. The

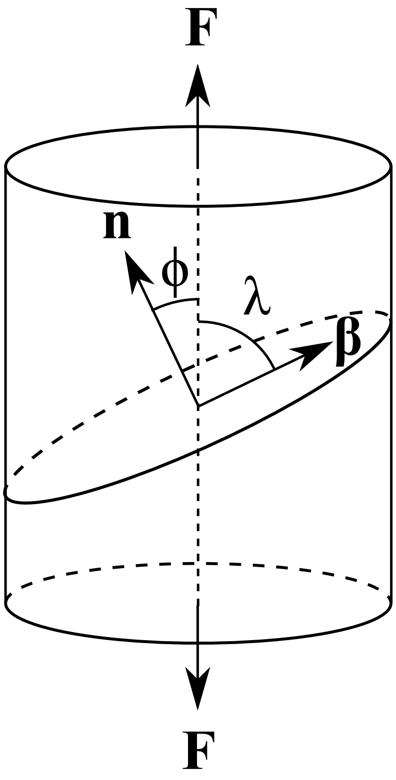

Figure 2.12: An illustration of slip in a cylindrical crystal. The normal to the slip plane and the slip direction are denoted by **n** and $\boldsymbol{\beta}$ respectively.

shear stress, τ, resolved on the slip plane in the slip direction is given by–

$$\tau = \frac{F}{A} \cos\phi \cos\lambda, \tag{2.50}$$

where ϕ is the angle between **F** and the slip plane normal, **n**, and λ is the angle between **F** and the slip direction, $\boldsymbol{\beta}$. The quantity $\cos\phi\cos\lambda$ is known as the Schmid factor. Slip systems with a higher Schmid factor will activate at a lower tensile force, and therefore will dominate over other systems. For convenience, this derivation has used the example of tension, but the mathematics are equally valid for compression.

The plastic strain rate, $\dot{\epsilon_p}$, during glide can be related to motion of dislocations, via Orowan's equation–

$$\dot{\epsilon_p} = b\rho_m \left\langle v \right\rangle , \tag{2.51}$$

where b is the magnitude of the Burgers vector, ρ_m is the dislocation density of mobile dislocations and $\langle v \rangle$ is their mean speed.

Twinning

Deformation twinning is another mechanism by which materials can plastically relax. For bcc materials twinning occurs primarily on the $\{112\}\langle 111\rangle$ system. Figure 2.13 shows that there are six stacking positions of the $\{112\}$ planes before the sequence repeats, labelled A to F. Thus we can represent this sequence of stacking as $ABCDEFAB$.... Twinning occurs when the stacking order is reversed to create two regions within the crystal that are mirror images of each other, creating a $ABCDCBA$... ordering. To create the twin, on one side of the twin plane, each plane of atoms is slipped by $\frac{1}{6}\langle 111\rangle$ compared with its neighbour.

2.2.6 Texture

Texture is the distribution of orientations of crystal grain within a polycrystalline sample. A number of manufacturing methods, such as rolling and epitaxial growth, result in characteristic textures due to the way in which the materials have been processed. This texture has an influence on a range of physical properties such as strength, electrical conductivity and wave propagation [48]. Therefore texture plays an important role in understanding material response.

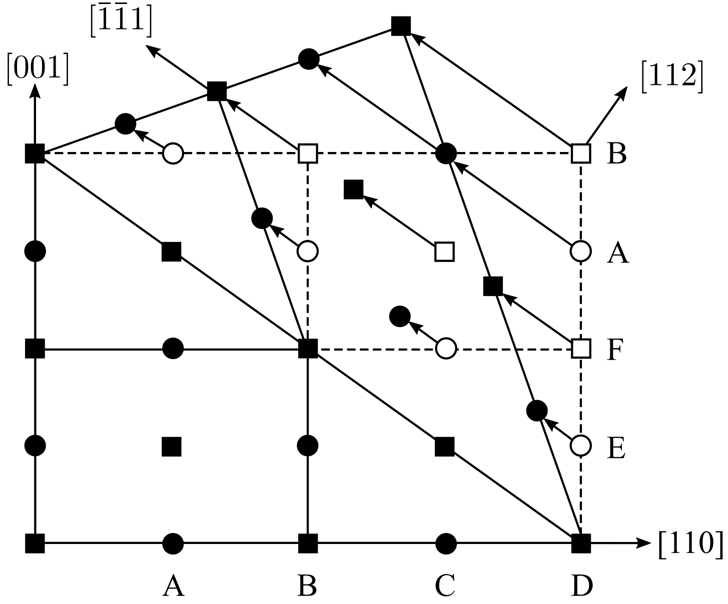

Figure 2.13: Twinning in a bcc crystal occurring by shearing on the (112) plane. The squares represent atoms in one (110) plane, while the circles represent atoms in the neighbouring plane.

The texture of a sample will also profound influence its diffraction pattern. As certain grain orientations are more likely to occur than others, the intensity of a particular Debye-Scherrer ring (corresponding to a certain set of Miller indices) will have a strong azimuthal dependence, and this dependence can in turn be used to extract texture information. Indeed, significant static studies of the texture of polycrystalline samples have been undertaken with synchrotron sources for many years. [49, 50, 48, 51, 52, 53, 54]. Wenk and co-workers provide an overview of the use of synchrotrons in such texture analysis [50]. While the texture of a material is often represented by a set of pole figures which can be measured directly via x-ray diffraction, prediction of anisotropic material properties requires knowledge of the full orientational distribution function (ODF). The ODF gives the probability of a crystallite having a given orientation, therefore provides a complete description of the texture of the sample.

2.3 X-ray diffraction

X-rays are produced when atoms undergo electron inner shell transitions, resulting in electromagnetic radiation being emitted in the range 100 eV - 100 keV or 0.01 nm - 10 nm. Since typical interatomic spacings in crystalline materials are of order 0.1 nm, this makes x-ray radiation a useful tool to probe the structure of matter. The section outlines the theory underlying this technique.

2.3.1 Bragg's law

Figure 2.14 shows two neighbouring crystal planes with spacing d with two incoming rays making an angle of θ to the plane normal. The condition for constructive interference to occur is that the path difference between the

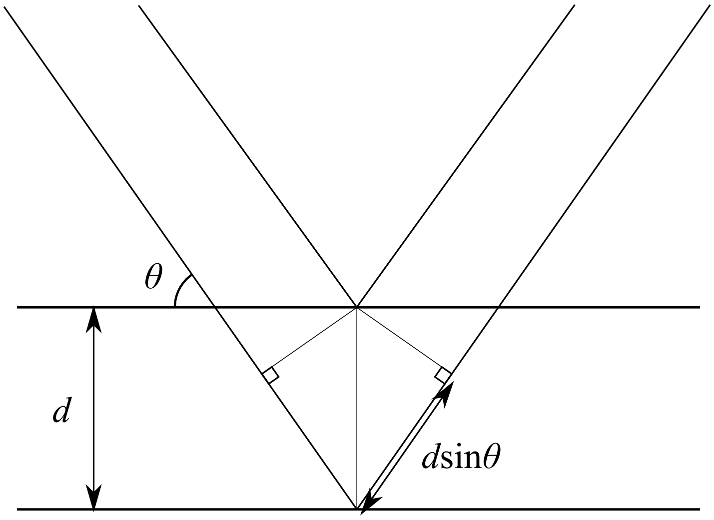

Figure 2.14: A graphical representation of Bragg's law.

two rays $2d\sin(\theta_B)$, will be an integer number of wavelengths. This gives–

$$n\lambda = 2d\sin(\theta_B), \tag{2.52}$$

where n is an integer. This is known as Bragg's law, and θ_B is referred to as the Bragg angle.

2.3.2 The Laue condition

At around the same time as Bragg developed this theory, von Laue developed a different approach, that did not rely on the assumption of specular reflections. Instead, the crystal is regarded as a collection of identical objects, formed of single atom or groups of atoms, placed at each lattice point in a Bravais lattice. Each object reradiates an incident radiation in all directions, and diffraction signal will only occur where all the scattered waves will interfere constructively.

To find the condition for constructive interference, let us consider two atoms displaced by vector $\mathbf{r}$, shown in Figure 2.15. The two incident x-rays have wavevectors $\mathbf{k}$, with magnitude $k = 2\pi/\lambda$ and have a path length difference given by–

$$r\cos(\theta) + r\cos(\theta') = \mathbf{r} \cdot \left(\hat{\mathbf{k}}' - \hat{\mathbf{k}}\right). \tag{2.53}$$

This must be equal to a multiple of the wavelength for constructive interference to occur. If we substitute this into Equation 2.53 and multiply by $2\pi/\lambda$, we get–

$$\mathbf{r} \cdot \left(\mathbf{k}' - \mathbf{k}\right) = 2\pi m. \tag{2.54}$$

Since the condition for diffraction to occur is that all scattered waves must constructively interfere, Equation 2.54 must hold for all lattice points, $\mathbf{R}$–

$$\mathbf{R} \cdot \left(\mathbf{k}' - \mathbf{k}\right) = 2\pi m. \tag{2.55}$$

From Equation 2.19, we see that $\mathbf{G} \cdot \mathbf{R}$ must also be equal to a multiple of 2π. By comparing Equations 2.19 and 2.55, we obtain the Laue condition–

$$\mathbf{k}' - \mathbf{k} = \mathbf{G}. \tag{2.56}$$

A graphical representation of the Laue condition is shown in Figure 2.15. We can use this diagram to determine–

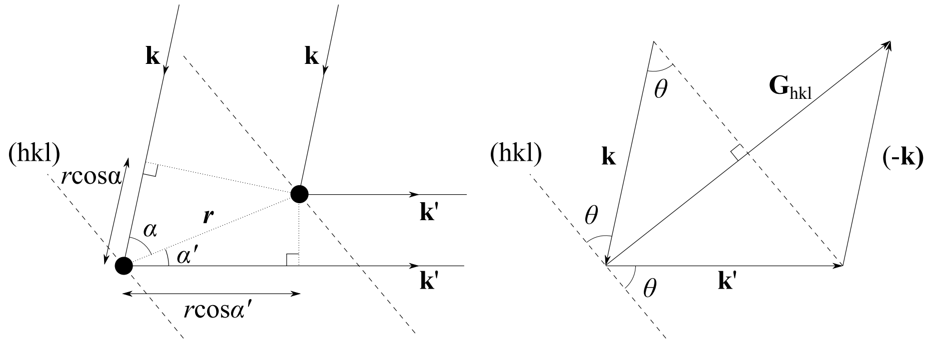

Figure 2.15: A graphical representation of the Laue condition.

$$|\mathbf{k}|\sin(\theta) = \frac{|\mathbf{G}|}{2}, \tag{2.57}$$

since $\mathbf{k}$ and $\frac{\mathbf{G}}{2}$ form two sides of a right angle triangle. By substituting in Equation 2.30 and $|\mathbf{k}| = \frac{2\pi}{\lambda}$, we find at Bragg's law–

$$\frac{2\pi}{\lambda}\sin(\theta) = \frac{2\pi}{2d_{hkl}}, \tag{2.58}$$

$$\lambda = 2d_{hkl}\sin(\theta), \tag{2.59}$$

demonstrating that both the Bragg and von Laue formations are mathematically equivalent. Note here that the factor m accounting for higher order reflections has been absorbed into d_{hkl}.

2.3.3 Atomic form factors and structure factors

So far our analysis has been based on the assumption that all the atoms within each primitive cell will interfere constructively. However, this usually incorrect and thus we must identify how the waves scattered by each atom will interact to correctly find the intensity of each reflection. Firstly, we must consider that each atom in the crystal contains a number of electrons, and it is this charge distribution $\rho\left(\mathbf{r}\right)$ from which incoming x-rays are scattered. The scattering factor of an individual atom is called the atomic form factor and is given by–

$$f_j\left(\mathbf{k}' - \mathbf{k}\right) = -\frac{1}{e}\int d\mathbf{r} e^{i\left(\mathbf{k}'-\mathbf{k}\right)\cdot\mathbf{r}}\rho_j\left(\mathbf{r}\right). \tag{2.60}$$

Secondly, we need to consider the effect of having multiple atoms in the basis. To do this, we sum the contributions from each atom in the unit cell, considering the phase difference between them. The phase difference between two atoms will be $(\mathbf{k'} - \mathbf{k}) \cdot (\mathbf{r}_j - \mathbf{r}_i)$, so the total scattering amplitude for all the atoms in the unit cell, known as the structure factor $S\left(\mathbf{k}' - \mathbf{k}\right)$, will be–

$$S\left(\mathbf{k}' - \mathbf{k}\right) = \sum_j f_j e^{i\left(\mathbf{k}'-\mathbf{k}\right)\cdot\mathbf{r_j}}. \tag{2.61}$$

The scattered intensity will then be proportional to the square of the structure factor. As an example, we can calculate the structure factor for the bcc structure. We use the conventional unit cell with lattice constant a, and the basis given in Equation 2.15. We find the structure factor as–

$$S = \sum_j f_j e^{i\mathbf{k}\cdot\mathbf{r}_j} = f\left(1 + e^{2i\pi\left(\frac{h}{a}\frac{a}{2}+\frac{k}{a}\frac{a}{2}+\frac{l}{a}\frac{a}{2}\right)}\right) = f\left(1 + e^{i\pi(h+k+l)}\right), \tag{2.62}$$

$$S = \begin{cases} 2f, & \text{if h+k+l is even.} \\ 0, & \text{if h+k+l is odd.} \end{cases} \tag{2.63}$$

We find for the case where $h + k + l$ is odd, alternating planes will

Structure	Forbidden Reflections
bcc	h+k+l is odd
fcc	h, k and l are neither all odd or all even
hcp	l is odd and h+2k = 3n for integer n

Table 2.1: Selection rules for a number of common crystal structures.

destructively interfere, resulting in there being no Bragg reflection associated with these G-vectors. These are called forbidden reflections, and a list of selection rules governing whether a reflection is forbidden or not is shown in Table 2.1 for a number of different structures.

2.3.4 Powder diffraction

A number of different geometries have been developed for x-ray diffraction, each having their own benefits and drawbacks. The earliest work by Laue used a single crystal sample and a collimated broadband x-ray source, such that for each diffracting plane, there was a corresponding photon energy such that the Bragg condition was met.

This thesis will concentrate on polycrystalline samples, and therefore we will concentrate on powder diffraction. Here a monochromatic x-ray source is used to interrogate a polycrystalline sample. Any particular grain is unlikely to be aligned such that it will meet the Bragg condition. However, since we have a large number of randomly oriented grains, we expect that a subset will be in the correct orientation to diffract the incoming x-rays. The diffraction from these planes will form a cone with angle 2θ with respect to the incident beam. These patterns are often collected on a flat detector or cylindrical film, and the captured lines are called Debye-Scherrer rings.

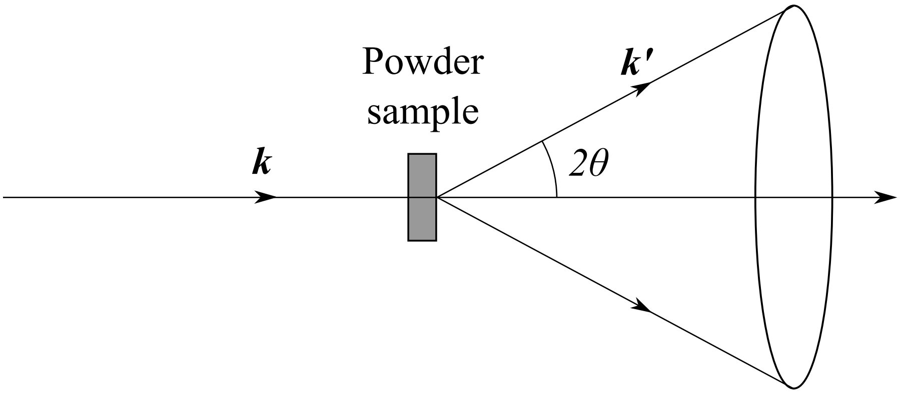

Figure 2.16: A schematic of the powder diffraction geometry.

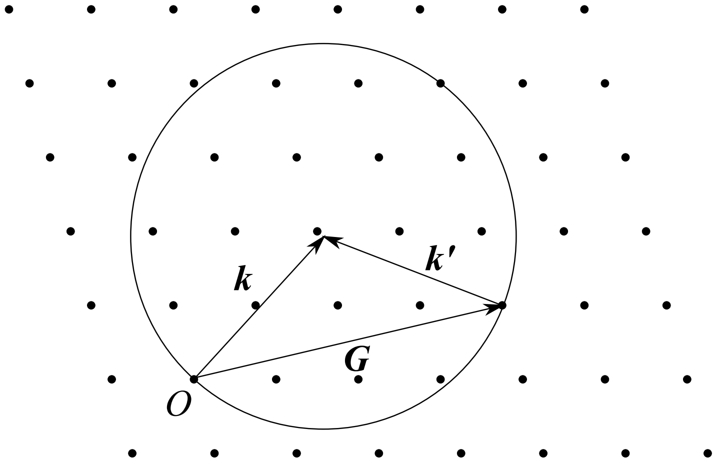

Figure 2.17: The Ewald construction demonstrating meeting of the Bragg condition

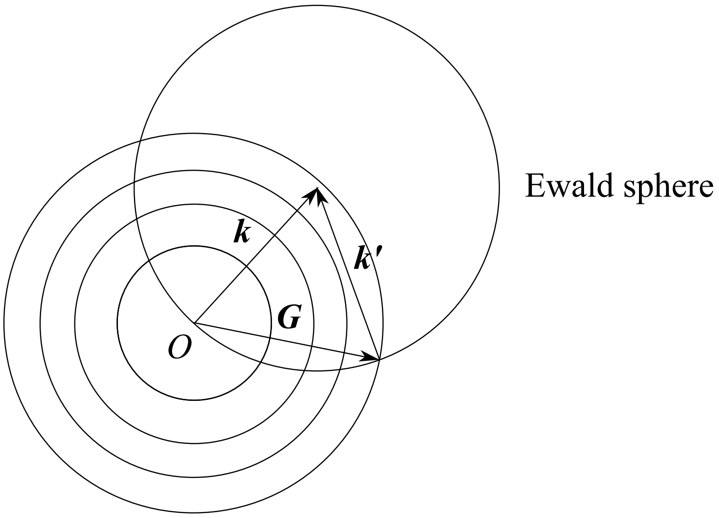

Figure 2.18: The Ewald construction for powder diffraction.

2.3.5 The Ewald sphere

It can be helpful to visualise different diffraction geometries in reciprocal space. The Ewald construction or Ewald sphere allows for a simple way to do this. Given that we assume the scattering to be elastic (thus $|\mathbf{k}| = |\mathbf{k}'|$), we can construct the loci of points that fulfil the Laue condition by constructing a sphere (or in 2D a circle) of radius k on the tip of the incident wave vector $\mathbf{k}$, such that it passes through the origin (Figure 2.17). The condition for diffraction to occur is that another reciprocal lattice point, in addition to the origin, lies on the surface of the sphere.

For the case of powder diffraction, we must consider how a polycrystalline sample appears in reciprocal space. The whole sample will be made up of many randomly oriented crystal grains, thus in reciprocal space, the sample will appear as a set of concentric spheres (or rings in 2D) centred on the origin, with each sphere corresponding to a different family of planes. To

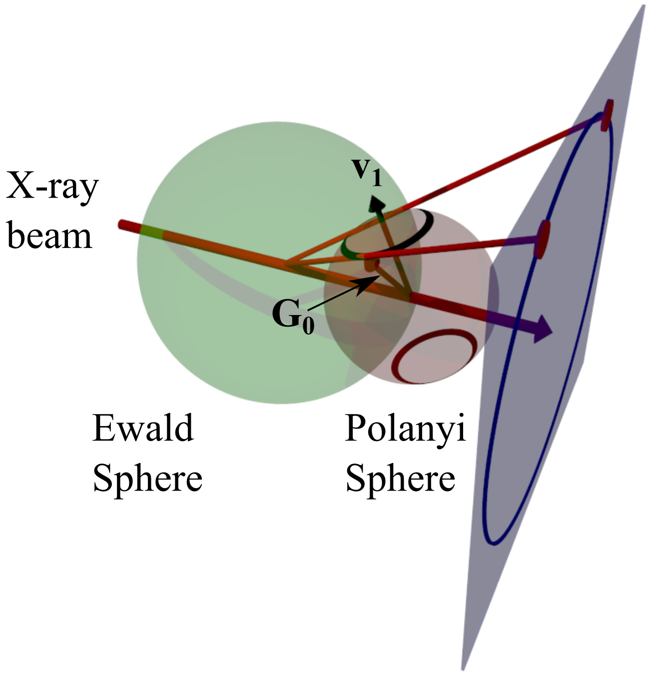

Figure 2.19: Schematic showing fibre diffraction geometry of an uncompressed sample [30]. For an untextured sample, diffraction occurs at the intersection between the green Ewald and red Polanyi spheres, resulting in the Debye-Scherrer ring. However, in a fibre textured sample, only certain crystallite orientations exist, which are represented as a ring on the Polanyi sphere. This puts another constraint on diffraction to occur, resulting in the diffraction pattern showing spots on the Debye-Scherrer rings. Figure adapted from Stribeck (2009) [55].

find the loci of where the Laue condition is met, we simply find where each of these concentric spheres intersects with the Ewald sphere, as shown in Figure 2.18.

2.3.6 The Polanyi sphere

So far we have concentrated on perfect polycrystals, where the grains are completely randomly oriented. However, as discussed earlier, many real materials exhibit preferential grain orientations known as texture. To understand what effect this texture has on the diffraction pattern, we can consider the approach developed by Polanyi [56, 57, 55], shown in Figure 2.19. As above, we can represent the possible orientations of the reciprocal lattice $\mathbf{G_0}$ in an untextured polycrystalline sample as points on the surface of a sphere, known as the Polanyi sphere. In the case of a textured sample, only some of these grain orientations are present. Figure 2.19 shows the case of a fibre texture. For the case of perfect fibre texture, each crystallite has a single crystallographic direction, the fibre orientation, $\mathbf{v_1}$, associated with the reciprocal lattice vector (h_1, k_1, l_1), which for all crystallites are aligned parallel to the sample normal, $\mathbf{n}$. Each grain is then deemed to possess a random orientation when rotated about the axis, $\mathbf{v_1}$. Hence we can represent the orientations of $\mathbf{G_0}$ in the sample as a ring of all the points which make a constant angle with $\mathbf{v_1}$. Diffraction will occur where the Ewald sphere intersects with the ring on the Ewald sphere, meaning that the Debye-Scherrer pattern is not a ring pattern, but an array of spots. Different fibre orientation will create different characteristic azimuthal positions for these spots, thus meaning that the azimuthal information from the diffraction pattern can be used to extract orientation information. While we have used fibre texture as an example, this technique is valid for any general ODF. The ODF is used to determine the probability of a given crystallite having the appropriate $\mathbf{G_0}$ existing within the sample, and where the Polanyi sphere intersects the Ewald sphere this probability is used to calculated an intensity projected onto a detector, after taking into account factors such as multiplicity.

2.4 Molecular dynamics simulations

Molecular dynamics (MD) dynamics seeks to simulate the evolution of a system of particles by integrating Newton's equations to calculate their trajectories. The forces felt by each particle are found calculated using an interatomic potential, that aims to simulate the properties of the material of interest. While here we will only be referring to systems of atoms, one should note that these techniques can be used to study any system which for which a suitable potential can be found, for example studying the dynamics of protein folding.

All molecular dynamics codes require an efficient method to calculate the forces between particles and update their positions accordingly. One such algorithm was proposed by Verlet [58]. To understand the Verlet algorithm, we Taylor expand $\mathbf{r}\left(t+\Delta t\right)+\mathbf{r}\left(t-\Delta t\right)$ and rearranging–

$$\mathbf{r}\left(t+\Delta t\right)+\mathbf{r}\left(t-\Delta t\right)=2\mathbf{r}\left(t\right)+\mathbf{a}\left(t\right)\Delta t^{2}+O\left(\Delta t^{4}\right), \tag{2.64}$$

$$\mathbf{r}\left(t+\Delta t\right)=2\mathbf{r}\left(t\right)-\mathbf{r}\left(t-\Delta t\right)+\mathbf{a}\left(t\right)\Delta t^{2}+O\left(\Delta t^{4}\right), \tag{2.65}$$

where Δt is the timestep of the simulation. The acceleration of each particle can be found by taking the spatial derivative of the potential $a=-\frac{\Delta V(t)}{m}$, and by combining this with Equation 2.65, we are able to update the position of every atom each timestep. We deliberately choose a timestep such that $O\left(\Delta t^{4}\right) << \left(\mathbf{r}\left(t+\Delta t\right)-\mathbf{r}\left(t\right)\right)$, but is long enough to stop the simulation from becoming prohibitively computationally expensive. Typical values for atomistic simulations are around a femtosecond. Since the Verlet algorithm requires the storage of the positions of the atoms for two timesteps, it is not as memory efficient as other methods. Additionally, it does not directly provide particle velocities, which must later be estimated.

The MD work carried out in this thesis was performed using the LAMMPS code (Large-scale Atomic/Molecular Massively Parallel Simulator) [59]. This code makes use of the velocity Verlet algorithm to perform the time integration [58]. This is based on the algorithm above, but explicitly calculates the velocities at each timestep and is more memory efficient. The positions and velocities are updated by the scheme given below–

$$\mathbf{r}\left(t+\Delta t\right)=\mathbf{r}\left(t\right)+\mathbf{v}\left(t\right)\Delta t+\frac{1}{2}\mathbf{a}\left(t\right)\Delta t^2, \tag{2.66}$$

$$\mathbf{v}\left(t+\Delta t/2\right)=\mathbf{v}\left(t\right)+\frac{1}{2}\mathbf{a}\left(t\right)\Delta t, \tag{2.67}$$

$$\mathbf{a}\left(t+\Delta t\right)=-\left(\Delta V\left[\mathbf{r}\left(t+\Delta t\right)\right]/m\right)+\mathbf{r}\left(t+\Delta t\right), \tag{2.68}$$

$$\mathbf{v}\left(t+\Delta t\right)=\mathbf{v}\left(t+\Delta t/2\right)+\frac{1}{2}\mathbf{a}\left(t+\Delta t\right)\Delta t. \tag{2.69}$$

Often it is desirable to extract macroscopic quantities from the simulation, via statistical mechanics. Simulations are run with a certain statistical ensemble, the most of which the most commonly used (and the one relevant to this work) is the NVE ensemble. This is where the number of particles (N), volume (V) and total energy (E) of the system are conserved and is equivalent to applying Newton's equations in an unmodified form.

2.4.1 Potentials

To correctly simulate the dynamics of materials at high pressure, accurate interatomic potentials are needed. One of the simplest and oldest potentials is the Lennard-Jones potential [60], given by–

$$V_{LJ}\left(r\right)=4\epsilon\left[\left(\frac{\sigma}{r}\right)^{12}-\left(\frac{\sigma}{r}\right)^{6}\right], \tag{2.70}$$

where r is the distance between the two particles, ϵ is the depth of the potential well and σ is the finite distance at which the attractive and repulsive terms are equal. The r^{-12} term describes the short range Pauli repulsion due to the overlapping of electrical orbitals and the r^{-6} term describes longer range attractive forces such as the van der Waals force. When modelling neutral particles, such as noble gases, this model performs reasonably well. However, since Lennard-Jones lacks a model for interatomic bonding, it performs poorly at simulating solids. Various approaches have been used to create more realistic potentials for solids by incorporating many body effects. One such approach is the embedded atom model (EAM) potential [61], which has been used to simulate many different metallic systems. It is given by–

$$V = \frac{1}{2}\sum_{i\neq j}^{N} \phi\left(r_{ij}\right) + \sum_{i}^{N} F_i\left(\rho_i\left(r_i\right)\right), \tag{2.71}$$

where $\phi\left(r\right)$ represents the pairwise interaction and ρ_i is the electron density of the neighbouring atoms. $F\left(n\right)$ is the embedding function that represents the many-body interaction and is chosen to match experimental data. While this approach is in general more accurate than the Lennard-Jones potential, the added complexity results in a longer computation time. The simulations of iron with this thesis were carried out using the Voter-Chen EAM potential [62], while the tantalum simulations were performed using the Ravelo EAM potential [63].

2.4.2 Generating simulated diffraction

The LAMMPS code returns the positions of each of the atoms in the simulation after a given number of timesteps. By treating each of the atom as a point particle, that is to say, a delta function, it possible to find the discrete 3D Fourier transform of the sample to generate a simulated diffraction pattern. The intensity for at a given scattered wavevector $\mathbf{k'}$ is given by–

$$I\left(\mathbf{k'}\right) \propto \left|F\left(\mathbf{q}\right)\right|^2 \propto \left|\sum_{j=1}^{N} Z_j e^{i\mathbf{q}\cdot\mathbf{r_j}}\right|^2 , \tag{2.72}$$

where Z_j is the atomic number of the jth atom located at $\mathbf{r_j}$ and $\mathbf{q}$ is the reciprocal lattice vector such that $\mathbf{k'} = \mathbf{k} + \mathbf{q}$. While the 'fast Fourier transform technique' can be used, for large simulations where high resolution in k-space is desired, the memory required can become prohibitive. Instead in this work, the Fourier transforms have been calculated using the scheme described in Kimminau *et al.* [64].

2.5 X-ray Free Electron Lasers

The introduction of x-ray free electron lasers (XFELs) has resulted in a step change in the quality of x-ray sources available for experiments. The advent of XFELs brought about a remarkable increase in peak spectral brightness by a factor of 10^9 [65]. These extremely bright x-ray sources provide low bandwidth hard x-rays, which are perfect for *in situ* x-ray diffraction studies.

XFELs use a linear accelerator (LINAC) to first accelerate electron bunches to close to the speed of light. These electron bunches are then sent through a periodic array of magnets with alternating north and south poles, known as an undulator. As the electrons pass between the alternating poles, the changing magnetic field causes them to oscillate transverse to their direction of motion. Since the electrons are now experiencing an acceleration, they emit electromagnetic radiation of wavelength–

$$\lambda = \frac{L}{2\gamma^2}\left(1 + \frac{K^2}{2}\right), \tag{2.73}$$

where L is the period of the undulator, γ is the Lorentz factor of the electrons and K is the undulator parameter which is related to the maximum undulator magnetic field strength, B_0, and L [66]. In order to obtain wavelengths in the x-ray regime, many orders of magnitude smaller than L, we require that γ is very large, and thus the electron bunches must be accelerated to GeV energies. To understand where this factor of $2\gamma^2$ originates, we must consider relativistic effects. Since the electron bunches approach the undulator at near the speed of light, the undulator period appears Lorentz contracted by a factor of γ. It therefore emits radiation with a wavelength of L/γ in the frame of the electron. As seen in the laboratory frame, this radiation is Doppler shifted, with a correction factor of 2γ, resulting in the $2\gamma^2$ factor in Equation 2.73 .

Many existing light sources, such as synchrotrons, are incoherent as each electron that emits radiation does so independently. However, in an XFEL, the emitted radiation is intense enough that it will begin to perturb the electron bunches. As the electrons begin to oscillate, the interaction between their transverse velocity and the transverse magnetic field from the previously emitted radiation cause a longitudinal Lorentz force that acts to create microbunches of electrons at intervals equal to the period of the emitted wavelength. Since all the electrons in a bunch oscillate together, they will emit in phase with each other, and therefore the emitted radiation will be coherent. It should also be noted that microbunching causes exponential amplification of the initial radiation, allowing for the generation of

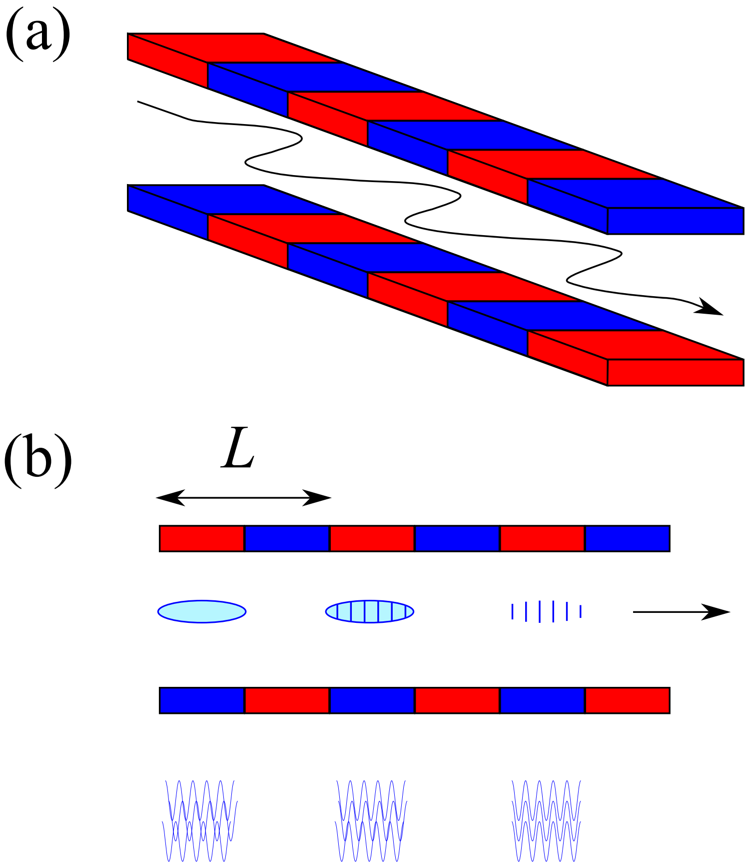

Figure 2.20: A simplified schematic describing the mechanism of a free electron laser. (a) Electron bunches from a LINAC enter a periodic array of magnets (undulator) causing them to oscillate transverse to their direction of travel. (b) The initial waves emitted from the electrons results in the formation of microbunches. Since each microbunch is separated by one wavelength, the electrons will emit coherently.

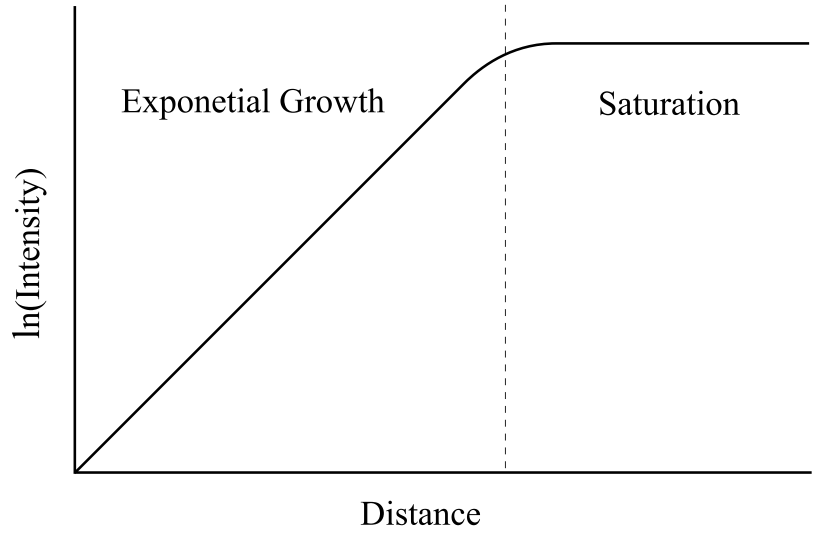

Figure 2.21: The intensity of the FEL radiation is initially amplified exponentially within the undulator. However, eventually the radiation produced will saturate.

exceptionally high intensity x-ray pulses. Since the electrons can't provide an infinite amount of energy, the intensity of the x-rays will saturate at some point along the undulator. As the electrons transfer energy to the radiation, they slow down with respect to the x-rays. This results in the electrons moving from a position where it favourable to transfer energy to the x-rays, to where it unfavourable, resulting in saturation of the pulse.

XFELs are relatively new, with only a handful of facilities currently open. The Free-electron LASer in Hamburg (FLASH) [67], was the first FEL to produce radiation in the extreme ultraviolet and soft x-ray region [68], opening in 2005. The Linac Coherent Light Source (LCLS), situated at the SLAC National Accelerator Laboratory, USA was the first machine to produce hard x-ray pulse offering photon energies up to 10 keV [69], achieved first lasing in 2009. Other facilities, such as FERMI in Italy [70] and SACLA in Japan

Figure 2.22: An aerial view of LCLS, with the LINAC and undulator section highlighted [74]. Licensed under a Creative Commons Attribution (CC BY-NC 2.0) license [75].

[71] have also begun operations, while the European XFEL in Hamburg [72] and SwissFEL in Villigen [73] are currently under construction.

2.5.1 Introduction to LCLS and comparison to existing x-ray sources

The accelerator for LCLS was built by repurposing roughly a kilometre section of the historic SLAC LINAC to provide 3.5-15 GeV electrons. It uses a 132 m undulator to provide a tuneable x-ray source with photons of energies ranging from 280 eV up to 10 keV. The machine currently has seven different instruments each designed to probe a different area of physics. Of particular interest is the Matter in Extreme Conditions (MEC) instrument [76], opened in 2012, with the aim to investigate material at high densities and temperatures. It is equipped with a 200 TW short pulse laser and a 40 J long pulse nanosecond laser. The combination of these lasers and the LCLS beam offerers a unique set of capabilities for studying dynamically compressed matter.

Historically, most laser compression experiments using *in situ* diffraction have used laser-plasma sources as x-ray backlighters. These sources have a number of advantages, such as their relatively short pulse length which is needed to capture dynamics on the temporal scales of laser experiments, as well as the convenience of being able to use lasers as both pump and probe. However, experiments using these sources have often struggled with low photon flux and poor contrast from the Helium-α source. XFELs offer a number of advantages over these sources. LCLS offers up to 10^{12} photons in a single pulse, as compared with $\sim 10^9$ on target in as laser-plasma source. XFELs can be tuned to a specific photon energy by changing the energy of the electron bunches. Additionally, under normal operation the bandwidth of LCLS is 0.2%, much smaller than the $\sim 1\%$ bandwidth offered by Helium-α sources. XFELs offer exquisite temporal resolution, with pulse lengths $\sim 100\,\text{fs}$, therefore allowing x-ray diffraction images to freeze motion on a timescale faster than the shortest phonon period of the material. LCLS also provides a highly collimated source, meaning the beam can be focused down to micron scale spot size. This allows for the drive laser to be focused to a much smaller spot than in laser-plasma experiment, while still ensuring a uniform shock front over the probed region. As a result, very high pressure states can be achieved with a relatively small laser system.

While synchrotrons have been used in dynamic compression experiment, their use in laser experiments has been limited. While modern synchrotrons provide similar average photon fluxes as XFELs, the photon flux per pulse is significantly lower, making it difficult to obtain good quality diffraction on the timescale of laser experiments. As a result, most compression experiments on synchrotrons have focused on lower strain rates, such as those produced by gas guns [77] and dynamic diamond anvil cells (dDAC) [78]. Despite these limitations, some laser experiments have been performed, such as the work by Torchio *et al.* measuring Extended X-ray Absorption Fine

Structure (EXAFS) in shock compressed iron up to 500 GPa. Recent and proposed upgrades to several synchrotrons mean in the near future are improving the available photon fluxes and dynamic compression experiments are becoming viable. Future facilities such as the Dynamics Compression Sector (DCS) at the Advances Photon Source and the proposed High Power Laser Facility (HPLF) at the European Synchrotron Radiation Facility have been designed with laser compression in mind and aim to close the gap to XFELs.

CHAPTER 3

Predicting Debye-Scherrer Diffraction Patterns Under Arbitrary Deformations

This chapter outlines a method for the prediction of powder diffraction patterns under an arbitrary deformation. The mathematical derivation is presented and for the purposes of verification, and a comparison between the theory and ray traces is shown. Finally, this method is applied to the problem of measuring large shear strains in dynamically compressed samples. This work forms the basis of a paper published jointly with Andrew Higginbotham in the Journal of Applied Physics [29]. Reproduced from Higginbotham and McGonegle, *J. Appl. Phys.* **115**, 174906 (2014), with the permission of AIP Publishing.

3.1 Motivation

Powder diffraction has been used as a powerful diagnostic of crystal structure for many decades and remains one of the most sensitive techniques we have for probing the structure of materials. In particular, a plethora of complex high pressure phases have been discovered in a diverse range of materials [79, 80, 81]. Laser compression has been increasingly used as a tool to study how materials behave at very high pressures, as well as to study how they deform at high strain rates. For example, recent work by Rygg and coworkers has demonstrated powder diffraction from solid samples at pressures of up to 800 GPa [82], with pressures of over 1 TPa now achievable on large scale laser facilities [83]. During laser compression, a uniaxial shock, or for higher pressures, ramp waves are launched into the sample leading to an initial state of uniaxial elastic strain, known as an elastic precursor. Molecular dynamics (MD) simulations of ultra-high strain-rate shocks have suggested these elastic precursors can exceed a uniaxial strain of 15% [84, 85, 63], and therefore small strain anisotropy can no longer be assumed. These high elastic precursors have been shown to occur experimentally, via velocimetry [86, 87, 88] and, more recently, through the use of picosecond diffraction performed on 4th generation light sources [1]. In addition, enhanced strength of materials at high pressure could potentially lead to large departures from a hydrostatic response, even after plasticity or structural phase change have relieved the initial elastic strain anisotropy. This departure from traditional small deviatoric strain limit leads to a need for more careful analysis of Debye-Scherrer rings from the material under compression.

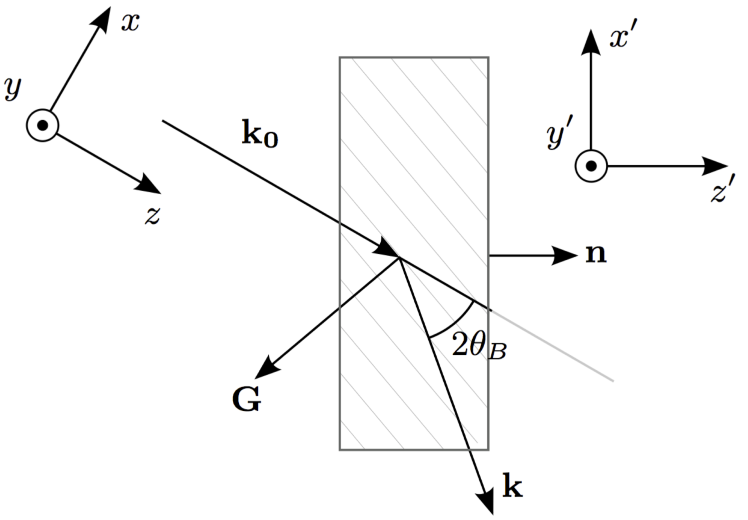

Figure 3.1: The sample geometry considered, illustrating the relation between sample (primed) and lab coordinates for the derivation.

3.2 Derivation

We consider the setup shown is Figure 3.1. A polycrystal with sample normal $\mathbf{n}$ is interrogated by a monochromatic source. A representative diffraction path is shown, with scattering of radiation of incident wavevector $\mathbf{k_0}$ by planes with the indicated orientation, and associated reciprocal lattice vector $\mathbf{G}$, leading to scattered radiation of wavevector $\mathbf{k} = \mathbf{G} + \mathbf{k_0}$. The sample normal, $\mathbf{n}$ is also indicated.

For simplicity, and without loss of generality, we work in a coordinate system where the incident x-ray direction, $\mathbf{k_0}$, is along z. Note that in general this choice clashes with the convention that z is the shock direction in the sample. This leads us to define two coordinate systems, one attached to the sample, where the shock is along z, and one, referred to as lab coordinates, where the x-ray incidence direction defines z. We also define a rotation matrix, $\mathbf{R}$, which transforms us from lab coordinates to sample coordinates. For x-rays incident along the shock direction $\mathbf{R} = \mathbf{I}$, the identity matrix.

To start, we note that any general diffracting plane will have outgoing $\mathbf{k}$ vector defined, in the lab coordinate system, by -

$$\mathbf{k} = \frac{2\pi}{\lambda} \begin{pmatrix} \sin 2\theta_B \cos\phi \\ \sin 2\theta_B \sin\phi \\ \cos 2\theta_B \end{pmatrix}, \tag{3.1}$$

where θ_B is the Bragg angle in the compressed system and ϕ the azimuthal angle around the Debye-Scherrer ring. By noting the Laue condition ($\mathbf{G} = \mathbf{k} - \mathbf{k_0}$) we define $\mathbf{G}$, the diffracting reciprocal lattice vector, as -

$$\mathbf{G} = \frac{2\pi}{\lambda} \begin{pmatrix} \sin 2\theta_B \cos\phi \\ \sin 2\theta_B \sin\phi \\ \cos 2\theta_B - 1 \end{pmatrix}. \tag{3.2}$$

Note that this reciprocal lattice vector denotes a set of planes, within a certain grain in the sample, which now meet the Bragg condition after being deformed. They are not, in general, the same planes which diffracted in the undeformed sample (i.e. as we compress a sample, we actually change the subset of grains which we are probing).

We proceed by finding the equivalent vector, $\mathbf{G_0}$ in the undeformed system. We limit discussion here to the Voigt (iso-strain) condition, under which the deformation of all grains can be defined by a single deformation gradient, $\mathbf{F}$. The Voigt limit is chosen as strain is directly related to the position of the atoms and therefore is closely related to the diffraction pattern. Since $\mathbf{G}$ is a reciprocal lattice vector we must consider not the deformation in real space, but the associated 'deformation' of reciprocal space. For a general deformation gradient in real space the reciprocal space analogue is given by $\mathcal{F} = \left(\mathbf{F}^{\mathrm{T}}\right)^{-1}$ (see appendix A). Thus, to return the deformed reciprocal space back to the undeformed we use $\mathcal{F}^{-1} = \mathbf{F}^{\mathrm{T}}$.

This gives $\mathbf{G_0}$, the original, unstrained reciprocal lattice vector as -

$$\mathbf{G_0}' = \mathbf{F^T R G} = \boldsymbol{\alpha}\mathbf{G} \tag{3.3}$$

$$= \frac{2\pi}{\lambda} \begin{pmatrix} \alpha_{11} & \alpha_{12} & \alpha_{13} \\ \alpha_{21} & \alpha_{22} & \alpha_{23} \\ \alpha_{31} & \alpha_{32} & \alpha_{33} \end{pmatrix} \begin{pmatrix} \sin 2\theta_B \cos\phi \\ \sin 2\theta_B \sin\phi \\ \cos 2\theta_B - 1 \end{pmatrix}, \tag{3.4}$$

where $\alpha = \mathbf{F^T R}$. The prime denotes that the reciprocal lattice vector is expressed in terms of sample coordinates. One could of course apply the transpose rotation tensor, $\mathbf{R^T}$, from the left hand side in equation 3.3, rotating the result back in to the lab coordinates. However, this would complicate the form of $\boldsymbol{\alpha}$, and as we will see, the direction of $\mathbf{G_0}$ is of no consequence.

As noted above, the fact that $\mathbf{G}$ meets the Laue condition is no guarantee that $\mathbf{G_0}$ did, so the only information of use in $\mathbf{G_0}$ is its length, $|\mathbf{G_0}'| = 2\pi/d_0$. By exploiting this knowledge one can assign a value to $|\mathbf{G_0}|^2$ and thus recover and expression for linking θ_B and ϕ such that -

$$\left(\frac{2\pi}{d_0}\right)^2 = \left|\boldsymbol{\alpha}\left(\mathbf{k} - \mathbf{k_0}\right)\right|^2 \tag{3.5}$$

$$\begin{aligned} \frac{\lambda^2}{d_0^2} &= \sin^2 2\theta_B \left(A_1 \cos^2\phi + 2A_2 \cos\phi \sin\phi + A_4 \sin^2\phi\right) \\ &\quad + \sin 2\theta_B \left(\cos 2\theta_B - 1\right)\left(2A_3 \cos\phi + 2A_5 \sin\phi\right) \\ &\quad + \left(\cos 2\theta_B - 1\right)^2 A_6, \end{aligned} \tag{3.6}$$

Table 3.1: Summary of the A_i and D_i coefficients in terms of the α_{ij} components.

A_1	$\alpha_{11}^2 + \alpha_{21}^2 + \alpha_{31}^2$
A_2	$\alpha_{11}\alpha_{12} + \alpha_{21}\alpha_{22} + \alpha_{31}\alpha_{32}$
A_3	$\alpha_{11}\alpha_{13} + \alpha_{21}\alpha_{23} + \alpha_{31}\alpha_{33}$
A_4	$\alpha_{12}^2 + \alpha_{22}^2 + \alpha_{32}^2$
A_5	$\alpha_{12}\alpha_{13} + \alpha_{22}\alpha_{23} + \alpha_{32}\alpha_{33}$
A_6	$\alpha_{13}^2 + \alpha_{23}^2 + \alpha_{33}^2$
D_1	$A_1 \cos^2\phi + 2A_2 \cos\phi \sin\phi + A_4 \sin^2\phi$
D_2	$2A_3 \cos\phi + 2A_5 \sin\phi$
D_3	A_6

where the A coefficients, defined in Table 3.1, correspond to the combinations of rotated deformation gradient components. This equation gives the relation between θ_B and ϕ as one proceeds around the Debye-Scherrer ring. Note that throughout the proof we only employ universal properties of the reciprocal lattice, and therefore this approach is valid for all crystal symmetries.

3.3 Example Geometries

3.3.1 $\mathbf{R} = \mathbf{I}$, normal strain only

In this geometry we have the sample coordinate system identical to our lab geometry such that $\mathbf{R} = \mathbf{I}$. We also assume that the off-diagonal elements of the strain tensor are zero (as we typically do not consider pure shear in shock physics applications). In this case equation 3.6 can be simplified by noting that the only non-zero coefficients are $A_1 = \alpha_{11}^2$, $A_4 = \alpha_{22}^2$ and

$A_6 = \alpha_{33}^2$ so that–

$$\frac{\lambda^2}{d_0^2} = \sin^2 2\theta_B \left(\alpha_{11}^2 \cos^2\phi + \alpha_{22}^2 \sin^2\phi\right) + \\ \left(\cos 2\theta_B - 1\right)^2 \alpha_{33}^2. \tag{3.7}$$

Note that in this case the rotated deformation gradient is simply–

$$\alpha = \begin{pmatrix} 1+\varepsilon_{xx} & 0 & 0 \\ 0 & 1+\varepsilon_{yy} & 0 \\ 0 & 0 & 1+\varepsilon_{zz} \end{pmatrix}. \tag{3.8}$$

Rearranging equation 3.7 we arrive at–

$$\sin^4\theta_B \left(\alpha_{33}^2 - \alpha_{11}^2\cos^2\phi - \alpha_{22}^2\sin^2\phi\right) + \\ \sin^2\theta_B \left(\alpha_{11}^2\cos^2\phi + \alpha_{22}^2\sin^2\phi\right) - \frac{\lambda^2}{4d_0^2} = 0. \tag{3.9}$$

For $\alpha_{11} = \alpha_{22} = \alpha_{33}$ we recover hydrostatic compression and the expression is seen to reduce to Bragg's law as expected.

3.3.2 Tilted target geometry

Although the $\mathbf{R} = \mathbf{I}$ geometry discussed above is common in static experiments, shock physics environments rarely allow such symmetry. In addition, the non normal x-ray incidence can be of some advantage. As shown by Singh, and for the shock case by Hawreliak and coworkers, by tilting the sample relative to the incoming x-rays we encode information on differing strain components around the Debye-Scherrer ring [89, 90, 25].

In tilted target geometry we apply a rotation of χ about y to give–

$$\alpha = \begin{pmatrix} 1+\varepsilon_{xx} & 0 & 0 \\ 0 & 1+\varepsilon_{yy} & 0 \\ 0 & 0 & 1+\varepsilon_{zz} \end{pmatrix} \begin{pmatrix} \cos\chi & 0 & -\sin\chi \\ 0 & 1 & 0 \\ \sin\chi & 0 & \cos\chi \end{pmatrix}, \tag{3.10}$$

where we have once again assumed only normal strains for simplicity. This gives–

$$\begin{aligned} \frac{\lambda^2}{d_0^2} = & \Big((1+\varepsilon_{xx})^2 \cos\chi^2 \cos^2\phi + (1+\varepsilon_{yy})^2 \sin^2\phi + \left(1+\varepsilon_{zz}^2\right) \sin^2\chi \cos^2\phi \Big) \sin^2 2\theta_B \\ & + 2\cos\chi \sin\chi \left((1+\varepsilon_{zz})^2 - (1+\varepsilon_{xx})^2 \right) \cos\phi \sin 2\theta_B \left(\cos 2\theta_B - 1\right) \\ & + \Big((1+\varepsilon_{xx})^2 \sin^2\chi + (1+\varepsilon_{zz})^2 \cos^2\chi \Big) \left(\cos 2\theta_B - 1\right)^2 \end{aligned} \tag{3.11}$$

Once again, we note that this reduces to the $\mathbf{R} = \mathbf{I}$ geometry equation for $\chi = 0$. In order to solve this equation for θ we define deformation, ϕ and χ coefficients such that -

$$D_1 \sin^2 2\theta_B + D_2 \sin 2\theta_B \left(\cos 2\theta_B - 1\right) + D_3 \left(\cos 2\theta_B - 1\right)^2 - \frac{\lambda^2}{d_0^2} = 0, \tag{3.12}$$

$$\begin{aligned} D_1 \left(\frac{e^{2i\theta_B} - e^{-2i\theta_B}}{2i} \right)^2 + D_2 \left(\frac{e^{2i\theta_B} - e^{-2i\theta_B}}{2i} \right) \left(\frac{e^{2i\theta_B} + e^{-2i\theta_B}}{2} - 1 \right) + \\ D_3 \left(\frac{e^{2i\theta_B} + e^{-2i\theta_B}}{2} - 1 \right)^2 - \frac{\lambda^2}{d_0^2} = 0, \\ \left(D_3 - D_1 - iD_2\right) e^{i8\theta_B} - \left(4D_3 - 2iD_2\right) e^{i6\theta_B} + \left(2D_1 + 6D_3 - \frac{4\lambda^2}{d_0^2} \right) e^{i4\theta_B} \\ - \left(2iD_2 + 4D_3\right) e^{i2\theta_B} + \left(D_3 + iD_2 - D_1\right) = 0, \end{aligned} \tag{3.13}$$

where the D coefficients are defined by comparison between equations 3.11

and 3.12. This quartic in $e^{i2\theta_B}$ can be solved using the Ferrari method[91] to find θ_B.

3.3.3 The general solution

It should be noted that the derivation of section 3.3.2 is equally applicable in the general case (though the normal strain, tilted target solution is expected to be sufficient for most applications). Here, we refer to equation 3.6 to see that we can define the D coefficients of equation 3.12 in a more general sense as–

$$D_1 = A_1 \cos^2\phi + 2A_2 \cos\phi \sin\phi + A_4 \sin^2\phi, \tag{3.14}$$

$$D_2 = 2A_3 \cos\phi + 2A_5 \sin\phi, \tag{3.15}$$

$$D_3 = A_6. \tag{3.16}$$

The solution in equation 3.13 is then equally valid with these new D coefficients. A summary of the full form of the A_i and D_i coefficients is given in table 3.1.

3.4 Verification

In order to verify the previous formulae, we compare with synthetic diffraction data obtained by ray tracing from polycrystals. While in a polycrystalline MD simulation, much care is taken to ensure the grain boundaries are relaxed, this is not necessary for verification purposes. We computationally generated a sample where each randomly oriented grain is offset by a random displacement and deform it according to a specified deformation gradient. The resultant set of atomic coordinates was used as the input to a ray tracing calculation in a variety of geometries [64]. In this calculation,

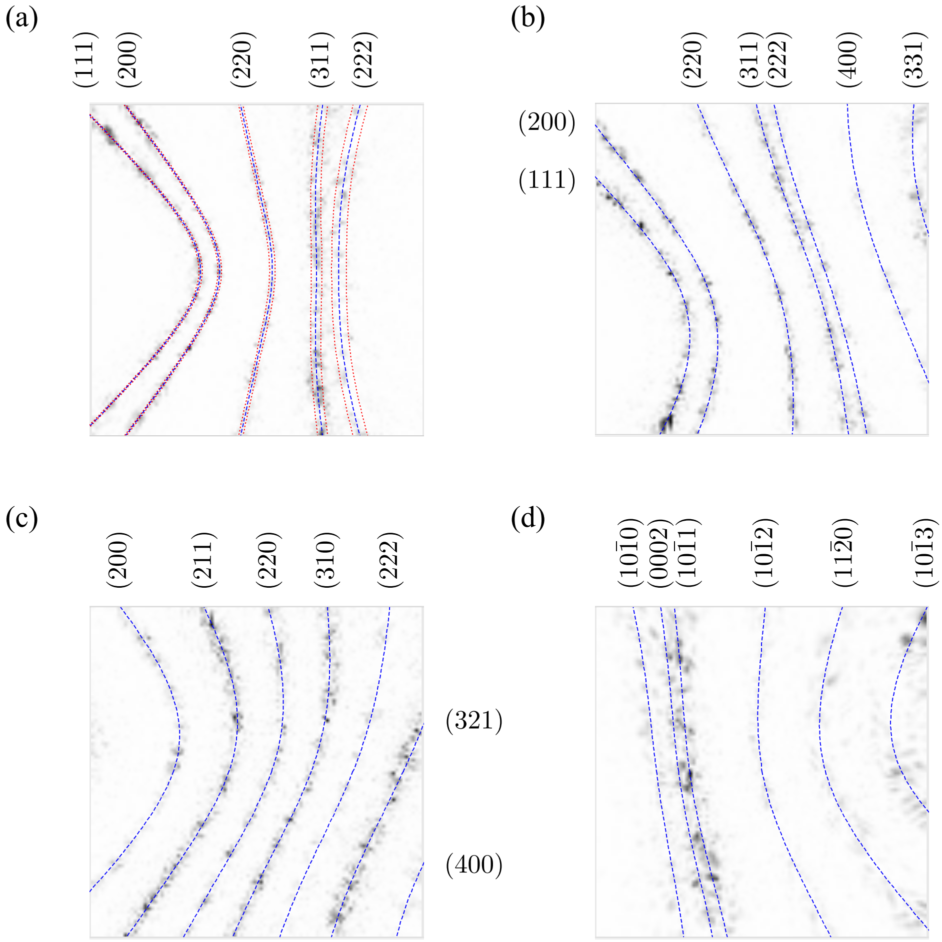

Figure 3.2: Ray traced diffraction signals from deformed polycrystals. Theory overlays are shown as (solid) blue lines. Panel (a) shows a detector 400x400mm, 100mm away from the Cu sample with the centre of the detector corresponding to $2\theta_B = 90^\circ$, $\phi = \pi$, in a geometry with $\mathbf{R} = \mathbf{I}$ and the deformation defined by equation 3.18. Panel (b) shows the same detector, but with $\chi = \pi/4$ and the deformation defined by equation 3.19b. Panels (c) and (d) have the the same geometry as panel b, but have Ta and Ti sample strained by the deformation gradients 3.19c and 3.19d respectively.

'photons' are traced from detector pixel back to source, via a sample position. in doing so, for a given photon wavelength we define, via the Laue condition, a diffracting G-vector. The diffraction signal is simply related to the intensity of the Fourier transform of atomic positions -

$$I\left(G\right) = \left|\sum_{j} e^{i\mathbf{G}.\mathbf{r_j}}\right|^2 , \tag{3.17}$$

where the sum is over all atoms in the diffracting sample. Having defined an intensity per pixel we have an artificial diffraction image, which should show deformation of the Debye-Scherrer rings consistent with the theory above provided a consistent use of the deformation gradient.

To demonstrate the agreement between theory and ray trace we show several examples. In the first, we set $\mathbf{R} = \mathbf{I}$ and normal strain only corresponds to a common synchrotron geometry (where, for example, small departures from hydrostatic stress are seen in diamond anvil cells). In this case we choose a simple deformation gradient of the form -

$$\mathbf{F_a} = \alpha = \begin{pmatrix} 0.8 & 0.0 & 0.0 \\ 0.0 & 0.9 & 0.0 \\ 0.0 & 0.0 & 0.7 \end{pmatrix} . \tag{3.18}$$

This deformation gradient is applied to the atomic positions of the initially undeformed Cu polycrystal, formed of 1000 crystallites each containing 20x20x20 unit cells. Ray tracing of 9 keV photons to a detector plane with normal perpendicular to the load axis results in figure 3.2a. The simulated diffraction from grains which meet the Bragg condition in the deformed sample match well with the theory above (blue lines). Also shown are theory lines for deformation gradients where we use $\alpha_{33} = 0.7 \pm 0.01$, corresponding to around a 1.5% change in volume of the deformed sample. It should be noted that diffraction from all grains lies within these bounds and that the bounds reflect the symmetry of the grain distribution, indicative of the blue theory lines lying at the centre of the Debye-Scherrer ring.

More complex examples are shown in figures 3.2b, 3.2c and 3.2d, using Cu (FCC), Ta (BCC) and Ti (HCP) samples respectively. These samples used 1000 crystallites each containing 10x10x10 unit cells. In these cases we use a rotation of $\chi = \pi/4$ and a random deformation gradient–

$$\mathbf{F_b} = \begin{pmatrix} 0.883 & -0.279 & 0.159 \\ -0.110 & 1.037 & 0.177 \\ 0.270 & -0.071 & 1.188 \end{pmatrix}, \qquad \mathbf{F_c} = \begin{pmatrix} 0.881 & 0.028 & -0.145 \\ 0.235 & 1.217 & 0.204 \\ 0.276 & -0.210 & 1.147 \end{pmatrix},$$

$$\mathbf{F_d} = \begin{pmatrix} 1.254 & 0.168 & 0.041 \\ -0.268 & 0.740 & -0.018 \\ 0.018 & -0.222 & 1.293 \end{pmatrix}. \tag{3.19}$$

This geometry has a detector with normal perpendicular to $\mathbf{k_0}$, photon energies of 7 keV, 8 keV and 4 keV respectively. Again, good agreement between ray trace and theory is seen, verifying the form of equation 3.11. For comparison, the raytraces for ambient Cu, Ta and Ti are shown in figure 3.3.Note we demonstrate this is true for both cubic and non-cubic lattices, supporting the claim we made earlier that this technique does not make any assumption of the crystal being cubic, and thus is valid for any crystal symmetry.

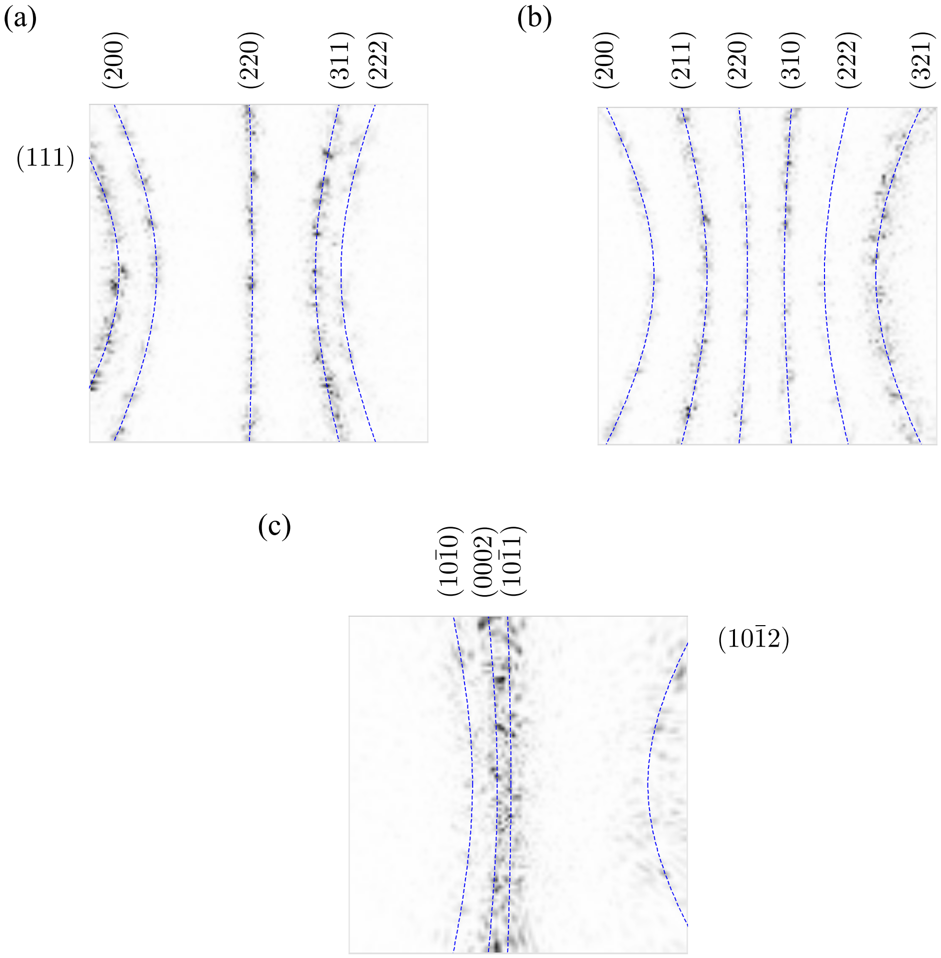

Figure 3.3: Ray traced diffraction signals from deformed polycrystals. All panels show a detector 400x400mm, 100mm away from the sample with the centre of the detector corresponding to $2\theta_B = 90°$, $\phi = \pi$. Panels (a), (b) and (c) show Cu (FCC), Ta (BCC) and Ti (HCP) respectively. Note that under hydrostatic conditions the theoretical prediction simplifies to the Bragg condition and thus the diffraction pattern is azimuthally symmetric.

3.5 Strength measurement

One key consideration in shock compression is the degree of departure from hydrostatic stress. This property, known as strength, may exhibit itself in the finite degree of initial uniaxial elastic compression (i.e. yield strength, or Hugoniot Elastic Limit) or in residual elastic strain anisotropy after plastic deformation or phase change. Similar scenarios have been studied in terms of non-hydrostatic conditions between the planar culets of conventional diamond anvil cells. For example, Singh discusses the effects of finite shear stress on the diffraction from high pressure samples [89]. As one of the few extant theories concerning diffraction in highly non-hydrostatic conditions, we compare our results to the widely used formulae of Singh.

We start with the outgoing **G** (noting it has a length of $2\pi/d$)–

$$\mathbf{G} = \frac{2\pi}{d}\begin{pmatrix} \sin\psi \\ 0 \\ \cos\psi \end{pmatrix}, \tag{3.20}$$

where ψ is the angle between **G** and the compression direction. As before, we work out the equivalent vector, $\mathbf{G_0}$, in the undeformed reciprocal lattice. Thus we apply a deformation gradient (and since rotations do not affect the result, an α tensor of)–

$$\mathbf{F^T} = \alpha = \begin{pmatrix} 1+\varepsilon_p-2\gamma/3 & 0 & 0 \\ 0 & 1+\varepsilon_p-2\gamma/3 & 0 \\ 0 & 0 & 1+\varepsilon_p+4\gamma/3 \end{pmatrix}, \tag{3.21}$$

where, following Singh, $\epsilon_p = \frac{1}{3}\left(2\varepsilon_{xx}+\varepsilon_{zz}\right)$ and $\gamma = \left(\varepsilon_{zz}-\varepsilon_{xx}\right)/2$ is the shear strain. Applying this to **G**, and taking the modulus squared–

$$\left(\frac{2\pi}{d_0}\right)^2 = \left(\frac{2\pi}{d}\right)^2 \left(\alpha_{11}^2 \sin^2\psi + \alpha_{33}^2 \cos^2\psi\right), \tag{3.22}$$

$$\Rightarrow \left(\frac{d}{d_0}\right)^2 = \alpha_{11}^2 \left(1 - \cos^2\psi\right) + \alpha_{33}^2 \cos^2\psi \tag{3.23}$$

$$= \alpha_{11}^2 + \left(\alpha_{33}^2 - \alpha_{11}^2\right) \cos^2\psi. \tag{3.24}$$

Since Singh works exclusively in the small γ limit we note that–

$$\alpha_{11}^2 \approx (1+\varepsilon_p)^2 - 4\gamma\,(1+\varepsilon_p)/3, \tag{3.25}$$

$$\alpha_{33}^2 \approx (1+\varepsilon_p)^2 + 8\gamma\,(1+\varepsilon_p)/3, \tag{3.26}$$

where ε_d^V is the change in d-spacing due to the deviatoric strain component in the Voigt limit. This allows us to express equation 3.24 as–

$$\left(\frac{d}{d_0}\right)^2 \approx (1+\varepsilon_p)^2 - \frac{4\,(1+\varepsilon_p)\,\gamma}{3}\left(1 - 3\cos^2\psi\right) \tag{3.27}$$

$$\approx \left((1+\varepsilon_p) - \frac{2\gamma}{3}\left(1 - 3\cos^2\psi\right)\right)^2, \tag{3.28}$$

$$\Rightarrow \frac{d}{d_0} - 1 = \varepsilon_p + \varepsilon_d^V \approx \varepsilon_p - \frac{2\gamma}{3}\left(1 - 3\cos^2\psi\right). \tag{3.29}$$

This small shear strain formula is in agreement with Singh's result. However, we note that equation 3.24 forms a more general relation between the measurable quantity, d/d_0 and the angle of **G** relative to loading, which does not assume small strains.

To demonstrate the deviation expected from Singh's formula for large shear we show the plots based on Singh's methodology as well one based on equation 3.24. In Singh's formalism it is noted a of a plot of $1 - 3\cos^2\psi$ against $\varepsilon_m = (d - d_0)/d_0$, the measured strain, is linear with gradient $2\gamma/3$.

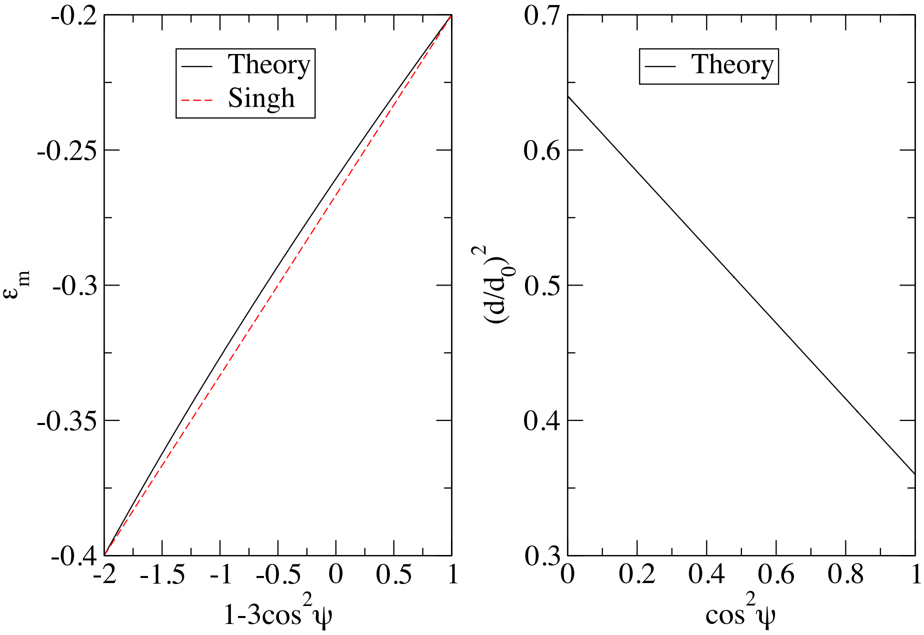

Figure 3.4: Comparison of the theory of section 3.2 with that of Singh. Black lines represent the theory outlined in this work, with the red dotted line in the left panel showing the small strain theory predictions for the same deformation.

Although the theory presented above agrees well with this at low γ, deviations are typically seen for shear strains of 5% and above, a level of shear which can be seen in the elastic compression phase of a shock [88]. It should be noted that even for the case of $\varepsilon_p = -0.267$, $\gamma = -0.1$ shown in figure 3.4, departures of the current theory from Singh's linear equation are minimal. However, if only a small range of $\cos^2\psi$ is accessible experimentally, a linear fit may lead to significant errors of several percent in strain, both volumetric and shear.

The proposed $\cos^2\psi$ against $(d/d_0)^2$ plot is seen to be linear over all $\cos^2\psi$, making it a better candidate for shear strain (and isotropic strain) determination where limited ψ range is covered. In the case $\alpha_{11} \neq \alpha_{22}$, or of non-zero off-diagonal deformation gradient components, both of these analyses fail; in fact for the latter case measured strain is no longer necessarily single-valued in ψ. Here, a full fit to the diffraction pattern using equation 3.11 is required to determine the applied deformation. Since this equation provides a unique set of values for θ_B and ϕ for a given deformation, it is possible to plot theory lines over raw experimental data taken on an area detector at any position, to produce an image that is similar to that in figure 3.2. The full deformation gradient can then be fitted by comparing the theory lines with the experimental data.

3.6 Conclusions

We present a method for predicting the Debye-Scherrer diffraction from samples with arbitrary deformation, and with arbitrary orientation of loading directions with respect to incident x-ray direction. This expression is shown to agree with ray tracing from computationally generated polycrystals, and in the small strain limit with existing theory. However, it is shown that for large shear strain, a more accurate form of analysis can alleviate errors due to incomplete sampling of ψ, providing an easy way to measure strain components even in samples with large strain anisotropies, such as those expected from laser compression. As noted above, deviations from existing small strain theory start at around $\gamma = 0.05$ and are pronounced above $\gamma = 0.1$. Errors of the order of percent in strain can be introduced by assuming a linear, small strain response in the $1 - 3\cos^2\psi$ formalism.

CHAPTER 4

Simulations of In Situ X-ray Diffraction from Uniaxially Compressed Highly Textured Polycrystalline Targets

This section describes a technique for extracting orientation information from a compressed highly textured sample. A method is outlined to calculate the analytic diffraction pattern of a textured material as a function of compression, and its orientation with respect to the x-ray beam. Simulated fibre textured diffraction data are produced from single crystal molecular dynamics simulations, and this technique is applied to simulations of the α–ϵ phase transition in iron, the α–ω transition in titanium, and deformation due to twinning in tantalum. Reproduced from McGonegle *et al*, *J. Appl. Phys.* **118**, 065902 (2015) [30], with the permission of AIP Publishing.

4.1 Background

In the past 50 years, much progress has been made in understanding of the response of both single crystals and polycrystalline matter to both shock and quasi-isentropic compression through *in situ* x-ray diffraction [92, 11, 16, 93, 94, 95, 96, 97, 98, 17, 99, 100, 25, 82, 28, 1]. A number of x-ray diffraction techniques have been developed to monitor material response, including divergent beam geometry [101], white-light Laue diffraction [102], Debye-Scherrer diffraction [10, 92, 12, 11] and the use of energy-dispersive single-photon counting [103]. While studies of both single crystals and polycrystalline matter have been undertaken, in the case of polycrystalline samples very little attention has yet been paid to the role of texture in these uniaxial compression experiments - that is to say the distribution function of grain orientations within a particular polycrystalline specimen. A number of manufacturing methods, such as rolling and epitaxial growth, result in characteristic textures due to the way in which the materials have been processed. This texture has an influence on a range of physical properties such as strength, electrical conductivity and wave propagation [48]. Therefore texture plays an important role in understanding material response.

Furthermore, whilst the texture of a sample will influence its response to rapid uniaxial compression, it will also have a profound influence on the way in which the sample diffracts. As certain grain orientations are more likely to occur than others, the intensity of a particular Debye-Scherrer ring (corresponding to a certain set of Miller indices) will have a strong azimuthal dependence, and this dependence can in turn be used to extract texture information. Indeed, significant static studies of the texture of polycrystalline samples have been undertaken with synchrotron sources for many years [49, 50, 48, 51, 52, 53, 54]. Wenk and co-workers provide an overview of the use of synchrotrons in such texture analysis [50]. While the texture of a material is often represented by a set of pole figures which can be measured directly via x-ray diffraction, prediction of anisotropic material properties requires knowledge of the full orientational distribution function (ODF). The ODF gives the probability of a crystallite having a given orientation, therefore provides a complete description of the texture of the sample. Pole figures, being a 2D projections of the ODF, result in some texture information being lost, although methods have been developed to obtain an approximate ODF from multiple pole figures [104, 50, 105, 106]. More recently, techniques have been developed to obtain an estimate of the ODF from a single 2D Debye-Scherrer pattern [107].

Given that the preferred orientation defined by texture links both the diffraction patterns observed and the sample response, this suggests is may be possible to gain specific information via *in situ* diffraction studies of samples with a known, well-defined texture. For example, bulk rotations of the crystal lattice, or changes in the crystal structure, such as Martensitic phase changes, will result in an altered texture that could be used to distinguish between different mechanisms of atomic rearrangement. This reorientation has been observed in previous work using both neutron sources [108] and synchrotrons [50, 54], although only at relatively modest pressures.

Ideally, we would like to understand the detailed response to shock compression of samples as a function of their ODF, and to then predict the resultant diffraction patterns. We outline in section 4.2 the method by which this could in principle be done, for the Voigt limit. However, for simplicity we chose to restrict ourselves to crystals that are highly fibre textured - that is to say, all of the grains within the sample initially have very similar orientations with respect to a single axis (the fibre axis), only deviating slightly in angle from that of a high-symmetry direction. As all of the grains have similar orientations along a given axis, which we also take to be the axis of compression, we might expect that we can, to a reasonable approximation, model certain aspects of their response to shock or quasi-isentropic compression using single-crystal parameters. In particular, when determining how the material will respond to compression and shear, we assume that the elastic stresses, supported by elastic strains, can be calculated by using elastic constants appropriately chosen to mimic single crystal response along the pertinent directions. In terms of x-ray diffraction, however, the finite range of orientations determined by the ODF is such that a monochromated, non-divergent incident x-ray beam can diffract from a reasonably large subset of the grains, both in the shocked and unshocked case. A similar approach to that outlined above has recently been used to observe, via femtosecond diffraction, the ultimate compressive strength of copper subjected to shock compression at strain rates of order 10^9 s^{-1} [1]. We shall show that breaking the symmetry of the system, such that the direction of the incident x-rays and the target normal (parallel to the compression direction) are no longer antiparallel, allows us to determine specific information about the system under study.

4.2 Method

In the previous section, we showed how to calculate the position of Debye-Scherrer rings from a polycrystal strained by an arbitrary deformation gradient in the Voigt limit. This assumed the sample was assumed to be isotropic in texture, and thus satisfying Equation 3.5 was deemed a sufficient condition for diffraction to occur. However, a non-isotropic ODF places further constraints on the possibility of diffraction for a given Bragg angle and azimuthal position around the Debye-Scherrer ring, as the ODF provides the measure of the probability of finding a crystal with a given $\mathbf{G_0}$ existing in the original unstrained sample. The route forward for simulating diffraction for a crystal with known original ODF under a known arbitrary deformation gradient is now clear: we use the ODF to determine the probability of a given crystallite having the appropriate $\mathbf{G_0}$ existing within the sample, we then determine $\mathbf{G}$ from Equation 3.5 (and hence $\mathbf{k}$ from the Laue condition), and use ray-tracing to propagate the diffracted beam to the detector assuming that the intensity is proportional to the probability of finding the original $\mathbf{G_0}$, as determined by the ODF, and taking into account factors such as multiplicity.

Although the above approach is general, we will restrict our study to the particular case of a simple fibre texture where the crystallites have nearly identical orientation in the axial direction, but close to random radial orientation. Our motivations for this are due to the fact that this allows us to treat the mechanical response of a polycrystal with sufficiently large grains to be well-approximated by that of a single crystal with orientation aligned with the fibre axis and that the technique of fibre diffraction under ambient conditions is well established [56, 57]. Furthermore, recent experiments conducted at LCLS using uniaxially compressed samples have employed targets with this type of texture, [1] and the thin films that have hitherto been used in these experiments often grow with such preferential orientation. Fibre textured samples have a greatly simplified ODF. For the case of perfect fibre texture, each crystallite has a single crystallographic direction, the fibre orientation, $\mathbf{v_1}$, associated with the reciprocal lattice vector (h_1, k_1, l_1), which for all crystallites are aligned parallel to the sample normal, $\mathbf{n}$. Each grain is then deemed to possess a random orientation when rotated about the axis, $\mathbf{v_1}$. If we consider a particular plane within a crystallite, with miller indices (h_2, k_2, l_2) (which are the same set of miller indices associated with $\mathbf{G_0}$) to which the reciprocal lattice vector is $\mathbf{v_2}$, then the value of $\hat{\mathbf{v}}_\mathbf{1} \cdot \hat{\mathbf{v}}_\mathbf{2}$ will be a constant, where $\hat{\mathbf{v}}_\mathbf{i} = \mathbf{v_i} / |\mathbf{v_i}|$. We denote the angle between $\mathbf{v_1}$ and $\mathbf{v_2}$ to be μ, such that $\hat{\mathbf{v}}_\mathbf{1} \cdot \hat{\mathbf{v}}_\mathbf{2} = \cos\mu$. To understand what effect this texture has on the diffraction pattern, we can consider the approach developed by Polanyi [56, 57, 55], shown in Figure 2.19. We can represent the possible orientations of $\mathbf{G_0}$ in an untextured sample as points on the surface of a sphere, known as the Polanyi sphere. As a material is compressed by deformation gradient $\mathbf{F}$, the Polanyi sphere deforms in reciprocal space by $(\mathbf{F}^T)^{-1}$. Therefore, while a hydrostatic compression only changes the size of the Polanyi sphere, for the case of anisotropic strains, the Polanyi sphere is deformed into an ellipsoid. By finding the intersection of the Polanyi sphere and Ewald sphere, we can determine which orientations meet the Laue condition, according to Equation 3.5. However, in a fibre textured sample, only some of these grain orientations are present. The set of possible $\mathbf{v_2}$ vectors are shown as a black ring on the Polanyi sphere, and therefore $\mathbf{G_0}$ is constrained to be on this ring, which we can represent mathematically as:

$$\hat{\mathbf{v}}_\mathbf{1} \cdot \hat{\mathbf{G}}_\mathbf{0} = \hat{\mathbf{v}}_\mathbf{1} \cdot \hat{\mathbf{v}}_\mathbf{2} = \cos\mu. \tag{4.1}$$

These rings will also deform when the sample is compressed, and the diffraction will occur where these deformed rings intersect with the surface of the Ewald sphere. The additional constraint of fibre texture means that the Debye-Scherrer pattern is not a ring pattern, but an array of points defined by simultaneously satisfying Equations 3.5 and 4.1 (see Figure 2.19). Note that this condition does not take into account multiplicity, and therefore one

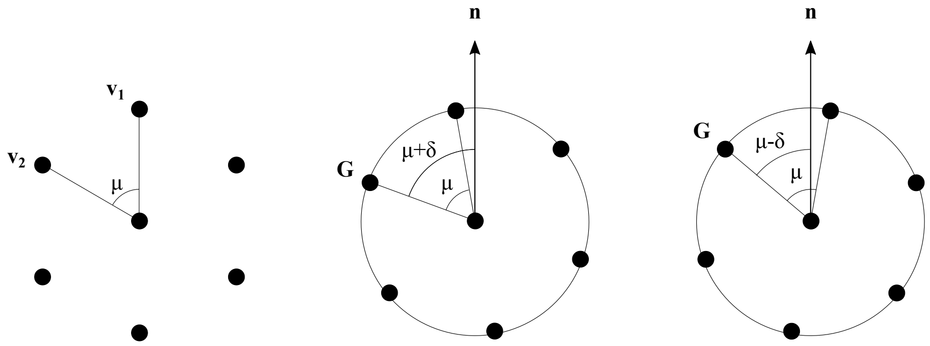

Figure 4.1: A schematic showing a slice through the Polanyi sphere in reciprocal space. We see that with a texture width of δ, that the angle between the sample normal $\mathbf{n}$ and $\mathbf{G}$ must be between $\mu - \delta$ and $\mu + \delta$, where μ is $\hat{\mathbf{v}}_\mathbf{1} \cdot \hat{\mathbf{v}}_\mathbf{2}$.

must consider this condition for each member of $\mathbf{v_2}$ in the $\{h_2, k_2, l_2\}$ family, since they do not necessarily result in the same values of $\hat{\mathbf{v}}_\mathbf{1} \cdot \hat{\mathbf{v}}_\mathbf{2}$. However, real fibre texture samples contain crystallites that are not perfectly aligned axially. We therefore need to consider $P(\mathbf{v})$, the volume fraction of crystallites that have a reciprocal lattice vector $\mathbf{v}$). As most grains will still have $\mathbf{v_1}$ closely aligned to the sample normal, $P(\mathbf{v_1})$ will be a rapidly decreasing function of $\hat{\mathbf{v}}_\mathbf{1} \cdot \hat{\mathbf{v}}_\mathbf{n}$, where now $\hat{\mathbf{v}}_\mathbf{n} =< \hat{\mathbf{v}}_\mathbf{1} >$. Since each crystallite will have the same $\mathbf{v_2} \cdot \mathbf{v_1}$ found in a single crystal, $P(\mathbf{v_2})$ should have a similar functional form, and in fact $P(\mathbf{v_2}) \propto P(\mathbf{v_1})$ subject to the $\mathbf{v_2} \cdot \mathbf{v_1}$ constraint. The diffraction condition is once more defined by simultaneously satisfying Equations 3.5 and 4.1, but now the intensity of the diffraction is proportional to $P(\mathbf{v_1})$. We can represent the effects of a finite texture width by broadening the rings on the Polanyi sphere into annuli (see Figure 2.19). As a result, our diffraction pattern broadens out into series of arcs, rather than points, with the width of the arcs providing information on the texture width of the sample. For the sake of simplicity in our simulations here we assume that the volume fractions of crystallite orientations are uniform over a small range of angles, i.e. $P(\mathbf{v_1}) = C$, a constant, for $|\arccos(\hat{\mathbf{v}}_\mathbf{n} \cdot \hat{\mathbf{G}}_\mathbf{0}) - \mu| \leq \delta$, and $P(\mathbf{v_1}) = 0$ for $|\arccos(\hat{\mathbf{v}}_\mathbf{n} \cdot \hat{\mathbf{G}}_\mathbf{0}) - \mu| > \delta$. The two limiting cases where $\arccos(\hat{\mathbf{v}}_\mathbf{n} \cdot \hat{\mathbf{G}}_\mathbf{0}) - \mu$ is either $+\delta$ or $-\delta$ are shown in Figure 4.1. Note that by changing the x-ray energy or the sample orientation, which varies the size of Ewald sphere or rotates the Polanyi sphere respectively, the position of the arcs on the Debye-Scherrer ring also change, and that by varying these parameters, different parts of reciprocal space can be interrogated.

4.3 Molecular Dynamics Simulations

One advantage of the fibre texture discussed above is that one knows (to within the texture width) the crystallographic orientation of grains with respect to an applied planar compression front. This is particularly important as crystallite orientation can drastically alter the material response under uniaxial loading [100, 84, 109, 110]. In the case that grain size is comparable to sample thickness [1], one can approximate the response of the sample as being close to that of a suitably oriented single crystal. This is particularly pertinent if one wishes to compare results with those of molecular dynamics, where state of the art polycrystalline simulations are still generally limited to grain sizes of 5-100 nm [111, 24, 112, 113, 114], far below the grain sizes of typical experimental samples.

In order to relax the requirements on computational power, we present a method for simulating the response of a fibre textured target by manipulation of a single crystal simulation. We do this by first performing a 3D Fourier Transform (FT) of the computed electron density of the single crystal [64]. This provides us with a momentum space representation of the lattice which describes the allowed scattering vectors for diffraction.

Working with the intensity of this FT, we first note that any polar dependence around the compression axis can be neglected due the random rotational distribution of grains in a fibre textured sample. Considering a cylindrical geometry, we therefore produce a 2D representation of the FT, which flattens the data into its (ρ, z) components, effectively integrating around ϕ. In the case of a perfect (zero texture width) fibre texture, this 2D representation correctly describes all scattering.

For the case of finite texture width, one can imagine that the misorientations of the grains are simply related to a rotation about the origin of the 2D representation, and so to mimic the width we sum rotated representations for angles between $\pm\delta$. This new representation necessarily still retains the cylindrical symmetry required for fibre texture, but correctly accounts for the distribution of grain alignments. Of course, as δ becomes larger than a few degrees, the underlying assumption that all grains react in a similar manner to a well aligned single crystal will break down. However, for simplicity, we will assume suitably small texture widths of $\approx 5^\circ$, as this was found to be close to the upper limit of applicability of the single crystal approximation.

One can now raytrace simulated diffraction patterns directly from this 2D representation by only considering the (ρ, z) component of the scattering vectors expressed in this cylindrical target geometry.

4.4 Results

We now present results for three different fibre textured polycrystals subject to uniaxial compression: iron with a [001] fibre texture, titanium with [0001] fibre texture, and tantalum with [001] and [110] fibre textures. For all three crystals we make assumptions about the deformation mechanisms, and use the approach of section 4.2 to predict diffraction patterns. For two of the cases - iron and tantalum - we also compare our calculations with diffraction patterns simulated using the method of molecular dynamics, as outlined in section 4.3.

4.4.1 α–ϵ Phase Transition in [001] Iron

The α–ϵ phase transition in iron is an example Martensitic transformation, characterised by a collective movement of atoms across distances that are typically smaller than a nearest-neighbour spacing. These type of transitions are well suited to laser compression studies, since the timescales on which they occur are comparable to the short pulses that can be attained in laser experiments. Importantly, for these non-diffusional transitions, an orientational relationship (OR) exists between the two phases. While the OR does not uniquely determine the mechanism by which the phase transition occurs, it can significantly reduce the number of candidate mechanisms. The ability to measure the OR *in situ* is therefore highly desirable.

As an example of determination of an OR, we take the case of [001] oriented iron, where the phase transition mechanism is well understood. Molecular dynamic simulations undertaken by Kadau *et al.* aimed to understand iron's bcc-hcp shock induced phase transition [23]. The results of these investigations were later reproduced with remarkable fidelity in experimental x-ray diffraction studies [17, 99]. In both MD and experiment, the OR was described as $[001]_{\mathrm{bcc}} \,||\, [2\bar{1}\bar{1}0]_{\mathrm{hcp}}$, $[110]_{\mathrm{bcc}} \,||\, [0002]_{\mathrm{hcp}}$ [23] . One can therefore consider this OR as reorienting a fibre textured sample from $(002)_{\mathrm{bcc}}$ to $(2\bar{1}\bar{1}0)_{\mathrm{hcp}}$.

Following Kadau, we simulate a 100x100x800 cell (288x288x2301Å) iron single crystal shocked along the [001] direction by 0.7 km s^{-1} piston using

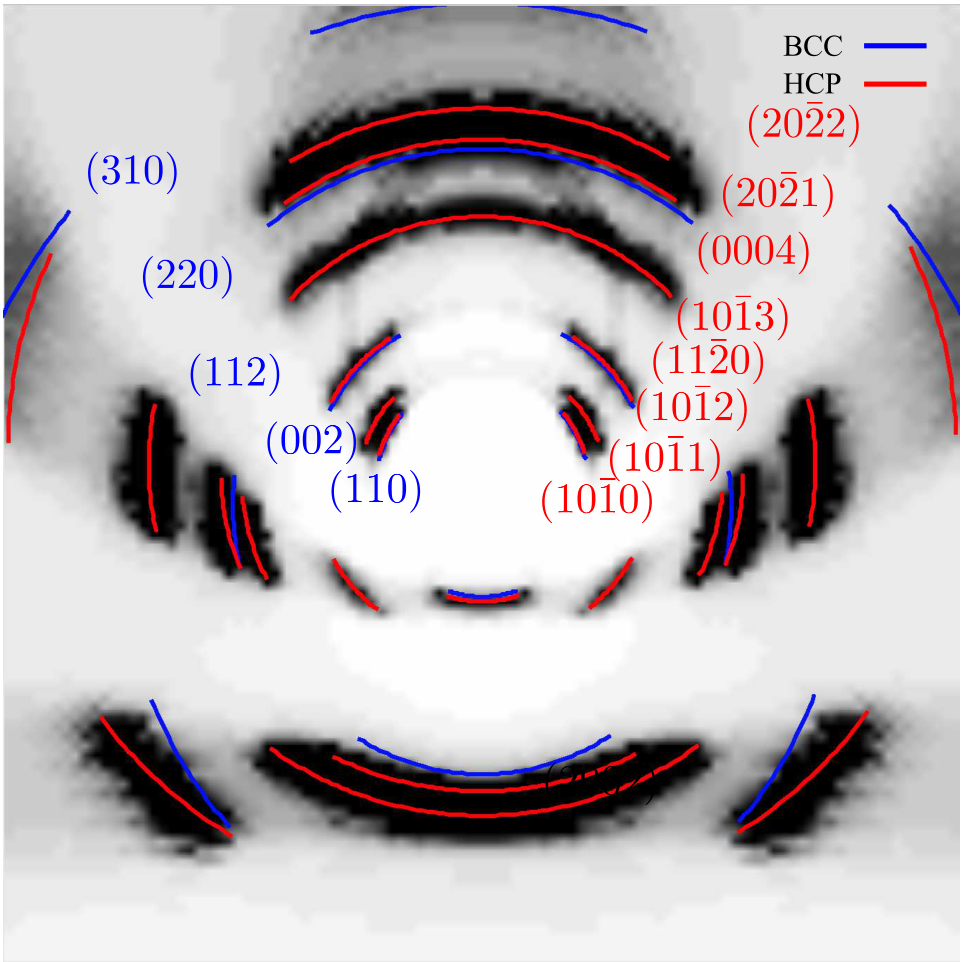

Figure 4.2: A simulated ray trace of diffraction from a [001] fibre textured polycrystalline hcp Fe formed under shock compression. The blue overlaid lines show the positions of arcs from uniaxially compressed bcc, while the red lines show the positions of arcs from hcp with OR $[001]_{\mathrm{bcc}} \,||\, [2\bar{1}\bar{1}0]_{\mathrm{hcp}}$, $[110]_{\mathrm{bcc}} \,||\, [0002]_{\mathrm{hcp}}$. For clarity the x-ray energies used to trace the bcc and hcp overlays were offset by 1%. The corners of the detector are located at a scattering angle $2\theta = 74.2°$.

Table 4.1: The three ORs that correspond to various proposed mechanisms of the $\alpha - \omega$ phase transition in [0001] Titanium

Variant	Orientational Relationship	Ref
I	$(0001)_\alpha \,\|\|\, (10\bar{1}1)_\omega$, $[10\bar{1}0]_\alpha \,\|\|\, [\bar{1}011]_\omega$	[115, 116, 117]
II	$(0001)_\alpha \,\|\|\, (1\bar{2}10)_\omega$, $[1\bar{2}10]_\alpha \,\|\|\, [0001]_\omega$	[115, 118]
Zong	$(0001)_\alpha \,\|\|\, (10\bar{1}0)_\omega$, $[10\bar{1}0]_\alpha \,\|\|\, [11\bar{2}3]_\omega$	[110]

the same Voter-Chen potential used in Kadau's work [23]. For this piston velocity, the material does not reach the 18.4% uniaxial compression needed to create ideal hcp, instead reaching only 13.8% [99], resulting in an anisotropically strained hcp structure. A 3D FT was performed on a section of the material behind the shock front. The FT was modified to mimic that of a fibre textured polycrystal, using the method described in section 4.3. Figure 4.2 shows the resultant ray trace [64] for a detector in transmission geometry, using a 12 keV x-ray source and with the sample normal rotated at an angle 30° to the incoming x-rays. The overlaid red lines show the predicted diffraction pattern (using the methods of section 4.2) of strained hcp iron described above, with a c/a ratio of 1.73, a texture direction along $[11\bar{2}0]_{\text{hcp}}$ and a textured width of 5°. The blue lines show the pattern from 13.8% uniaxially compressed bcc. As expected, there is agreement between the raytrace and predictions from the molecular dynamics simulations, supporting the validity of the approach outlined in section 4.2.

4.4.2 α–ω Phase Transition in [0001] Titanium

The group IV transition metals titanium (Ti), zirconium (Zr) and hafnium (Hf) have a hexagonal close-packed structure (α) under ambient conditions, but exhibit a Martensitic phase transition to another hexagonal structure (ω) under high pressure. Although the α–ω transition is well established, the

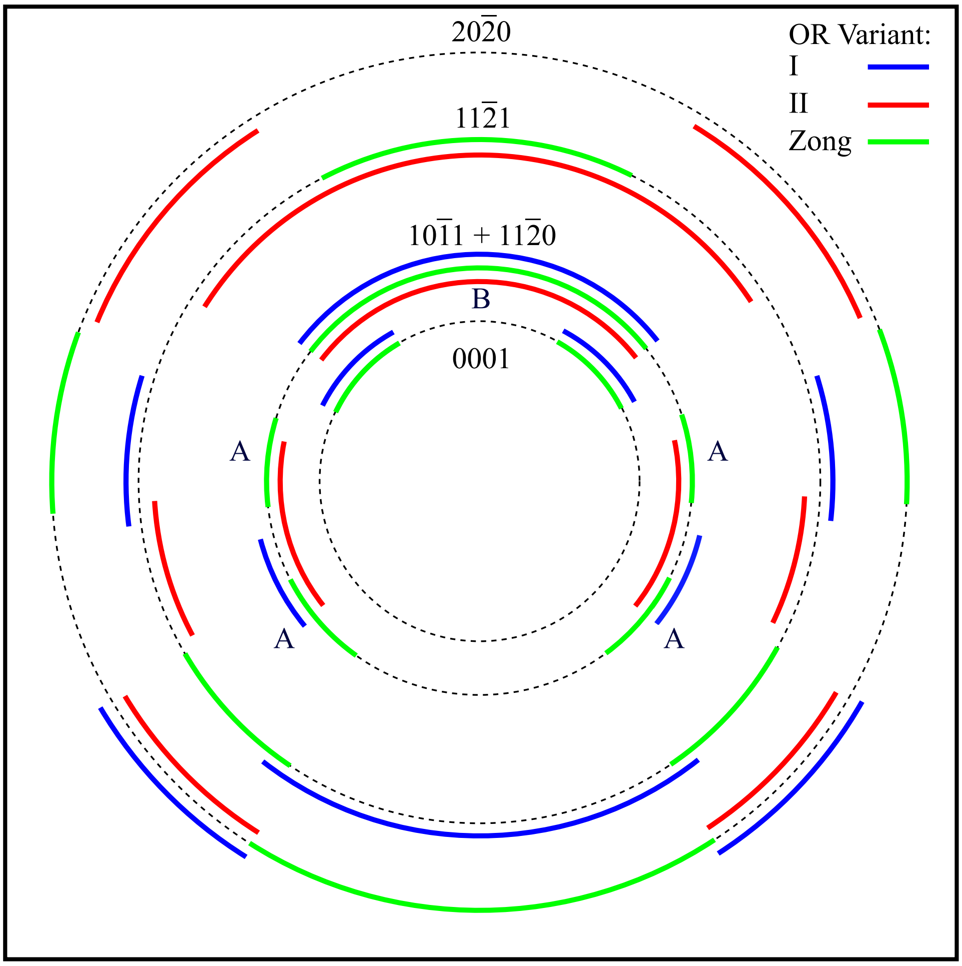

Figure 4.3: The predicted diffraction pattern using 7.5 keV x-rays from the ω phase of a shocked [0001] fibre textured Ti sample, with the sample normal rotated at an angle 25° to the incoming x-rays. The ORs of the variants I, II and Zong are given in Table 4.1. The green arcs labelled A and B correspond to the $\{10\bar{1}1\}$ and $\{11\bar{2}0\}$ sets of planes respectively. The corners of the diagram are located at a scattering angle $2\theta = 70.5°$.

mechanism by which it occurs, and therefore the OR between the phases, is still not fully understood, especially under different loading conditions. A summary of the ORs for various proposed mechanisms is given in Table 4.1. The first two ORs were proposed by Usikov and Zilbershtein [115] in a TEM study of statically compressed Zr and Ti, by arguing that the transition occurs via an intermediate β phase, and are usually referred to as Variant I and II. Earlier work by Silcock [118] on the ω phase in Ti alloys proposed a different direct mechanism which corresponds to the Variant II OR. Later computational work by Trinkle [116] demonstrated that a new mechanism, known as TAO-1, had a lower energy barrier than that proposed by Silcock. This new mechanism produced the Variant I OR. Experimental work by Song and Gray [117] observed the OR $(0001)_\alpha \,||\, (10\bar{1}1)_\omega$, $[10\bar{1}0]_\alpha \,||\, [11\bar{2}3]_\omega$, although independent analysis re-examining this data led to the conclusions that it is actually a subset of Variant I [119]. We have therefore associated Song and Gray's work with Variant I in Table 4.1.

Molecular dynamics simulations performed by Zong *et al.* [110] found that Ti shocked along the [0001] direction resulted in a mechanism that gave an OR differing from both Variant I and II, as listed in the table. Note that each OR results in a different fibre texture direction for the ω-phase for uniaxial compression of an initially fibre textured α-phase target, and thus a target with the normal tilted with respect to the incident x-ray beam is well suited to provide some discrimination between variants, therefore providing some insight into possible transformation mechanisms.

The work by Zong [110] found that Ti shocked along the [0001] direction by a piston with a velocity of 0.9 km s^{-1} resulted in transformation to the ω phase, with lattice parameters $a_\omega = 4.61\,\text{Å}$ and $c_\omega = 2.82\,\text{Å}$. Using these values, we calculate the diffraction pattern from the ω phase of a shock-compressed [0001] sample of Ti with an angular texture width of ±5°. The sample normal is set at angle 25° to the incoming x-rays, which have an energy of at 7.5 keV. The predicted diffraction patterns for each of the possible variants are shown in Figure 4.3. The blue, red and green lines correspond to the diffraction from ω material of Variant I, Variant II and the Zong OR respectively, while the dotted black line corresponds to the diffraction from an untextured polycrystalline sample. For clarity, the blue lines have been slightly offset outside the true Debye-Scherrer rings, while the red lines have been slightly offset inside. A clear difference can be seen in the diffraction patterns for the different variants, thus allowing the OR and hence a subset of mechanisms to be determined by the azimuthal position of the diffracting arcs around the Debye-Scherrer ring. It is important to note that the ability to discriminate clearly between all three ORs is not guaranteed, and relies on a judicious choice of both x-ray energy and tilt angle.

Figure 4.3 also demonstrates that lines with similar *d*-spacings do not necessarily appear at similar azimuthal positions. For example in an ideal ω crystal, the $\{10\bar{1}1\}$ and $\{11\bar{2}0\}$ planes have the same spacing and are therefore completely unresolvable by powder diffraction from an untextured sample. However, since these planes form different angles to the sample normal, within a textured sample their corresponding arcs appear at different azimuthal angles around the Debye-Scherrer ring, allowing them to be resolved. This is shown in Figure 4.3, where the green arcs labelled A correspond to the $\{10\bar{1}1\}$ set of planes, while the green arc labelled B corresponds to the $\{11\bar{2}0\}$ set of planes. By resolving these two arcs, we are able to gain information that cannot be obtained via powder diffraction from an untextured sample; in this case on any small departure from the ideal c/a ratio. We note that it is only possible to resolve lines with similar *d*-spacings if the angle between G-vectors of each of the planes and the sample normal is significantly different.

4.4.3 Twinning in [001] and [110] Tantalum

Tantalum provides an appealing case to study, owing to its multitude of competing plasticity mechanisms (a combination of dislocation and deformation twinning mediated responses). This is of particular interest, as Debye-Scherrer diffraction in polycrystalline samples with completely random texture cannot distinguish between slip and twinning. Most experimental work into twinning under uniaxial dynamic compression has been performed using either explosive lenses or gas guns [120, 121, 122, 123]. However, to date, time resolved laser diffraction experiments have failed to yield any evidence of twinning *in situ*, although residual twinning has been observed in laser driven shock recovery experiments [124, 125].

As with phase transitions, the reorientation of the lattice caused by twinning will result in a different crystallographic direction being oriented along the fibre direction. This may, in turn, lead to a signature in the diffraction pattern. A similar technique using neutron diffraction has been used to observe twinning in magnesium, which occurs at much lower pressures than in tantalum [108]. Figures 4.4 and 4.5 demonstrate how twinned material will produce new diffraction arcs. Figure 4.4 shows the reciprocal lattice for a [001] oriented Ta grain. Note that the reciprocal lattice of a BCC lattice is an FCC lattice. The red and blue spots show neighbouring planes of reciprocal lattice points. If we assume the crystal twins on the (112) twin plane, the grain will reorient so its [221] direction will be along the sample normal. Figure 4.5 shows the reciprocal lattice of the untwinned and twinned orientation in cylindrical coordinates. Each spot on this diagram will correspond to a different ring on the Polanyi sphere and therefore will also correspond to a different diffraction arc. The twinned orientation results in many new spots and the corresponding diffraction arcs can be used to experimentally

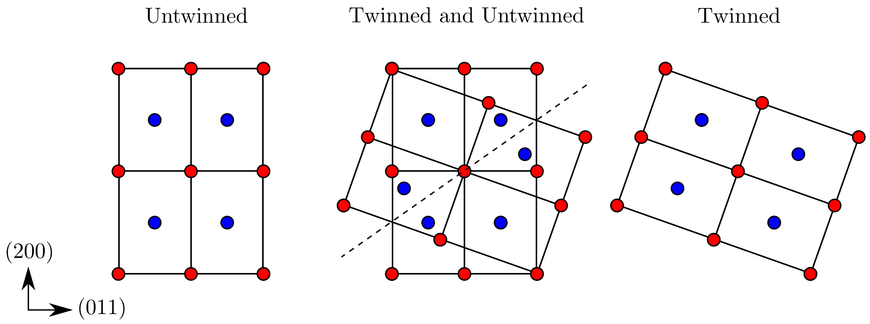

Figure 4.4: The reciprocal lattice of an untwinned and twinned [001] Ta crystal. Red and blue spots correspond to neighbouring planes of reciprocal lattice points.

measure twin fraction.

Molecular dynamics simulations performed by Higginbotham *et al.* have predicted a significant twinning fraction in [001] tantalum under shock compression [85]. In that work, the sample was found to be almost completely twinned when compressed by a piston with a velocity of 0.9 km s^{-1}, corresponding to a uniaxial compression in the elastic wave by 18%. The authors noted that after an initial uniaxial compression of 18.4%, twinning could be achieved by shuffling alternating $(\bar{1}12)$ planes in the $\langle 111 \rangle$ direction. They therefore proposed this to be the mechanism by which the twinning occurred, with the material reaching its final state via elastic relaxation, although they caution that, given the relatively simple nature of the potential used, they do not claim to exactly model what will occur in practice in shocked Ta. However, the observed shuffling provides a possible mechanism for how twinning of bcc materials may occur under shock compression.

We repeated the simulations in this work, using a 100x100x800 cell (330x330x2644Å) Ta single crystal, modelled using the EFS potential [126],

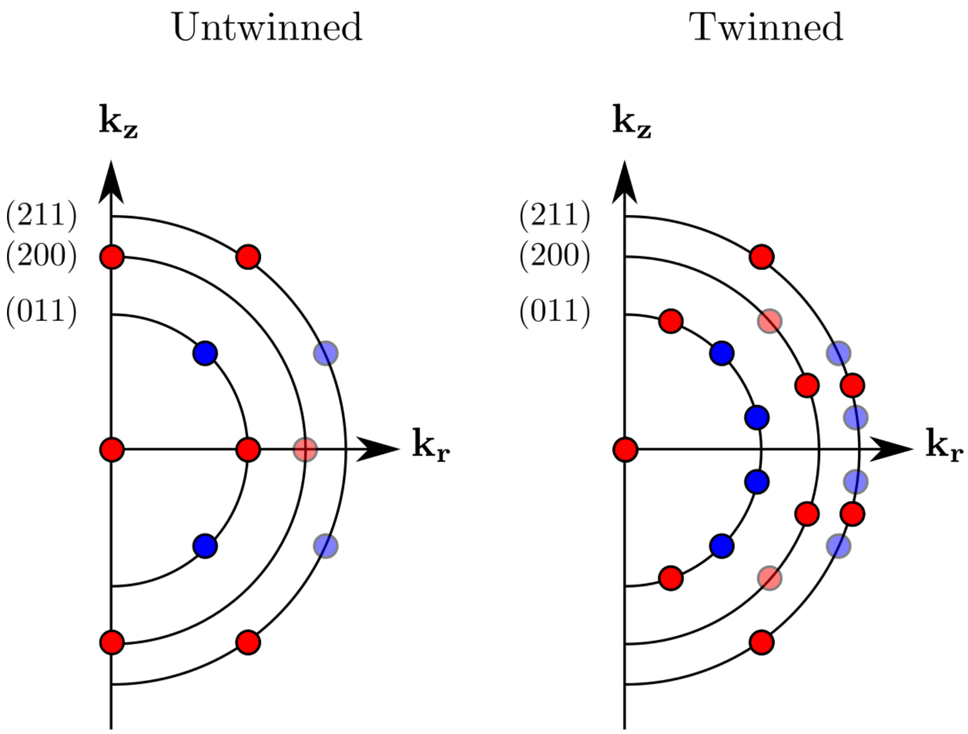

Figure 4.5: The reciprocal lattice of an untwinned and twinned [001] Ta crystal in cylindrical coordinates. Semi transparent spots correspond to reciprocal lattice points two planes above the full opacity spots.

and shocked along the [001] direction by a piston travelling at 0.9 km s^{-1}. The per atom structure factor (PASF) [85] was used to distinguish between twinned and untwinned material in the plastically deformed material behind the shock front. The PASF code performs a FT on all the atoms within a spherical cutoff of each atom. By comparing the intensities of k points corresponding to untwinned and twinned orientations, it is possible identify regions of twinned and untwinned material. A 3D FT was performed on a stable region within the plastically deformed material behind the shock front, as well as the twinned region separately, and both were modified in the way described in section 4.3. The diffraction pattern was simulated assuming a 12 keV x-ray source, with the angle between the incoming x-rays and the sample normal being 25°. The results are shown in Figure 4.6. For the case of slip, while small rotations of the crystal lattice have been observed [26], no large reorientation is expected, and thus the fibre orientation will remain close to [001]. However, by comparing the observed and predicted positions of the diffraction arcs for a [001] textured sample including the strains described above (shown in Figure 4.6a), it is clear that there has been a significant reorientation of crystallites within the sample, indicative of twinning.

In Figure 4.6b we plot the predicted diffraction pattern using the methods of section 4.2 assuming that the sample has undergone twinning, and is subject to the longitudinal and transverse strains noted above. In order to find the diffraction pattern resulting from the shuffling mechanism above, one must consider how this affects the lattice vectors of the crystal. The sample is first compressed uniaxially along the z axis by 18.4%. The shuffling then has the effect of causing the crystal to be reflected in the (112) twinning plane. Note that as the crystal is uniaxially compressed, this

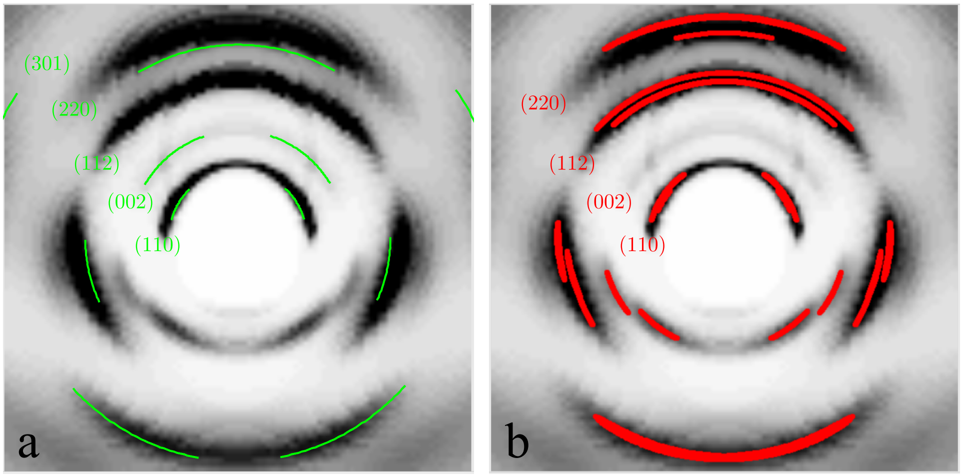

Figure 4.6: Simulated diffraction from a [001] fibre textured polycrystalline Ta under shock compression. Overlaid are the predicted diffraction patterns for: (a). the untwinned case, with elastic strains of $\epsilon_t = -0.029, \epsilon_l = -0.136$ shown in green and (b) the twinned case, with elastic strains of $\epsilon_t = -0.052, \epsilon_l = -0.109$, shown in red. The corners of the detector are located at a scattering angle $2\theta = 66.3°$.

causes the [001] direction to be reflected to the [111] direction of the compressed crystal, rather than the [221] direction expected under hydrostatic conditions (see Figure 6 of Higginbotham *et al.* [85]). Lastly, the twinned material returns towards the hydrostat, by relaxing along the longitudinal direction and compression along the transverse directions in the new rotated coordinates. The final longitudinal and transverse strains were measured to be -0.109 and -0.052 respectively, giving a deformation gradient of:

$$\mathbf{F} = \begin{pmatrix} 0.7110 & -0.2370 & -0.5456 \\ -0.2370 & 0.7110 & -0.5456 \\ -0.5805 & -0.5805 & -0.4455 \end{pmatrix} \tag{4.2}$$

However, in the textured sample, the effect of a finite texture width

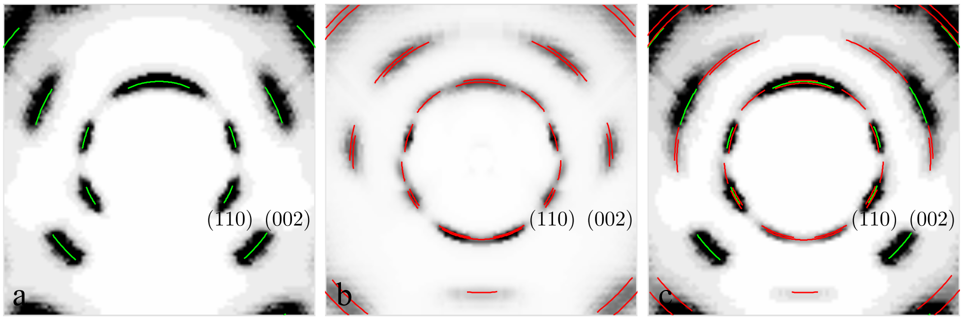

Figure 4.7: Simulated diffraction from a [110] fibre textured polycrystalline Ta under shock compression. Overlaid are the predicted diffraction patterns for: (a). the untwinned case, with elastic strains of $\epsilon_t = -0.045, \epsilon_l = -0.075$, shown in green, (b) the twinned case, with the $[\bar{9}22]$ direction close to the compression axis, shown in red, and (c) both the untwinned and twinned case together. The corners of the detector are located at a scattering angle $2\theta = 51.3°$.

must also be considered. In this case, the initial compression occurs at a slight angle to the texture direction, which results in a slightly different orientation of the twinning plane. The crystal is then reflected in this altered twinning plane and relaxes as before. To create the predicted diffraction pattern, the lattice vectors of many crystallite orientations within the desired texture width were deformed by the method given above. These were then used to calculate deformed reciprocal lattice vectors, and thus the resultant diffraction pattern.

Excellent agreement can be seen between the analytic solution, and the MD simulation, demonstrating that twinning has occurred, although slight differences can be observed which are due to the small angle assumptions used in section 4.3 to simulate the 3D FT of a fibre textured target. Additionally, there are some very weak arcs in the data corresponding to plastically compressed material (Figure 4.6a). The ratio of intensities of lines from twin and slip deformed material is indicative of the twin fraction.

While most theoretical work on twinning in Ta has concentrated on the

[001] direction, recent MD studies by Ravelo *et al.* have suggested shocking along the [110] direction may be more favourable for deformation twinning, due to the lower observed shear stress threshold for twin nucleation [63]. This agrees with gas gun recovery work on Ta single crystals, which found a significantly higher twin volume fraction in shocks along [110], compared to the [001] and [111] directions [122]. Furthermore, as the [110] direction is the preferred direction for epitaxial growth of fibre textured thin films, this direction is particularly well suited for this technique. The [110] orientation exhibits two types of $\{112\}\langle111\rangle$ twin systems, which result in different fibre orientations. Under hydrostatic conditions, the first type causes no change in the fibre texture, while the second causes a reorientation to the $[\bar{4}11]$ direction. However, only the second type has non-zero Schmid factors, and it is therefore assumed that only twins of this type occur. It follows that diffraction arcs corresponding to a [110] fibre orientation are from the untwinned material, while arcs corresponding to fibre orientations close to the $[\bar{4}11]$ type directions are from the two twinned variants. Figures 4.8 and 4.9 show the reciprocal lattices an untwinned and twinned [110] Ta sample in cartesian and cylindrical coordinates respectively.

We repeated the simulations in this work, using a 100x100x800 cell (330x330x2644Å) Ta single crystal, modelled using Ravelo's Ta1 EAM potential [63], and shocked along the [110] direction by a piston travelling at $0.62\,\mathrm{km\,s^{-1}}$. Again the PASF was used to distinguish between twinned and untwinned material, and a 3D FT was performed on each region separately. In the twinned material, the $[\bar{9}22]$ direction of the compressed crystal is close to the compression axis, which is consistent with twinning after an initial uniaxial compression, similar to the [001] case. By extracting the reciprocal lattice vectors from the FT, we can therefore deduce a deformation gradi-

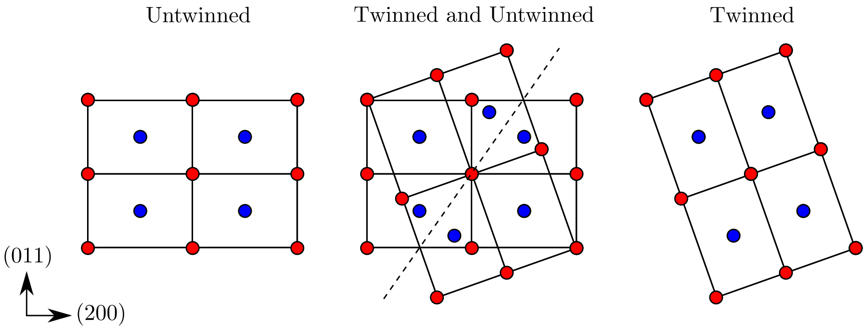

Figure 4.8: The reciprocal lattice of an untwinned and twinned [110] Ta crystal. Red and blue spots correspond to neighbouring planes of reciprocal lattice points.

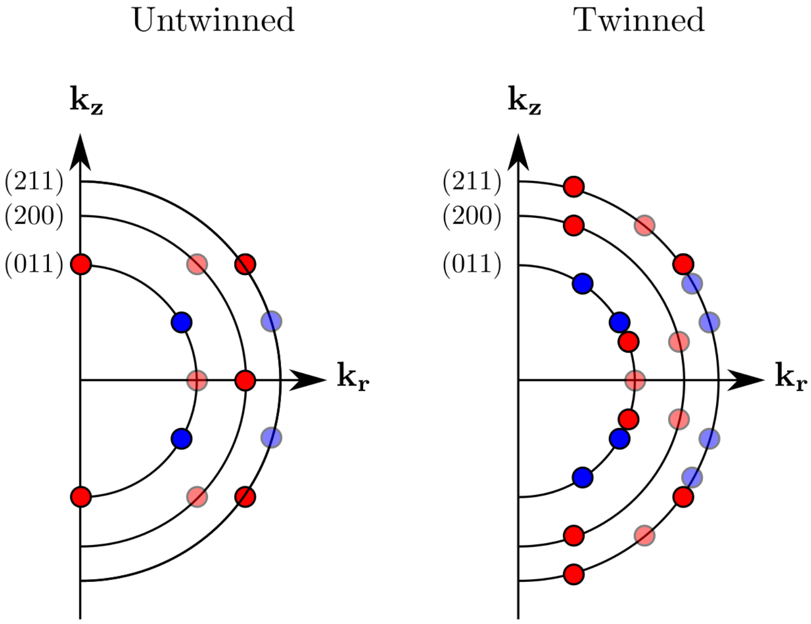

Figure 4.9: The reciprocal lattice of an untwinned and twinned [001] Ta crystal in cylindrical coordinates. Semi transparent spots correspond to reciprocal lattice points two planes above the full opacity spots.

ent in reciprocal space. This is equal to $(\mathbf{F}^T)^{-1}$, so by applying the inverse transpose, we find the deformation gradient of:

$$\mathbf{F} = \begin{pmatrix} -0.2949 & -0.0009 & 0.9006 \\ -0.0319 & 0.9825 & 0.0116 \\ 0.8930 & -0.0010 & 0.2762 \end{pmatrix} \tag{4.3}$$

The diffraction pattern was simulated assuming a 10 keV x-ray source, with the angle between the incoming x-rays and the sample normal being 45°. The results are shown in Figure 4.7. Since the twinning mechanism in [110] Ta is not well understood, the predicted pattern was produced for the structure found measured with the FT. Again, good agreement is seen between the analytic solution and the MD simulation, although in this case, there are strong arcs corresponding to both twinned and untwinned material, suggesting a significant amount of both are present in the sample.

To test how well the twin fraction can be measured via diffraction, both the simulation above, as well as another performed with a piston velocity of 0.6 km s^{-1}, were analysed with the PASF code to determine the twin fraction. The same regions of the two simulations were raytraced at 9.6 keV using the method provided above to generate simulated diffraction patterns from a [110] fibre textured polycrystal, assuming a 35° tilt. The azimuthal variation in intensity of the (110) lines is shown in figures 4.10 and 4.11.

The peaks between 50° and 150° are fitted with four pseudo-Voigt profiles. The peak at 95° corresponds to only the twinned material, while the peak at 65° corresponds to both twinned and untwinned material. However, there are two different azimuthal grain orientations that contribute to the 65°, while the 95° only has one. Therefore, we are able to find the twin

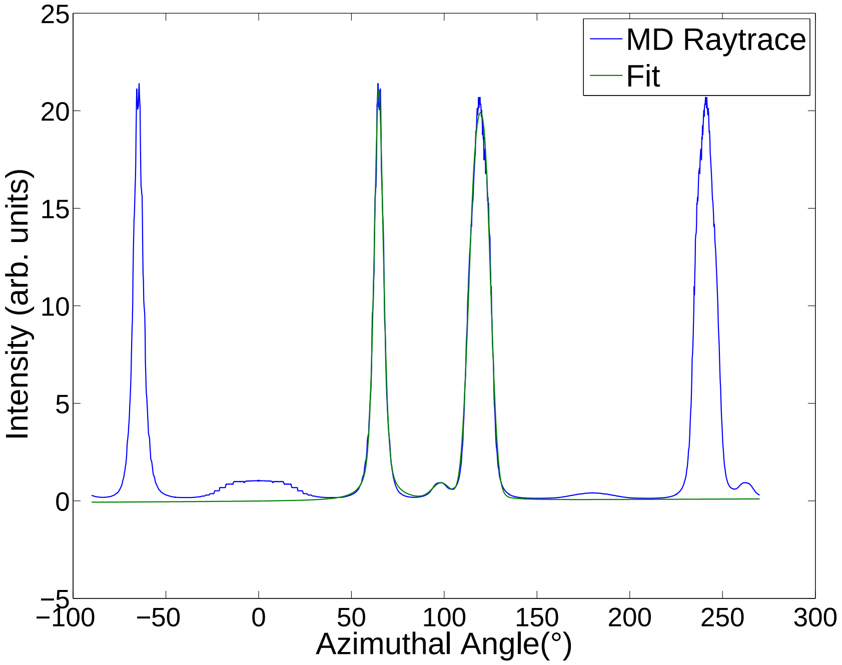

Figure 4.10: The azimuthal variation in intensity of the (110) line for the simulated diffraction pattern of the 0.6 km s^{-1} simulation.

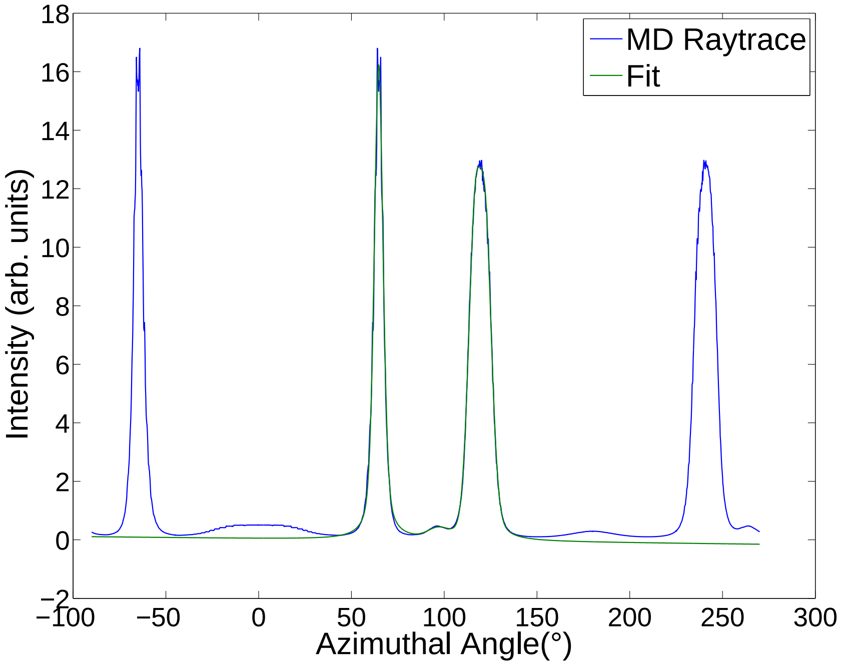

Figure 4.11: The azimuthal variation in intensity of the (110) line for the simulated diffraction pattern of the $0.62\,\mathrm{km\ s^{-1}}$ simulation.

fraction by dividing the intensities of the 95° and 65° peaks and multiplying by two. For the 0.6 km s^{-1} simulation, the PASF method gives a twin fraction of 13%, while the diffraction gives a value of 11.7%. For the 0.62 km s^{-1} simulation, the PASF method gives a twin fraction of 8.5%, while the diffraction gives a value of 7%. We find an excellent agreement between the two methods of measuring twin fraction, with the diffraction method slightly underestimating the twin fraction by between 10-20%.

4.5 Discussion

We have shown that it possible to obtain information about deformation mechanisms, be they due to phase transformations or twinning, through the use of fibre textured targets. The breaking of the symmetry of the system, by tilting the normal of the polycrystalline target with respect to the incident x-ray beam allows the encoding of such information in the azimuthal distribution of intensity in the Debye-Scherrer rings. It is worth considering, however, that the choice of initial fibre direction is important in determining what structural information can be extracted. In particular, it should be noted that for [001] fibre oriented Fe and Ta samples, these orientations do not have the lowest surface energy, and thus are not the typical orientations in which thin polycrystalline foils of these materials grow. It may thus be that some effort is required to fabricate suitable samples. This is not an issue for the case of [0001] Ti or [110] Ta, which are usually grown with these textures. This technique may also have other advantages for the study of samples subject to shock or quasi-isentropic compression. Owing to the high strain rates present in such experiments, high dislocation densities [127] or small grain sizes under phase transformation may ensue [23, 99], resulting in broad diffraction peaks that are hard to resolve simply in terms of scattering angle, and thus would not necessarily be easily amenable to study by techniques such as Rietveld refinement. However, tilting of a target and separation of diffraction peaks azimuthally offers a possible route to finding structural solutions under the extreme pressures that can be obtained via laser-ablation.

CHAPTER 5

Measuring the Timescale for Plasticity in Shocked [110] Fibre Textured Tantalum

This chapter describes an experiment using the Coherent X-ray Imaging (CXI) instrument seek to measure the timescale under which plasticity occurs in Ta.

5.1 Background

As alluded to in section 4.4.3, tantalum has multiple competing plasticity mechanisms, making it an appealing material to study plastic deformation. Relief of shear stress can occur either by a dislocation mediated response (slip) or by deformation twinning. While there has been a large amount of work dedicated to understanding plasticity in Ta, there is a striking lack of agreement between different theoretical approaches. Molecular dynamics studies of single crystal Ta compressed along the [001] direction by Higginbotham *et al.* using the EFS potential yielded twin fractions upwards of 95% [85]. Work by Tramontina and co-workers also observed massive twin nucleation above 70 GPa in single crystal simulations of [001] Ta using the Ravelo potential [128]. However, simulations performed using the Model Generalized Pseudopotential Theory (MGPT) potential developed by Lawrence Livermore National Laboratory demonstrated a homogenous nucleation threshold above 65 GPa, resulting in massive generation of dislocations, resulting in the sample deforming purely by slip [129].

Previous experiments attempting to characterise plasticity mechanisms in Ta have been limited to shock recovery experiment, where shocked material is captured and the resulting microstructure is determined by traditional crystallographic techniques. Gas gun recovery experiment performed by Florando *et al.* on single crystal Ta in a number of different observations found twin fractions of 25% by shocking along the [110] direction at 55 GPa [122]. Murr *et al.* also concluded there must be a twinning transition in their explosively driven samples to account for additional hardening of the Ta microstructure. Studies that rely on analysis of recovered samples lack time resolution and therefore cannot distinguish whether features arise due to the initial compression, subsequent reverberations or release. This has motivated the use of *in situ* diffraction to diagnose twin fraction. While white-light Laue experiments have been performed on [001] single crystal samples, to date they have not achieved the required signal to noise to distinguish between a purely slip mediated response and a combination of slip and twinning [28, 27]. Thus obtaining high quality diffraction data from a 4th generation source, such as LCLS is highly desirable. The white-light

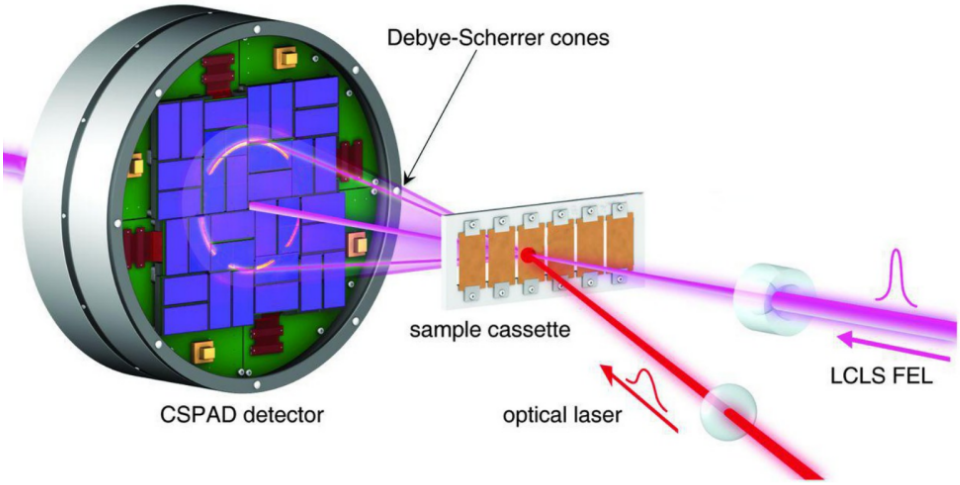

Figure 5.1: The experimental setup at CXI. From Milathianaki *et al*, *Science* **342**, 220 (2013) [1]. Reprinted with permission from AAAS.

Laue experiments have been able to observe changes in lattice aspect ratio over time, and therefore measure the plastic relaxation timescale at low pressure. However, above 50 GPa they do not have sufficient temporal resolution to resolve the relaxation, which is predicted to take place on picosecond timescales [129]. The use of femtosecond diffraction at LCLS has been successfully used to measure a relaxation time in of 60 ps in polycrystalline copper by Milathianaki *et al* [1] at the CXI end station. This experiment was performed in the Hull geometry and exploited the narrow [111] fibre texture of the Cu samples by tuning the photon energy of the XFEL beam such that the $(1\bar{1}1)$ planes met the Bragg condition, resulting in a dramatic increase in signal to noise. However, in the experiment described below we use a tilted target geometry, for the reasons outlined in chapters 3 and 4.

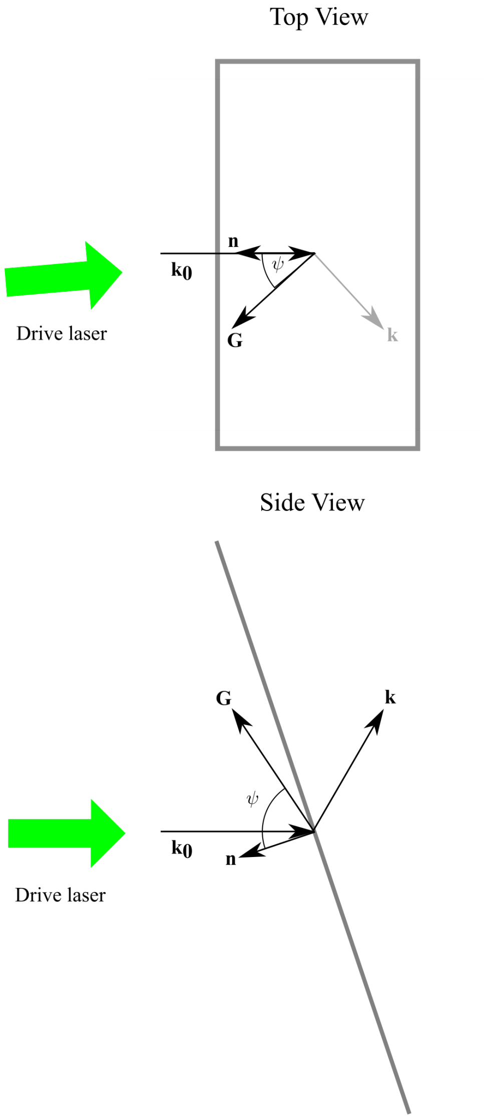

Figure 5.2: A schematic showing the top and side view of the CXI experiment.

5.2 Experimental Details

The experiment was performed at the CXI instrument at LCLS. A compression wave was launched into the Ta samples via direct ablation of the surface by a Gaussian 260 μm ($1/e^2$ diameter) focus using a 800 nm, 20 mJ, $\sim$ 170 ps (full width half maximum) Ti:sapphire laser system. The 1 μm polycrystalline Ta samples have a [110] fibre texture, with a $\sim$ 3 degrees texture width and were created by vapour deposition of Ta onto a 100 μm Si substrate. The target is interrogated by the LCLS beam, consisting of 9.4 keV x-rays pulses ($\Delta E/E = 0.2\,\%$ to $0.5\,\%$) of 50 fs duration and an average of 10^{12} photons per pulse focussed to a 30 μm diameter spot. The diffraction images were captured using an in-vacuum 2.3-megapixel array detector, the Cornell-SLAC hybrid Pixel Array Detector (CSPAD) [130] in a transmission geometry. The target normal was tilted by 18.6° about the y-axis, resulting in a symmetry breaking described in the previous two chapters (note that this tilt is about a different axis than in the previous two chapters, resulting in a top-bottom asymmetry in the data). As a result of this tilt, the diffraction data of the uncompressed crystal shows two sets of arcs. These can be characterised ψ, the angle between the diffracting G-vector and the sample normal. The two arcs at the top of the detector have $\psi = 90°$ and are only sensitive to transverse strain, while the arcs in the lower half have $\psi = 60°$ and are sensitive to both normal and transverse strains. The delay between the pump and probe beams were changed in 10 ps increments, with three diffraction images being taken for each delay time.

In Figure 5.3 we show the diffraction patterns at three different timesteps. Initially, we see the lower set of arcs move out to a large Bragg angle and move towards the centre of the detector, while the upper arcs on the detector

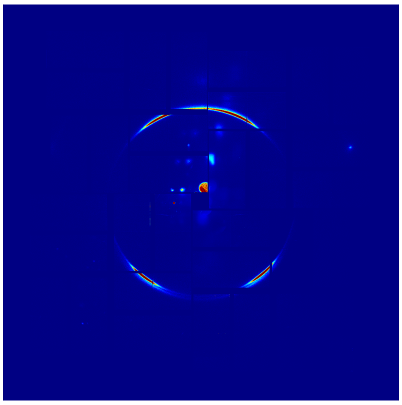

50 ps

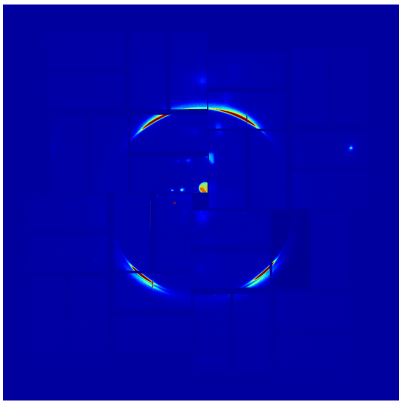

100 ps

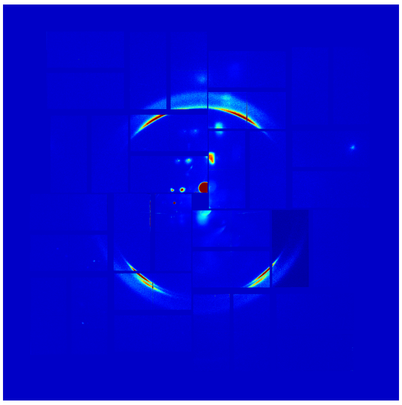

150 ps

Figure 5.3: Diffraction images captured with 50, 100 and 150 ps delay. Between 50 ps and 100 ps we see mostly elastic deformation, while between 100 ps and 150 ps we see the sample plastically relax.

do not move. Note that the diffraction pattern is symmetric about the vertical axis. The path of the incoming drive beam makes a slight angle to the sample normal and we might expect this to break the symmetry. However, at the laser intensities used in this experiment, the surface of the sample is heated via inverse bremsstrahlung and will form an expanding plasma that drives a shock perpendicular to the sample surface. Since the setup is symmetric, we can expect the diffraction pattern to be symmetric also, as shown in Figure 2.19.

As mentioned in chapter 4, the width of the diffraction arcs can be related to the textured width of the sample. Figure 5.4 shows the diffraction warped into $\theta - \phi$ space. For a given θ_B and ϕ, the angle ψ between direction of diffracting reciprocal vector and sample normal, will be given by–

$$\hat{\mathbf{G}} = \begin{pmatrix} \sin\left(\frac{\pi}{2} + \theta_B\right)\cos\phi \\ \sin\left(\frac{\pi}{2} + \theta_B\right)\sin\phi \\ \cos\left(\frac{\pi}{2} + \theta_B\right) \end{pmatrix}, \tag{5.1}$$

$$\hat{\mathbf{n}} = \begin{pmatrix} 0 \\ -\sin\chi \\ -\cos\chi \end{pmatrix}, \tag{5.2}$$

$$\psi = \cos^{-1}\left(\hat{\mathbf{G}} \cdot \hat{\mathbf{n}}\right), \tag{5.3}$$

where $\hat{\mathbf{n}}$ is the sample normal and and χ is tilt angle of the sample. Therefore for a given θ_B we can create a lineout of intensity as a function of ψ, where the width of the peaks will be the texture width of the sample. Figure 5.5 shows lineouts for both the ambient peak of 0 ps data as well as the compressed plastic peak of the 160 ps data fitted to pseudo-Voigt profiles. For the ambient data, both the $\psi = 60°$ and the $\psi = 90°$ arcs are found to

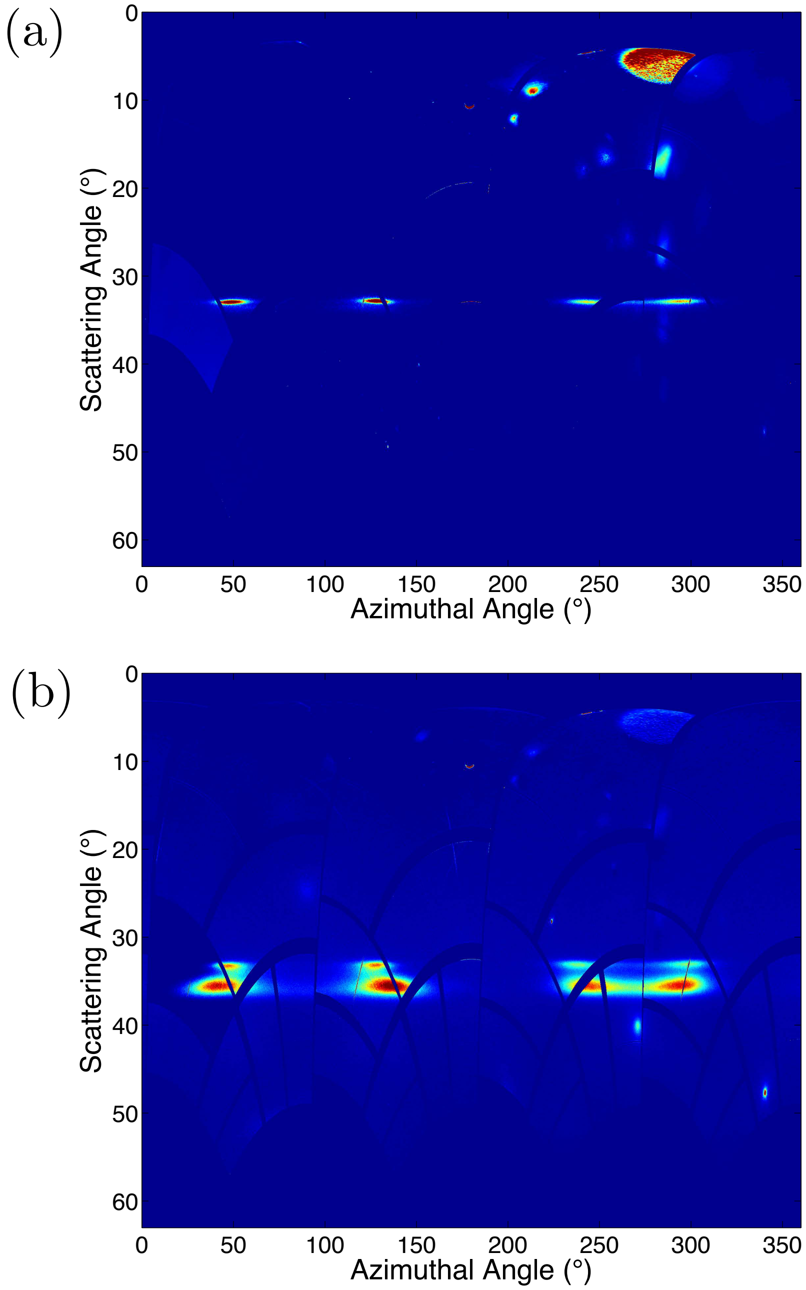

Figure 5.4: Diffraction patterns warped into $\theta - \phi$ space. Figure (a) shows that pattern as the laser turns on (0 ps), while Figure (b) shows the pattern after 160 ps.

give a full-width half-maximum texture width of 2.6°. However the $\psi = 60^\circ$ arcs from the compressed sample was found to have a width of 7.6°, while the width of the $\psi = 90^\circ$ arcs are only 4.0°. We expect the favoured $\{112\}\langle 111\rangle$ slip system to result in rotation about the $[1\bar{1}0]$ direction, resulting in a splitting of the $\psi = 60^\circ$ arcs. However, given the limited number of arcs in the diffraction pattern and the fact that any splitting of the $\psi = 60^\circ$ arcs is not large enough to resolve two peaks, we cannot be certain that slip is occurring via the $\{112\}\langle 111\rangle$ system.

If the sample twins on the (112) plane, this should result in new (110) and (002) arcs appearing at at $\psi = 70.5^\circ$ and $\psi = 73.2^\circ$, which we do not observe, and hence conclude that the sample deforms purely by slip. After 80 ps the position of $\psi = 60^\circ$ line gives a strain of 2.3%. By putting this value into equation 3.24 and assuming the transverse strain is zero, we find an elastic strain of 9.5%. This is slightly lower than the 12% elastic strain found in MD simulation using the Ravelo potential [63], however we would expect to find a lower value due to the lower strain rate of this experiment.

To analyse the data, a Lagrangian elasticity code developed by Wark, Higginbotham and coworkers [131] is used. An overview of how the code works is provided in appendix B with improvements made by Stubley [132] in his work regarding phase transitions in Si modified for the purposes of modelling plasticity. Simulated diffractions can be generated by taking the longitudinal and transverse elastic strains and then entering them into Equation 3.5. We then multiply this pattern by a probability distribution to account for the effects of fibre texture, as outlined in section 4.2. However,

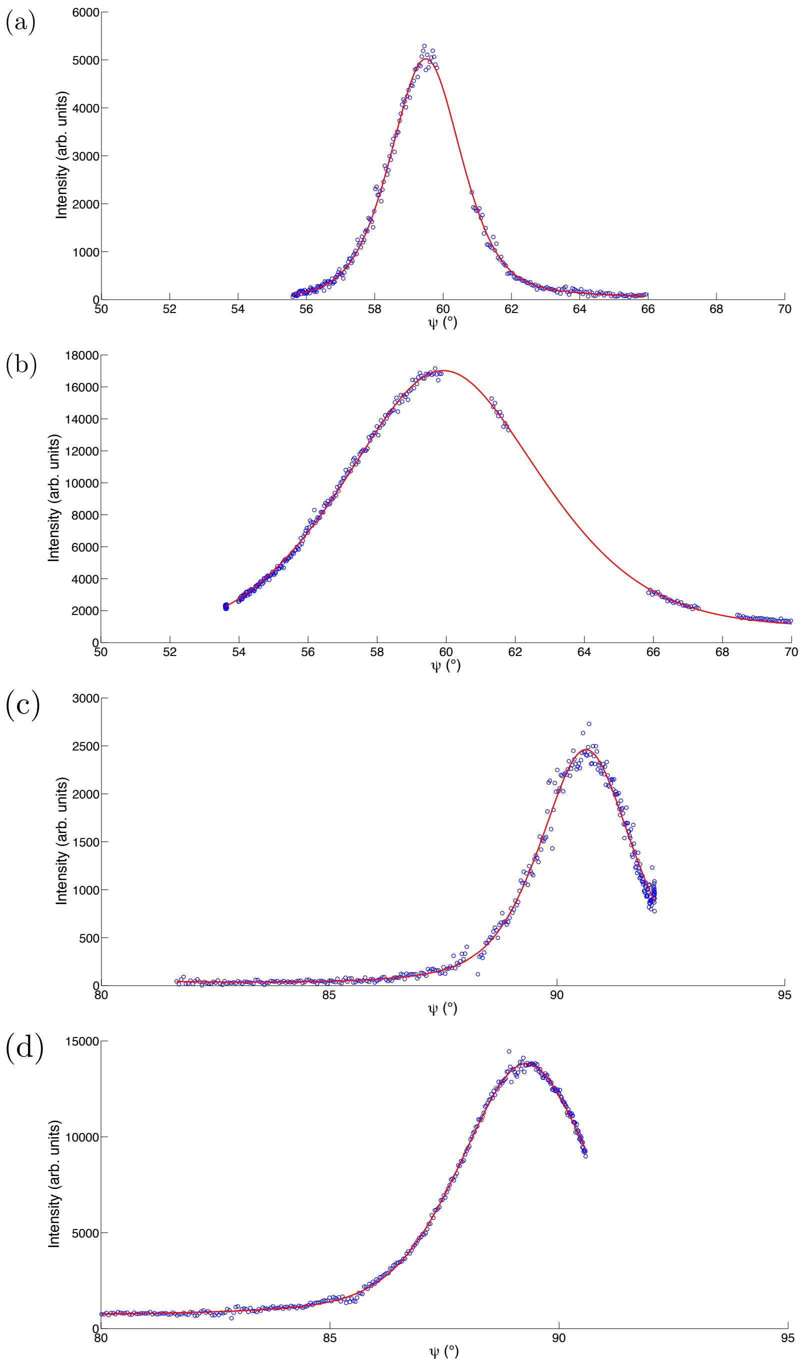

Figure 5.5: Lineout of intensity as a function of ψ. Figures (a) and (b) show lineouts from the $\psi = 60^\circ$ at 0 ps and 160 ps respectively. Figures (c) and (d) show lineouts from the $\psi = 90^\circ$ at 0 ps and 160 ps respectively. Fits to pseudo-Voigt profiles are overlaid in red.

rather than using a uniform distribution, we assume that it is Gaussian–

$$P(\mathbf{G_0}) = \frac{1}{\delta\sqrt{2\pi\ln(2)}}\exp\left[-\frac{\left(\arccos(\hat{\mathbf{v}}_\mathbf{n}\cdot\hat{\mathbf{G}}_\mathbf{0}) - \mu\right)^2}{\ln(2)\delta^2}\right]. \tag{5.4}$$

In this experiment, the picosecond laser produces a Gaussian pulse which is used to directly ablate the surface of the Ta sample. This has shown to result in a stress pulse of the form–

$$\sigma_n\left(z=0,t\right) = \frac{P_{\mathrm{peak}}t^2\exp\left(-2t/\left(t_{\mathrm{peak}}\right)\right)}{t_{\mathrm{peak}}^2\exp\left(-2\right)}, \tag{5.5}$$

$$\tag{5.6}$$

where P_{peak} is the peak pressure and t_{peak} is the rise time [131, 133]. We find for this experiment that $P_{\mathrm{peak}} = 126\,\mathrm{GPa}$ and $t_{\mathrm{peak}} = 130\,\mathrm{ps}$. The code requires this time dependent stress pulse as an input.

5.3 Analysis

To compare the data with the Lagrangian elasticity code, both the experimental and simulated diffraction data was plotted in angle space and two lineouts were taken through the (110) lines. The first lineout was formed by averaging over the ϕ range from 25° and 42°, while a second lineout was taken over the range 126° to 168°, with each lineout encompassing the $\psi = 90°$ and $\psi = 60°$ arcs respectively. A comparison between the code output and experimental data is shown in Figure 5.6 and 5.7, with a list of fitting parameters provided in Table 5.3.

Parameter	Fitted Value
HEL	30 GPa
α	$7 \times 10^{16}\,\mathrm{m}^{-2}$
v_∞	$1200\,\mathrm{ms}^{-1}$
N_0	$2 \times 10^{16}\,\mathrm{m}^{-2}$
τ_0	5 GPa
Φ	0.5 GPa
Strength	10.5 GPa

We find a good agreement between the experimental and simulated data, showing an initial elastic peak in the $\psi = 60^\circ$ lineout at $2\theta = 33.5^\circ$ followed by the formation of a broad plastic peak in both lineouts at $2\theta \sim 35.8^\circ$. We see a slight shoulder on the peaks corresponding to the elastic and uncompressed parts of the sample in both the $\psi = 60^\circ$ and $\psi = 90^\circ$ experimental data, which we do not see in the simulation. We interpret this to be a slower relaxation due to slip below the homogenous nucleation threshold, as seen by Wehrenberg below 50 GPa in [001] single crystal Ta [27]. As a result, the peak plastic strain rate may be slightly higher than suggested by the code, since we are effectively averaging over an initial slow relaxation, followed by a much faster relaxation once dislocation homogeneously nucleate. However, since we reach this threshold relatively quickly, the difference in plastic strain rate is small.

In Figure 5.8 we plot the strains experienced by a section of the sample $0.2\,\mu$m as a function of time. We find the plastic transverse strain increases to -5.2% between 80 ps and 105 ps, giving a plastic strain rate of $\sim 2 \times 10^9\mathrm{s}^{-1}$. When fitting the data, there was found to be a trade off between matching the height of the elastic peak and getting the correct speed for the plastic relaxation. Fits were also performed to match the height of

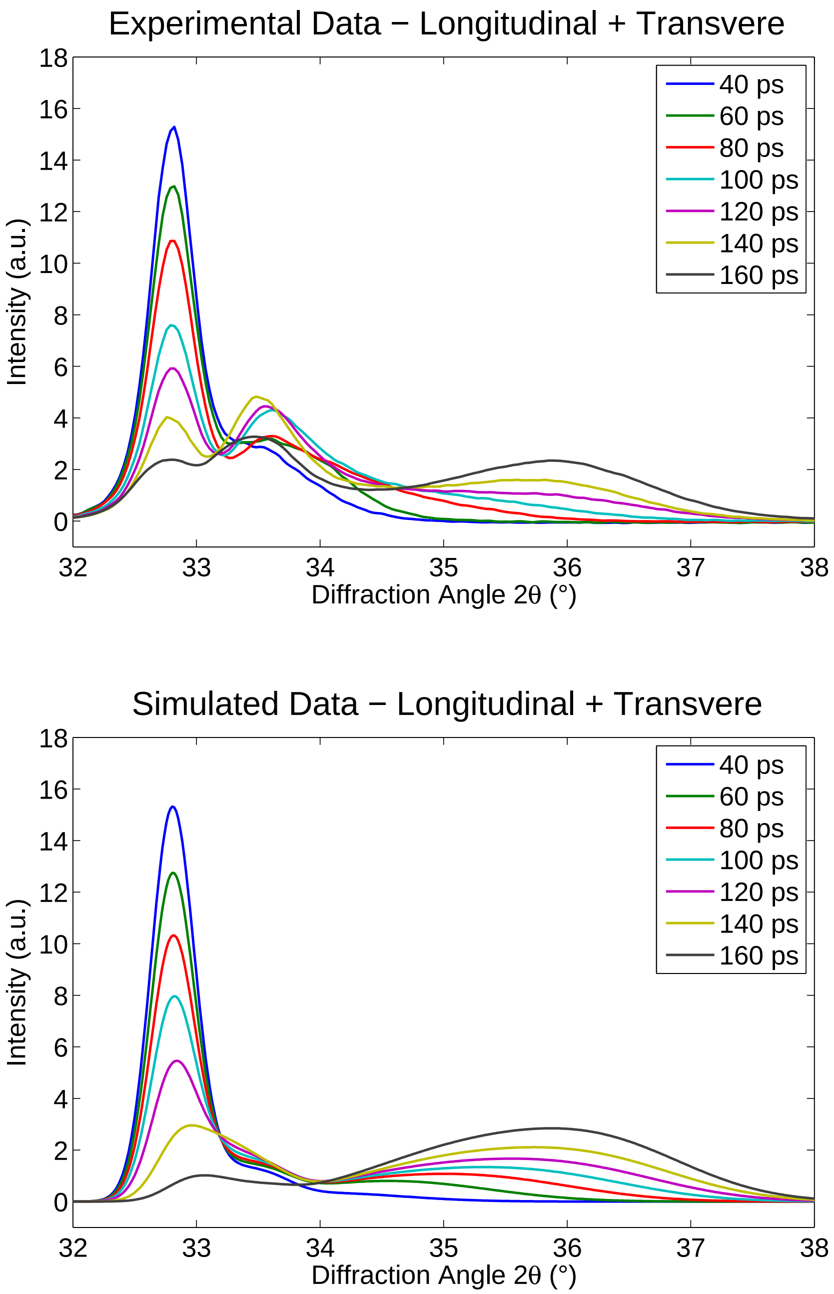

Figure 5.6: A comparison of the $\psi = 60°$ experimental data (top) with simulated data fitted using Lagrangian elasticity code (bottom).

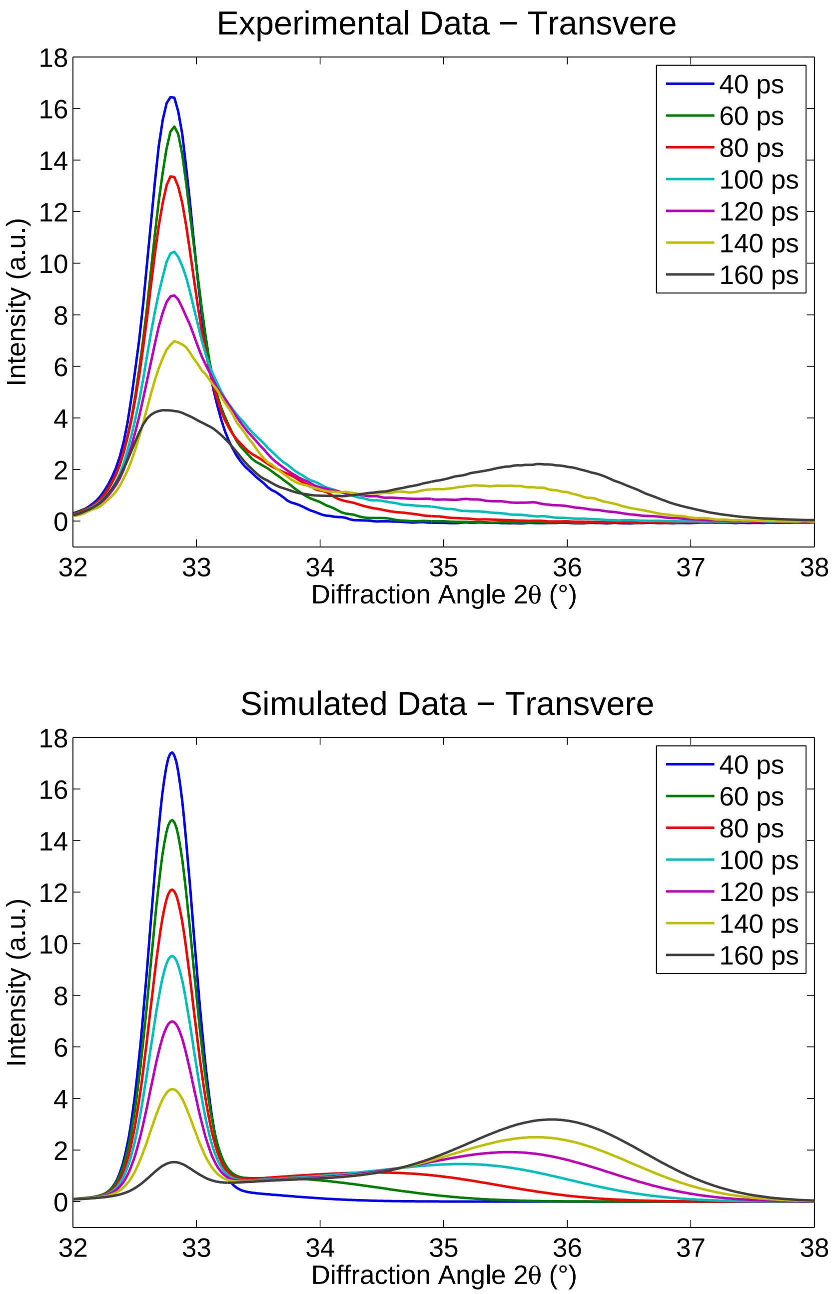

Figure 5.7: A comparison of the $\psi = 90^\circ$ experimental data (top) with simulated data fitted using Lagrangian elasticity code (bottom).

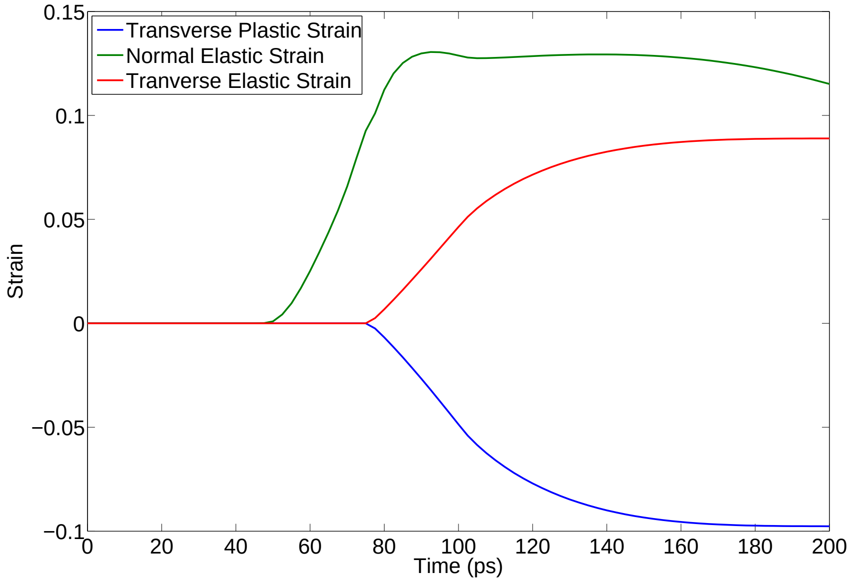

Figure 5.8: The elastic and plastic strain history at a sample depth of $0.2\,\mu$m.

the elastic peak which resulted in a significantly larger plastic strain rate, but the simulated diffraction did not match the speed at which the experimental data broadened out into the plastic peak. Thus these simulations were discarded. Given the magnitude of the Burgers vector is given by $|\mathbf{b}| = 2.86\,\text{Å}$, we can infer a dislocation density-velocity product of $7 \times 10^{18}\,\mathrm{m^{-1}s^{-1}}$, via Orowan's equation. Molecular dynamics studies have found dislocation velocities in the range $300\,\mathrm{ms^{-1}}$ to $600\,\mathrm{ms^{-1}}$, and thus we can imply a minimum dislocation density of $10^{16}\,\mathrm{m^{-2}}$. While Ta is usually thought to plastically relax much more slowly that Cu due to its limited dislocation mobility, we find that the timescale for plasticity in Ta is faster than was found in Cu by Milathianaki, albeit at a higher pressure.

5.4 Conclusions

We have measured the plastic relaxation time in polycrystalline Ta for the first time. The plastic strain rate of $2 \times 10^9\text{s}^{-1}$, which is significantly larger than found in Cu using a similar method, is significantly larger than expected from heterogeneously generated dislocations. This therefore suggests that the dislocations are either homogeneously nucleated or the multiplication rate for dislocations that are heterogeneously nucleated is significantly higher than expected.

CHAPTER 6

Experimental Investigations into the Plasticity Mechanisms of Shocked [110] Fibre Textured Tantalum

The experiment in the previous chapter used relatively thin samples and a gaussian laser pulse, resulting in an unsteady drive. To study the response from a steady shock, a second experiment was undertaken using a different setup with a nanosecond laser.

6.1 Experimental Details

The experiment was performed at the MEC end station of the LCLS. A 5-10 ns 2ω (527 nm) 16 J square pulse was used to irradiate samples and drive a planar shock. Hybrid Phase Plates (HPP) of either 150 μm or 250 μm in diameter (depending on the required pressure) were used to ensure a smooth beam profile. The targets were made by vapour deposition of Ta onto a SiO_2 substrate to form a 6 μm layer with a [110] fibre texture. This was performed at a significantly high temperature to obtain a narrow texture width while allowing the foil to be delaminated from the substrate on cooling. The resultant foils were predominantly α-Ta (bcc), although some targets contained a small amount of β-Ta (<1%). A 50 μm Kapton layer was then glued onto the target to form an ablator, to allow the pressure pulse to shock up in the plastic layer before reaching the Ta foil, whilst also shielding the Ta layer from the heat produced by the laser ablation. Two different batches of Ta targets were used during the experiment, r123 with a texture width of $\sim 2^\circ$ and r127 with a texture width of $\sim 1^\circ$. A schematic of the setup is provided in Figure 6.1. The LCLS beam (9.6 keV, 50 fs duration) was focused to a 20μm diameter spot which was centred on the focal spot of the drive laser. The x-ray beam and optical laser were timed with a delay such that the shock had travelled approximately half way through the sample when the probe pulse arrives and the resulting diffraction pattern was recorded on several CSPADs. The sample was oriented such that the probe beam makes a 35° angle with respect to the target normal. While pressures were determined by extracting the volumetric compression from diffraction and comparing them with Hugoniot data, a line VISAR was used to measure rear surface velocities to provide an independent check of these values. Figure 6.3 shows an example of a diffraction pattern taken from an uncompressed sample. The image has a log colour scale so all the relevant peaks can be easily viewed on the same plot despite there being a large variation in signal intensity. Dashed lines indicate constant 2θ values corresponding to ambient bcc Ta. The low intensity signal between these lines is from the small vol-

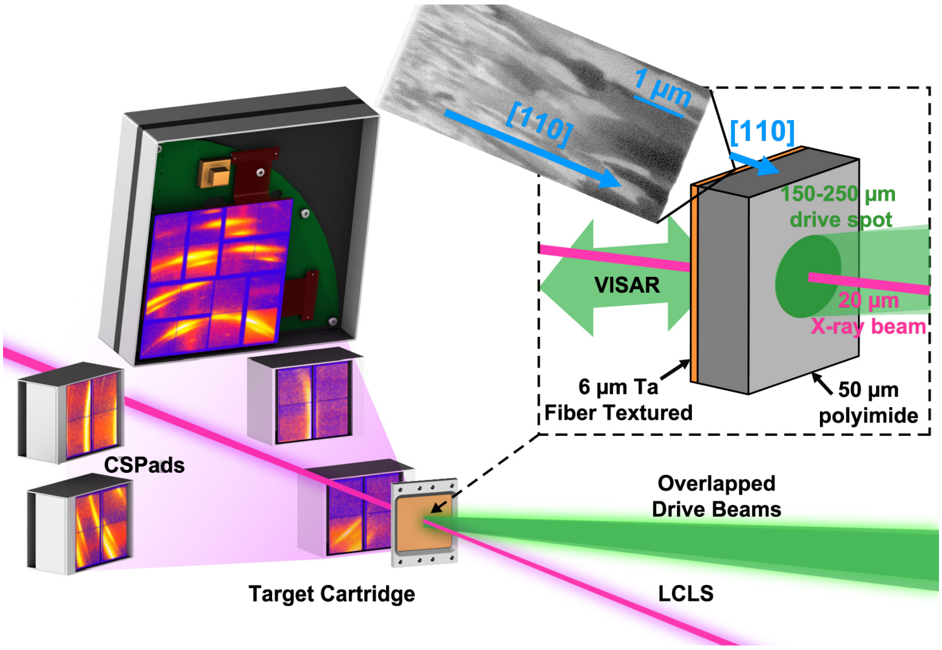

Figure 6.1: The experimental setup used at the MEC end station of LCLS. A nanosecond laser irradiates a plastic ablator driving a shock into the Ta sample. An SEM micrograph shows the columnar grains that result in the [110] fibre texture. The LCLS x-ray beam is used to interrogate the shocked Ta, and the resulting diffraction patterns are captured on an array of CSPADs.

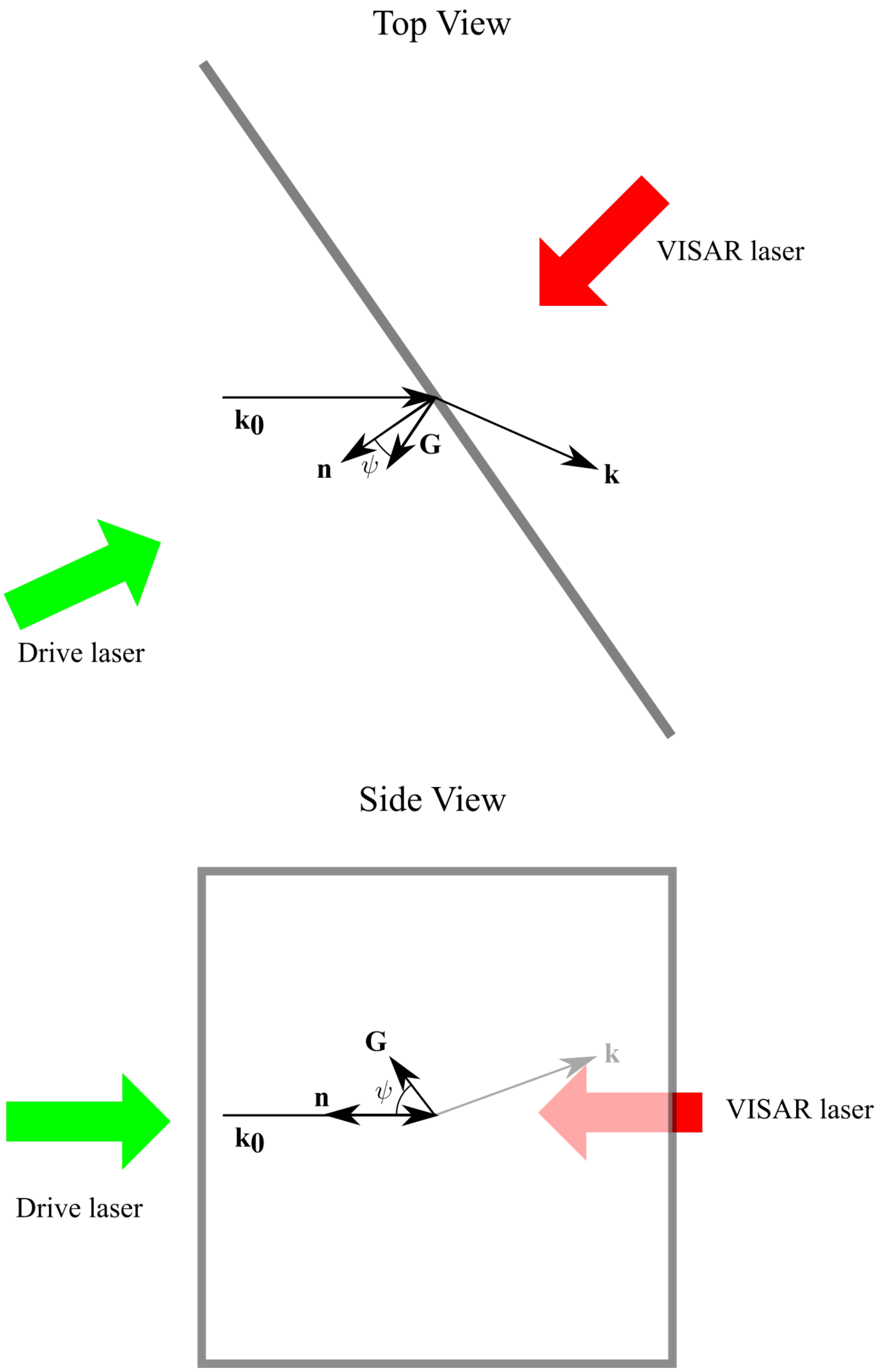

Top View

Side View

Figure 6.2: A schematic showing the top and side view of the MEC experiment.

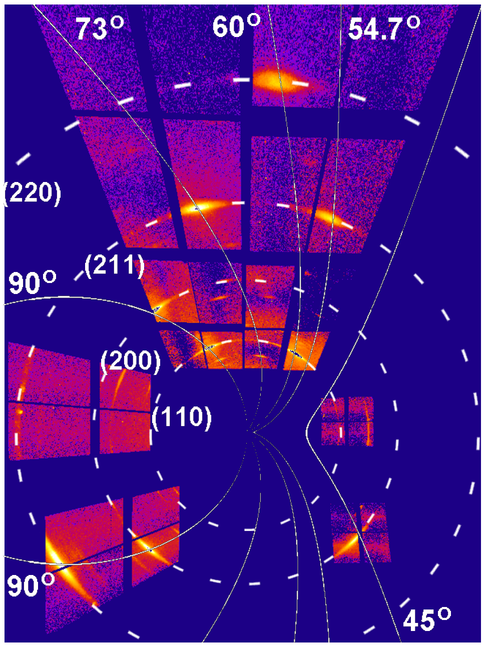

Figure 6.3: Ambient diffraction data projected onto a flat plane normal to the incoming x-ray direction.

ume fraction of β-Ta. The solid lines show constant ψ values, the predicted position of diffracted signal assuming a constant angle between the sample normal and a reciprocal lattice vector, G. In addition to the (110) arcs with ψ of 60° and 90° seen in the CXI experiment, we also see (002) arc with ψ of 90° and 45°, (112) arcs with ψ of 90°, 73.2° and 54.7° and a (220) arc with ψ of 60°. These are all consistent with the pattern expected for a [110] fibre textured bcc material.

6.2 Analysis

Diffraction images were collected at pressures from 15 GPa up to 270 GPa. Figures 6.4 and Figure 6.5 shows eight different diffraction patterns from samples at pressure from 30 GPa to 265 GPa, with lines of constant ψ over-

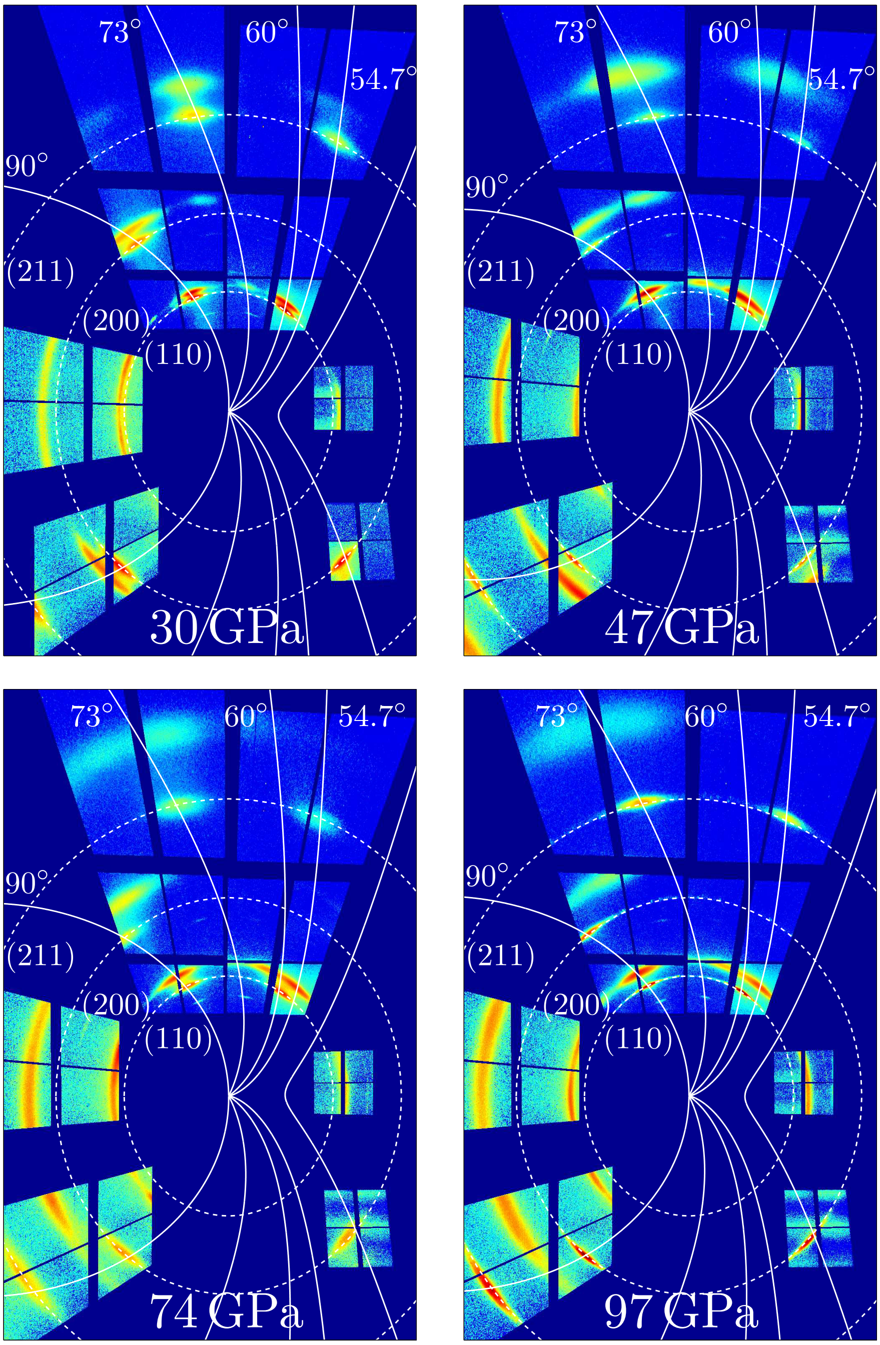

Figure 6.4: Low pressure data from the experiment projected onto a flat plane normal to the incoming x-ray direction.

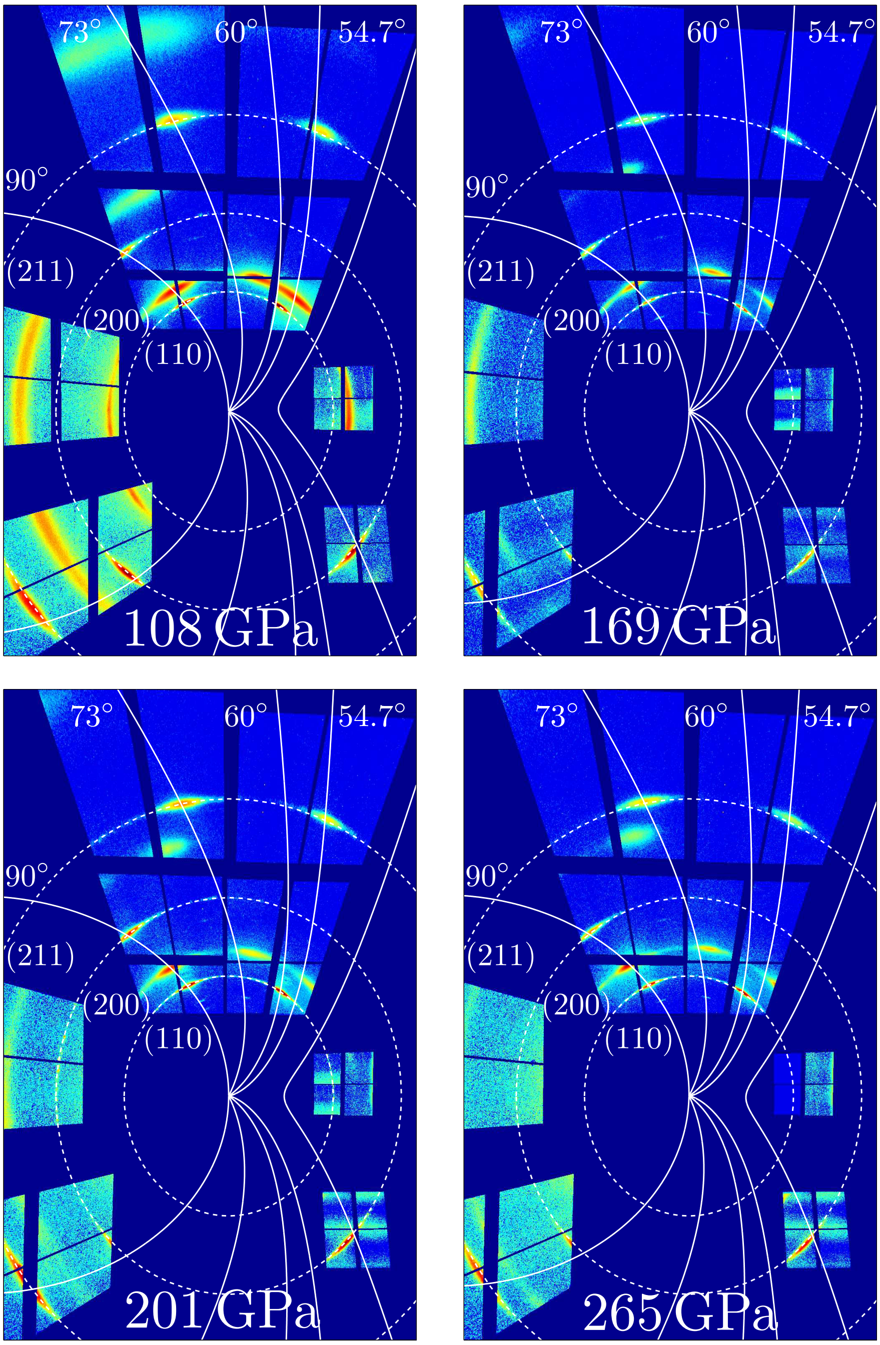

Figure 6.5: High pressure data from the experiment projected onto a flat plane normal to the incoming x-ray direction.

laid in white. Note that the positions of these lines and the arcs corresponding to diffraction from the ambient sample change slight between shots. This is because, unlike in the CXI experiment where the sample was one flat Ta sheet deposited onto a Si wafer, the Ta foil was diced to form individual targets and each of the targets were slightly misaligned to the sample mount. However, by measuring the positions of the five ambient peaks on the largest detector, the sample orientation can be fitted. The lines of constant ψ can then be drawn taking account for any misalignment.

While other recovery experiments have observed a phase transition to the hexagonal ω phase under shock compression in single crystals, we find no phase change up to 270 GPa, meaning that shear stress built up by uniaxial compression must be relieved plastically by either slip or twinning. We can characterise changes in the orientation of the lattice by measuring changes in the ψ value for each of the arcs. At 20 GPa, we initially see little change in ψ for each of the peaks, however we see the emergence of a new arcs at $\psi = 73^\circ$ and 78° for the (110) and (002) lines respectively, which correspond to the expected positions for a crystal twinned on the (112) plane with a 2.5° rotation. As pressure increases, we observe an initial broadening followed by a splitting of the $\psi = 60^\circ$ (110) arc, while the corresponding $\psi = 90^\circ$ does not split. This can be explained by a lattice rotation about the $[1\bar{1}0]$ direction, since the G-vector corresponding to the $\psi = 90^\circ$ arcs are parallel to the rotation axis and therefore unaffected, while $\psi = 60^\circ$ G-vectors will either be rotated towards or away from the sample normal, changing their ψ value either up or down and resulting in a splitting in the azimuthal position of the peaks. By fitting the azimuthal position of the peaks in term of ψ (as outlined in section 5.2), or by fitting the broadening of the $\psi = 60^\circ$ (110) for data taken below 70 GPa, we can find the lattice rotation as a

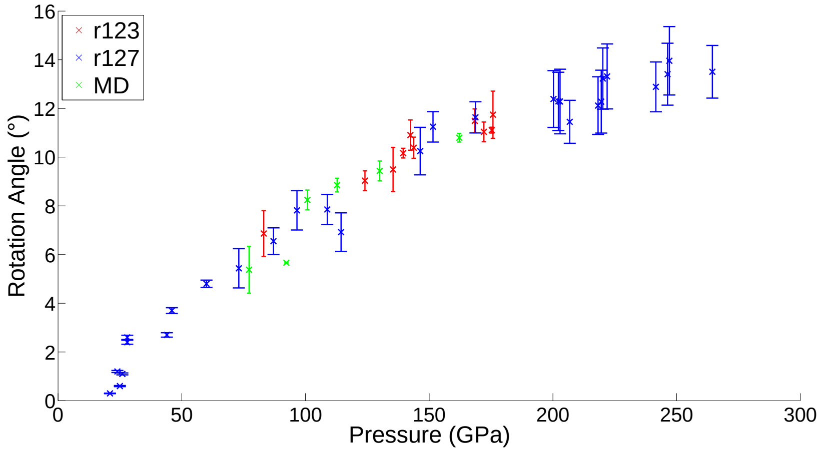

Figure 6.6: Lattice rotation angle calculated from experimental diffraction patterns compared to measured rotation in MD simulations using the Ravelo potential.

function of pressure, shown in Figure 6.6. We also show the lattice rotation observed in MD simulations using the Ravelo potential [63]. We repeated the simulations described in section 4.4.3 but vary the piston velocity to achieve a range of pressures. By taking the FT of the plastically relaxed region behind the shock front, we were able to directly extract the lattice rotation as a function of pressure. We observe very good agreement between the simulation and data up to 150 GPa, where we start to see the formation of a premelted region behind the shock front described in Ravelo's paper which limits our ability to look at higher pressures. While both twinning and slip can both cause rotation in either direction around the $[1\bar{1}0]$ axis (shown in Figure 6.7), in both the diffraction data and the MD simulations, we see that twinned and slipped untwinned regions must locally cause a rotation in the same direction. If the opposite was true, and they rotated in opposite direction, the $\psi = 60^\circ$ (110) arc would not split and if there was no correlation between the rotation directions of slip and twinning (in other

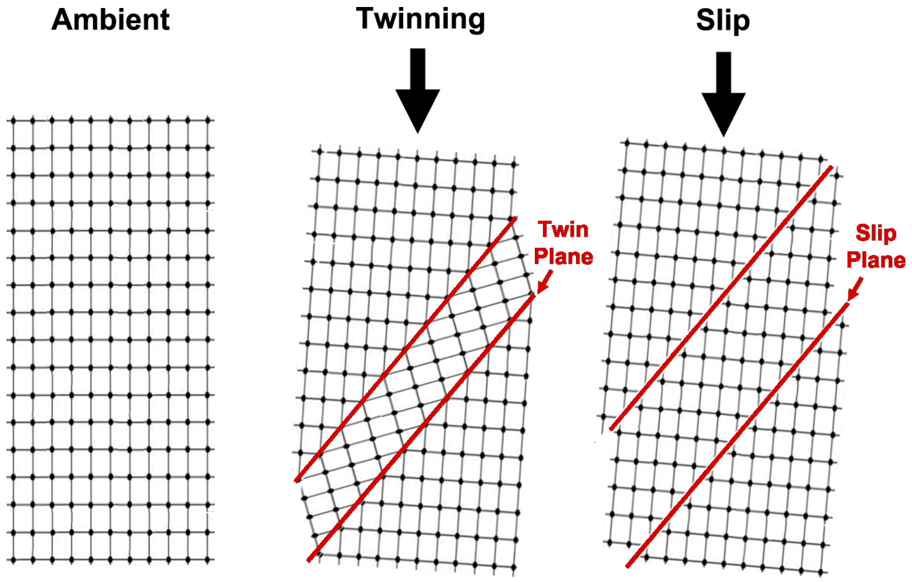

Figure 6.7: Lattice rotation can result from both twinning and slip.

words areas of rotation in the same and opposite directions), there would be more (110) peaks than we observe. If we consider the Schmid factor for (112) type planes (which is the same for both slip and twinning), we see why this is the case as if the lattice starts to rotate, the Schmid factor now favours the slip or twin system that will increase the rotation. 6.6.

We can also measure the twin fraction of the sample by comparing the ratios of intensities of different arcs. Material in both the twinned and untwinned orientation will contribute equally to the $\psi = 90°$ (110) reflection while only twinned material will contribute to the intensity of the new arc. Additionally, we must consider that there are twice as many G-vectors that can contribute to the $\psi = 90°$ peak in both twinned and untwinned case than contributing to the new peak from the twinned material, so to find the twin fraction we must take the ratio of the total intensity contained in the new arc with the intensity of the $\psi = 90°$ and multiply by two. This assumes that

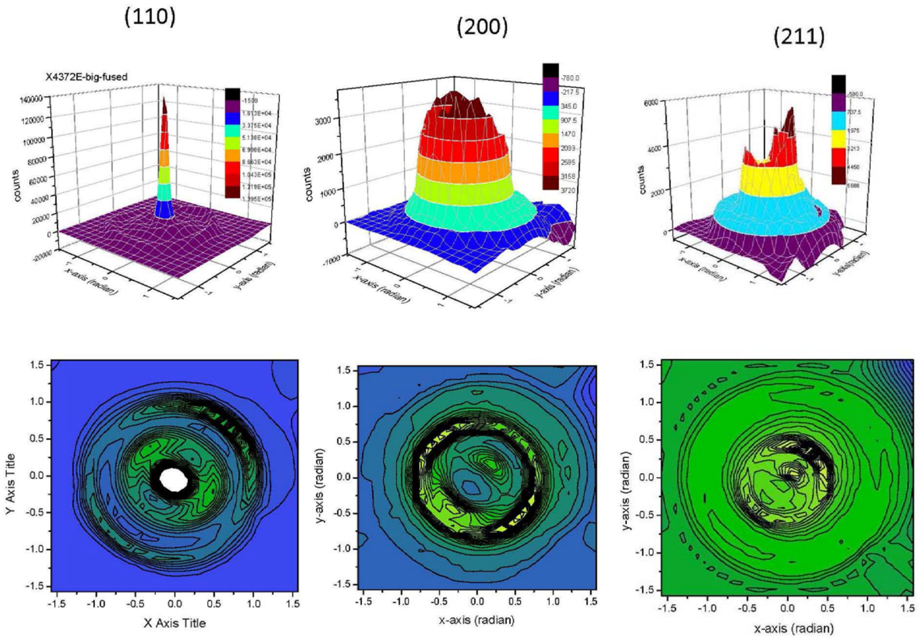

Figure 6.8: Pole plots showing the unequal azimuthal distribution of grains in the Ta samples.

there is a completely random azimuthal distribution of grains. However, pole plots of the ambient samples revealed this not to be the case, shown in Figure 6.8. As a result, our twin fraction measurement will be inherently noisy due to the effects this distribution, since it is not consistent between targets. We can significantly reduce this noise by using the diffraction patterns from the ambient sample taken before the driven shot to correct the data. The grains that diffract into the new twin arc have a similar azimuthal orientation to the grains that diffract into the (112) $\psi = 54.7°$ arc, while the grains that diffract into the ambient and compressed (110) $\psi = 90°$ arcs are also similar. Thus it is possible to use the ratio of these two ambient peaks (accounting for intensity reduction due to the Debye-Waller effect) to correct for the effect of the azimuthal asymmetry. Figure 6.9 shows the corrected twin fraction as a function of pressure. We observe the onset of twinning at 26.5 GPa and

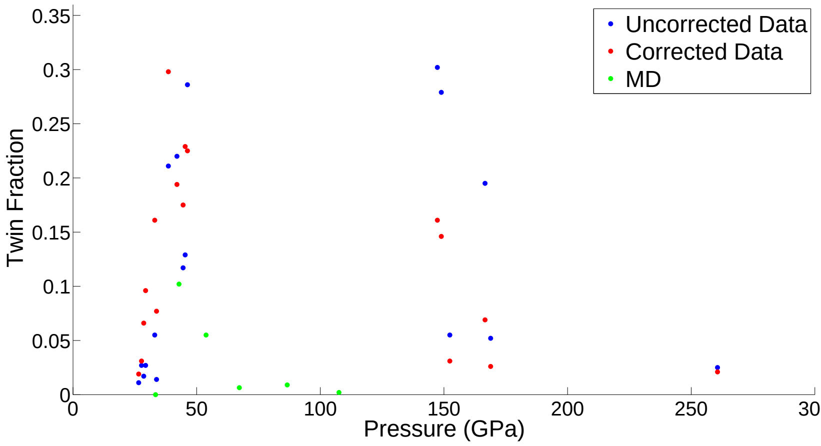

Figure 6.9: Uncorrected and corrected twin fraction data as a function of pressure.

find a roughly linear increase in twin fraction up to 23% at 45 GPa, which is close to the 25% twin fraction seen by Florando in recovery experiments at 55 GPa [122]. However, beyond this pressure, the (110) twin spot moves into a gap between the detectors. At pressures above 90 GPa, we find a new (110) twin arc at approximately $\psi = 100°$. The twin fraction can be calculated in the same way as mentioned before, but this time, the ambient $\psi = 90°$ (002) peak is used to correct for azimuthal distribution. However, since this peak is not as close a match in azimuthal orientation, there is a larger error on these measurements. The larger texture width of the r123 targets made it very difficult to measure the intensity of the twin spot, and thus the data presented here is only for the r127 targets. We also plot the twin fraction found from the simulations mentioned above. We apply the PASF code [85] on the plastically relaxed region behind the shock front for each simulation to identify atoms in the untwinned and twinned orientations and use this to calculate a twin fraction, shown in Figure 6.9. In both cases we see an increase in twin fraction up to a maximum at 45 GPa, followed by a drop off. However, the molecular dynamics simulations give a significantly lower peak twin fraction and has a much quicker drop off. Since we are performing a single crystal simulation, this is not completely applicable to the fibre texture samples used in the experiment. Thus it is possible that we may get a closer agreement with the data by performing a polycrystalline simulation with a fibre texture.

The amount of lattice rotation can be used to calculate the total plastic shear strain relieved (see appendix C)–

$$\gamma^p\left(rotation\right) = \frac{\cos\phi}{\cos\phi_0} - \frac{\cos\phi_0}{\cos\phi} \tag{6.1}$$

Furthermore, we can compare this to the value expected for hydrostatic compression along the Hugoniot (see appendix C)–

$$\gamma^p = \left(\frac{V_0}{V}\right)^{2/3} - \left(\frac{V}{V_0}\right)^{2/3} \tag{6.2}$$

We can also calculate the shear stress relieved for a twin fraction f, shown in Figure 6.10. Note that slip and twinning will both relieve the same amount of plastic shear strain for a given rotation angle. At the lowest pressures, the amount of plastic shear strain is significantly less than expected for hydrostatic compression on the Hugoniot. Molecular dynamics simulations suggest we should observe a purely elastic response at these pressures. However this would result in a significant anisotropy in elastic strains, that should be detectable in the diffraction signal. In fact, we find no elastic shear strain to within the detector resolution ($< 6\%$). Thus, we hypothesise that the lack of initial rotation is due to existing defects in the crystal that could activate a number of slip planes that do not necessarily have the highest Schmid factor. At low pressures, this could be sufficient to relieve the shear

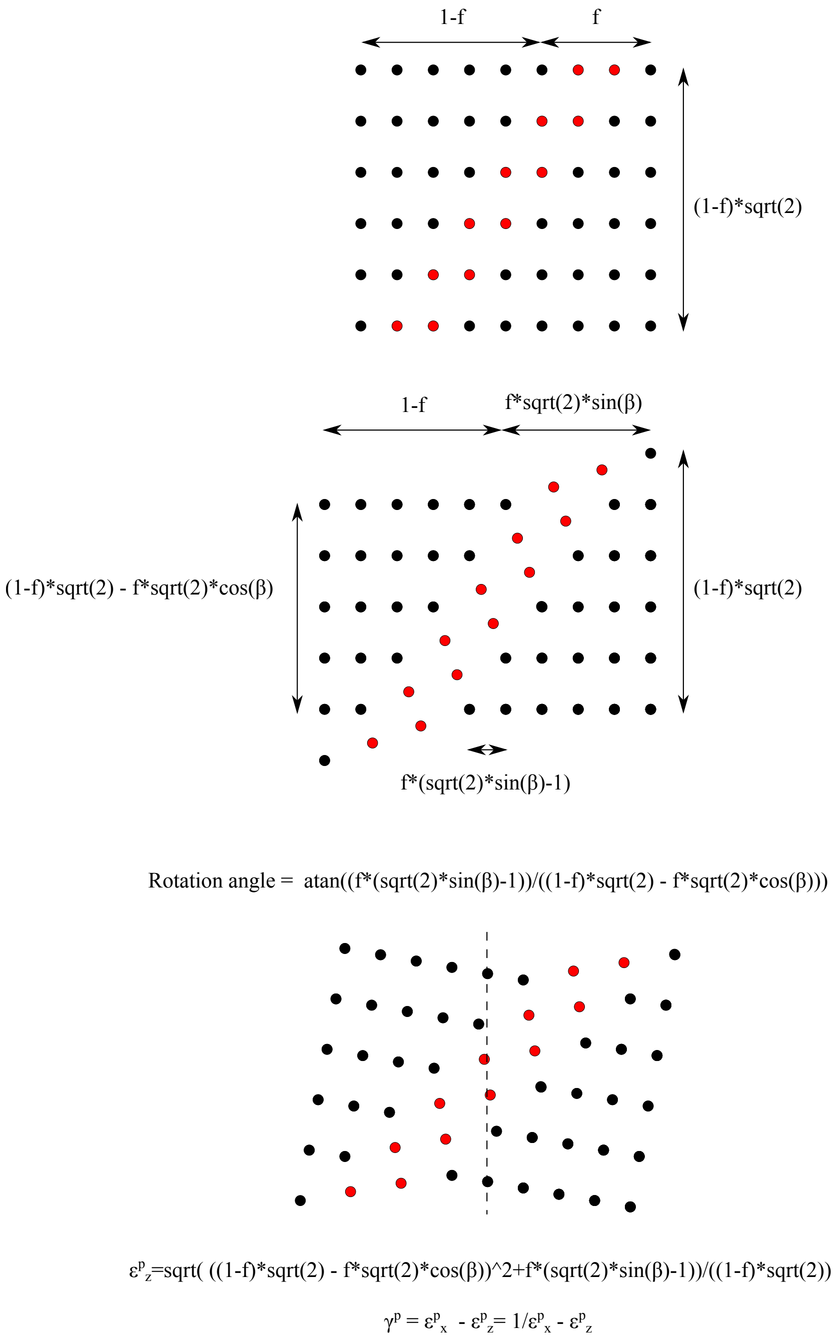

Figure 6.10: A diagram demonstrating how a Ta [110] crystallite will twin to relieve shear stress by a series of slips. β is the angle between the [110] and [114] directions and f is the twin fraction.

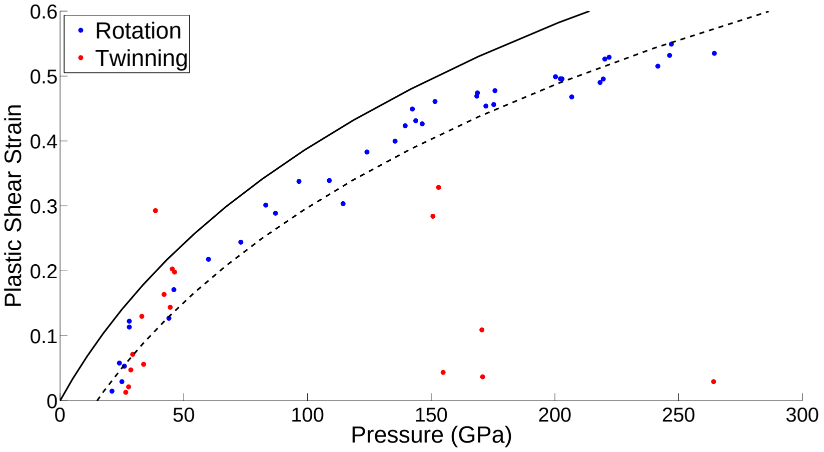

Figure 6.11: A comparison of the total plastic shear strain relieved in the sample (calculated from the lattice rotation) with the shear strain relieved by twinning. The solid line shows the expected plastic shear strain relieved if the compression is hydrostatic, while the dotted line assumes that rotation due to slip and twinning is inhibited until 15 GPa.

stress built up by shock compression. Since multiple slip systems are relieving small amounts of shear stress, we postulate that this will not result in a large net rotation, thus explaining the lack of rotation at small pressures. Further analysis of the microstructure of the initial samples is required to find whether the initial defect density is high enough to make this theory plausible. At higher pressures, the Hugoniot equivalent plastic shear strain and total plastic shear strain measured from rotation diverge. However, if we change the value of V_0 in Equation 6.2 so that plasticity only starts at $0.93V_0$ (equivalent to 15 GPa), we are able to obtain good agreement over the whole pressure range of the experiment.

The plastic shear strain relieved by twinning closely follows the total amount measured from the rotation in the range 20-45 GPa, suggesting initially all shear stress is relieved by twinning. This close agreement is an indication that the twinning occurs by the slip mechanism shown in Figure

6.10, rather than the shuffle mechanism proposed by Higginbotham *et al.* [85] which does not result in a net rotation of the lattice. If the rotation of the lattice was due to another mechanism, such as slip, this would mean that the total plastic shear strain relieved would be larger than would exceed the Hugoniot plastic shear strain, and therefore the should be larger transverse elastic strain than the longitudinal elastic strain, which we do not observe.

At higher pressures, we see a large difference between the plastic shear strain inferred from twin fraction and lattice rotation, shown in Figure 6.11. We interpret this difference as relaxation due to slip. We therefore find that slip is the dominant mechanism at 150 GPa and above. This provides further evidence that there should be a transition to homogenous nucleation dislocations somewhere between 50 and 150 GPa.

6.3 Conclusions

We have also demonstrated the first *in situ* measurement of twin fraction in a shocked bcc material. While the two experiments disagree about the importance of twinning in Ta plasticity, this is not necessarily surprising, given the significant differences in their setups. While a nanosecond laser is used in the MEC experiment, the fact that the shock steepens up in a CH ablator means that the strain rate expected from the Sweagle-Gradey relation is actually higher than in the CXI experiment at relatively low pressures. This suggests that twin fraction could strongly depend on strain rate, and prompts further investigation.

CHAPTER 7

Conclusions and Further Work

7.1 Summary

In chapter 3 an expression is derived for the form of Debye-Scherrer diffraction from polycrystalline materials deformed by an arbitrary deformation gradient. A number of simplified expressions for common geometries used in shock compression experiments are given, as well as the general formula. This prediction agrees with ray tracing from computationally generated polycrystals and is also shown to agree with existing theory used to measure strain anisotropy in the small strain limit. However, it is shown that for large shear strain, a more accurate form of analysis can alleviate errors due to incomplete sampling of ψ, and that this form is applicable for any strain state within the Voigt limit. By making a small modification to existing analysis this source of error can be removed without adding complexity.

By checking the original orientation of the grain before compression, it is possible to predict the effect that texture will have on the diffraction pattern. Using this technique, the azimuthal dependence of the intensity around the Debye-Scherrer ring can be used to yield information about lattice orientation. For a fibre textured material, it is possible to obtain orientation relations that relate the two structures involved in a phase transition, and this is demonstrated using the examples of Fe and Ti. This technique can also be used to identify large rotations associated with twinning and predicted diffraction for twinning in [001] and [110] Ta is provided, with comparisons to MD simulations.

Chapter 5 describes two LCLS experiments using the technique outlined in earlier chapters to investigate plasticity in Ta. In the first experiment at the CXI end station, we measure the plastic relaxation time in polycrystalline Ta for the first time. At 40 ps this is faster than a similar measurement made in Cu, albeit it at a high pressure. The second experiment at the MEC end station provides the first *in situ* diffraction measurement of twin fraction in a shock compressed metal. We also measure an overall rotation of both the twinned and untwinned crystal which can be related to shear stress relieved by plasticity. These two measurements demonstrate that in the range 20-50 GPa, twinning is the dominant mechanism of plastic deformation, while above 150 GPa, slip is more important.

7.2 Further work

The differences observed in the two LCLS experiments naturally lend themselves to further enquiry. The lack of agreement on twin fraction suggests that there may be a strong dependence on strain rate, since the two experiments used very different drives. Additionally, while this work has assumed that strains in both transverse directions are the same, there are some indications that this might not be the case. For the case of compression along the [110] axis, it is easy to plastically relieve shear strain in the [002] direction by shearing along {112} type planes (either by slip or twinning), but shear strain is not relieved in the $[1\bar{1}0]$ direction. Thus to elastically compress grains along $[1\bar{1}0]$ requires for them to be compressed by the expansion of neighbouring crystallites in a different azimuthal orientation. Thus any difference between the strains in the two transverse directions provides information of where the sample lies between the Voigt and Reuss limits. While we have applied this technique to the problem of bcc materials, we would like to apply this to other crystal structures. Work by Suggit *et al.* has already demonstrated lattice rotation in Cu single crystals in response to shock compression [26], and the techniques outlined here would allow us to extended this work to polycrystalline samples at higher pressure.

The fibre texture technique may have other advantages for the study of samples subject to shock or quasi-isentropic compression. Given the nature of laser compression, high strain rates will often result in large dislocation densities or small grain sizes under phase transformation. This results in broad diffraction peaks which limit the ability of techniques such as Rietveld refinement to find structural solutions to high pressure phases. However, using this tilted target technique it may be possible to separate diffraction peaks azimuthally, offering a route to identification of complex phases at high pressure. This is important since new facilities opening up such as the Dynamic Compression Sector (DCS) at the APS synchrotron and the HIBEF facility at XFEL in Hamburg offering much high pressures than those achievable at LCLS.

APPENDIX A

Reciprocal space deformation

Let us assume a deformation gradient, $\mathbf{F}$, is applied in real space. This deformation gradient is defined such that the position, $\mathbf{u}$, of an element in the undeformed system, is related to its position in the deformed system, $\mathbf{U}$, by $\mathbf{U} = \mathbf{F}\mathbf{u}$. In general this deformation gradient will consist of 9 independent components -

$$\mathbf{F} = \begin{pmatrix} a & b & c \\ d & e & f \\ g & h & i \end{pmatrix}. \tag{A.1}$$

One can apply this to three unit vectors initially aligned with the cartesian axes in the undeformed system to fully characterise the deformation -

$$\mathbf{a} = \begin{pmatrix} a \\ d \\ g \end{pmatrix}, \quad \mathbf{b} = \begin{pmatrix} b \\ e \\ h \end{pmatrix}, \quad \mathbf{c} = \begin{pmatrix} c \\ f \\ i \end{pmatrix}. \tag{A.2}$$

Assuming that these vectors span a lattice, one can define the equivalent reciprocal lattice vectors as -

$$\mathbf{a}^* = \frac{2\pi}{V_D} \begin{pmatrix} ei - hf \\ hc - bi \\ bf - ce \end{pmatrix}, \tag{A.3}$$

$$\mathbf{b}^* = \frac{2\pi}{V_D} \begin{pmatrix} fg - id \\ ia - cg \\ cd - af \end{pmatrix}, \tag{A.4}$$

$$\mathbf{c}^* = \frac{2\pi}{V_D} \begin{pmatrix} dh - eg \\ bg - ah \\ ae - db \end{pmatrix}, \tag{A.5}$$

where $V_D = a\,(ei - hf) + d\,(hc - bi) + g\,(bf - ce)$ is the volume of an initially cubic unit cell in the deformed system. One can use these reciprocal lattice vectors to define a deformation gradient, $\mathcal{F}$, for reciprocal space -

$$\mathcal{F} = \frac{1}{\mathrm{V_D}} \begin{pmatrix} ei - hf & fg - id & dh - eg \\ hc - bi & ia - cg & bg - ah \\ bf - ce & cd - af & ae - db \end{pmatrix} = \left(\mathbf{F}^{\mathrm{T}}\right)^{-1}, \tag{A.6}$$

which is seen to be equivalent to the inverse transpose of the real space deformation gradient, **F**.

APPENDIX B

Lagrangian Elasticity Code

Conservation of mass and momentum leads to equations relating stress, σ_n, and total strain, ϵ_n^T, along the normal direction, and particle velocity, u–

$$\rho_0 \left(\frac{\partial u}{\partial t} \right) + \left(\frac{\partial \sigma_n}{\partial z} \right) = 0, \tag{B.1}$$

$$\left(\frac{\partial \epsilon_n}{\partial t} \right) + \left(\frac{\partial u}{\partial z} \right) = 0. \tag{B.2}$$

We can relate small changes in strain to changes in stress via elastic constants. This can be found by obtaining the stiffness tensor for a [110] oriented Ta single crystal as function of longitudinal and transverse strain, using a modified version of the elastic constants code found in LAMMPS [59] with the Ravelo Ta potential [63]. To get the stiffness tensor, we find the tensor rotated about the fibre axis by angle ξ [134], and then assume that the grains are randomly distributed in ξ, such that $\langle\cos\xi\rangle = \langle\sin\xi\rangle = 0$, $\left\langle\cos^2\xi\right\rangle = \left\langle\sin^2\xi\right\rangle = 1/2$ and $\left\langle\cos^4\xi\right\rangle = \left\langle\sin^4\xi\right\rangle = 3/8$. This results in an average stiffness tensor for the fibre textured sample of the form–

$$\begin{pmatrix} \Delta\sigma_t \\ \Delta\sigma_t \\ \Delta\sigma_n \\ 0 \\ 0 \\ 0 \end{pmatrix} = \begin{pmatrix} C_{11} & C_{12} & C_{13} & 0 & 0 & 0 \\ C_{12} & C_{11} & C_{13} & 0 & 0 & 0 \\ C_{11} & C_{13} & C_{33} & 0 & 0 & 0 \\ 0 & 0 & 0 & C_{44} & 0 & 0 \\ 0 & 0 & 0 & 0 & C_{44} & 0 \\ 0 & 0 & 0 & 0 & 0 & C_{66} \end{pmatrix} \begin{pmatrix} \Delta\epsilon_t \\ \Delta\epsilon_t \\ \Delta\epsilon_n \\ 0 \\ 0 \\ 0 \end{pmatrix}. \tag{B.3}$$

From Equation B.3 we can therefore relate changes in normal and transverse stresses and strain by–

$$\Delta\sigma_n = C_{33}\Delta\epsilon_n^e + 2C_{13}\Delta\epsilon_t^e, \tag{B.4}$$

$$\Delta\sigma_t = C_{13}\Delta\epsilon_n^e + (C_{11} + C_{12})\,\Delta\epsilon_t^e. \tag{B.5}$$

Since the sample is laterally confined, the total normal strain will also be the change in the volume of the sample, while the total transverse strain is zero.

$$\Delta\epsilon_n^T = \Delta\epsilon_n^e + \Delta\epsilon_n^p = \Delta V/V, \tag{B.6}$$

$$\Delta\epsilon_t^T = \Delta\epsilon_t^e + \Delta\epsilon_t^p = 0. \tag{B.7}$$

Additionally, changes in elastic strain can be related to the change in the volume of the sample, while plastic strains cannot lead to a net volume change–

$$\Delta\epsilon_n^e + 2\Delta\epsilon_t^e = \Delta V/V, \tag{B.8}$$

$$\Delta\epsilon_n^p + 2\Delta\epsilon_t^p = 0. \tag{B.9}$$

By inserting B.6 and B.8 into B.4, we find–

$$\Delta\sigma_n = C_{33}\left(\Delta\epsilon_n^T - 2\Delta\epsilon_t^e\right) + 2C_{13}\Delta\epsilon_t^e, \tag{B.10}$$

$$\Delta\sigma_n = C_{33}\Delta\epsilon_n^T + 2\left(C_{13} - C_{33}\right)\Delta\epsilon_t^e. \tag{B.11}$$

Using B.7 with B.11, we obtain–

$$\Delta\sigma_n = C_{33}\Delta\epsilon_n^T - 2\left(C_{13} - C_{33}\right)\Delta\epsilon_t^p. \tag{B.12}$$

Inserting B.9 into B.12, we get–

$$\Delta\sigma_n = C_{33}\Delta\epsilon_n^T - 2\left(C_{13} - C_{33}\right)\left[\Delta\epsilon_t^p - \frac{1}{3}\left(\Delta\epsilon_t^p + 2\Delta\epsilon_n^p\right)\right], \tag{B.13}$$

$$\Delta\sigma_n = C_{33}\Delta\epsilon_n^T - \frac{4}{3}\left(C_{33} - C_{31}\right)\gamma, \tag{B.14}$$

where γ is the plastic shear strain given by $(\epsilon_t^p - \epsilon_n^p)$. From Orowan's equation [135, 31], plastic strain rate is given by $\dot{\gamma} = Nbv$, where N is the dislocation density, b is the magnitude of their Burgers vector and v is their velocity. By taking derivates of Equation B.15 with respect to time, we find–

$$\frac{\partial\sigma_n}{\partial t} = C_{33}\frac{\partial\epsilon_n^T}{\partial t} - \frac{4}{3}\left(C_{33} - C_{31}\right)Nbv. \tag{B.15}$$

The model by Taylor assumes that the dislocation density and their velocity can be represented by–

$$N = N_0 + \alpha\gamma, \tag{B.16}$$

$$v = v_\infty \exp\left[-\left(\tau_0 + \Phi\gamma\right)/\tau\right], \tag{B.17}$$

where Φ is a constant that represents work hardening, v_∞ is the shear wave velocity and τ is the shear stress. By combining Equations B.16 and B.17 with Equation B.15, we obtain–

$$\frac{\partial\sigma_n}{\partial t} - C_{33}\frac{\partial\epsilon_n^T}{\partial t} = -g\left(\sigma, \epsilon\right), \tag{B.18}$$

$$g\left(\sigma_n, \epsilon_n\right) = \frac{4}{3}\left(C_{33} - C_{31}\right)\left(N_0 + \alpha\gamma\right)v_\infty \exp\left[-\left(\tau_0 + \Phi\gamma/\tau\right)\right]. \tag{B.19}$$

Note that to ensure an initial elastic response, we set $g = 0$ when σ_n is smaller than a given HEL and when $|\epsilon_t^e|$ is larger than an arbitrarily small threshold.

In order to integrate these equation, we use a simple two step method developed by Horie [136, 137, 131].

$$\Delta\epsilon_n^T\left(p+1, j\right) = \left(R^2/\rho_0\right)\sum_{q=0}^{p}\left[\sigma_n\left(q, j+1\right) - 2\sigma_n\left(q, j\right) + \sigma_n\left(q, j-1\right)\right]. \tag{B.20}$$

$$\Delta\sigma_n\left(p+1, j\right) = \left\langle C_L^2\right\rangle R^2\sum_{q=0}^{p}\left[\sigma_n\left(q, j+1\right) - 2\sigma_n\left(q, j\right) + \sigma_n\left(q, j-1\right)\right] - g\left(\sigma, \epsilon\right)\Delta t. \tag{B.21}$$

By rearranging Equations B.4, B.6 and B.8, we find–

$$\Delta\sigma_n = C_{33}\left(\Delta\epsilon_n^T - 2\Delta\epsilon_t^e\right) + 2C_{13}\Delta\epsilon_t^e, \tag{B.22}$$

$$\Delta\sigma_n = C_{33}\Delta\epsilon_n^T + 2\left(C_{13} - C_{33}\right)\Delta\epsilon_t^e, \tag{B.23}$$

$$\Delta\epsilon_t^e = \frac{\Delta\sigma_n - C_{33}\Delta\epsilon_n^T}{2\left(C_{13} - C_{33}\right)}. \tag{B.24}$$

Since Equations B.20 and B.24 allow us to calculate the change in total normal strain and transverse elastic strain, Equations B.6 to B.9 can be used to find the other elastic and plastic strains. Lastly, we calculate the change in transverse stress using Equation B.5.

The stresses and strains are updated as follows–

$$\sigma \leftarrow \sigma + \Delta\sigma, \tag{B.25}$$

$$\epsilon \leftarrow \left[1 - (1-\epsilon)(1-\Delta\epsilon)\right]. \tag{B.26}$$

The updating of strains is more complex then simple addition since we are using engineering strains rather than true strain. Once we have obtain the total normal stress and strains, the change in elastic and plastic strain as well as transverse stress can be obtained by Equations B.4 and B.4. Equations B.25 and B.26 can now be used to update these values.

APPENDIX C

Lattice Rotation

Consider the case of a strained laterally confined crystal, as shown in shown in Figure C.1 and outlined Kelly & Knowles [35]. Although for ease of illustration the tension case is shown, the same analysis is equally valid for the compressive case, with the direction of slip reversed. The system initially has loading axis along OA, and the system is laterally confined such that after glide the system will rotate such that OA' remains vertical.

We denote the vector OA as $\mathbf{r}$ and OA' as $\mathbf{r}'$. Therefore, for a glide of γ, we find–

$$\mathbf{r}' = \mathbf{r} + \gamma\left(\mathbf{r} \cdot \mathbf{n}\right)\beta, \tag{C.1}$$

where $\mathbf{n}$ is the unit vector normal to the slip plane and β is the slip direction.

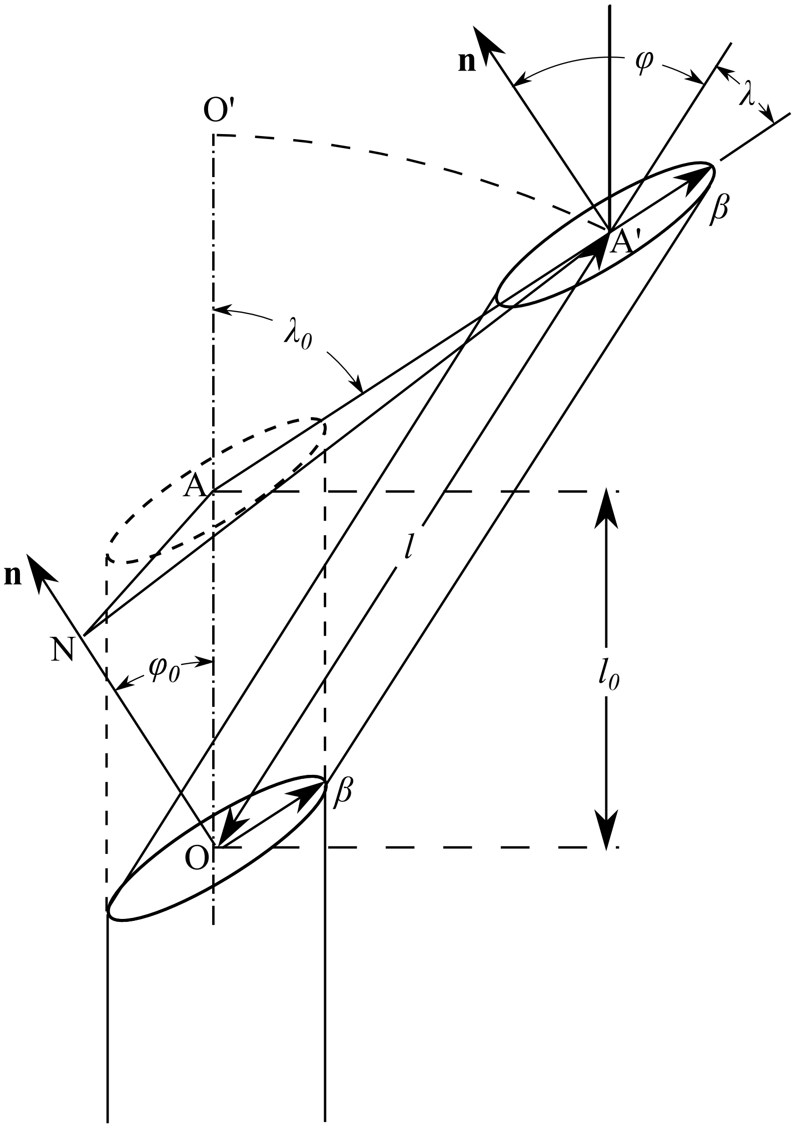

Figure C.1: The geometry of lattice rotation due to glide.

The length of $\mathbf{r}$ and $\mathbf{r}'$ will give the length of the crystal along the loading axis before and after compression respectively–

$$\frac{l}{l_0} = (1+e) = \frac{|\mathbf{r}'|}{|\mathbf{r}|}. \tag{C.2}$$

The angle ϕ between the new loading axis OA' and $\mathbf{n}$ will be given by–

$$\cos\phi = \frac{\mathbf{r}'\cdot\mathbf{n}}{|\mathbf{r}'|}, \tag{C.3}$$

$$\cos\phi = \frac{(\mathbf{r}+\gamma\,(\mathbf{r}\cdot\mathbf{n})\,\beta)\cdot\mathbf{n}}{|\mathbf{r}'|}, \tag{C.4}$$

$$\cos\phi = \frac{\mathbf{r}\cdot\mathbf{n}+\gamma\,(\mathbf{r}\cdot\mathbf{n})\,(\beta\cdot\mathbf{n})}{|\mathbf{r}'|}. \tag{C.5}$$

Since $\cos\phi = \frac{\mathbf{r}\cdot\mathbf{n}}{|\mathbf{r}|}$ and $\beta\cdot\mathbf{n} = 0$, we find–

$$\frac{l}{l_0} = \frac{\cos\phi_0}{\cos\phi}. \tag{C.6}$$

This analysis only considers plastic deformation, so the change in h is related to the total plastic strain in the normal direction $\frac{l}{l_0} = (1+\epsilon_n^p)$. Note that we will be using the deformation gradient $F = 1+\epsilon$.

The volume change of the sample will be equal to the product of the elastic deformations–

$$F_x^e F_y^e F_z^e = \frac{V}{V_0}, \tag{C.7}$$

while the plastic strains do not change the volume of the sample–

$$F_x^p F_y^p F_z^p = 1. \tag{C.8}$$

Additionally we make the assumption that after compression the material will remain hydrostatic and thus the elastic strains will be equal in all directions–

$$F^e_x = F^e_y = F^e_z. \tag{C.9}$$

Finally, since the material is laterally constrained, we assume that while individual grains may expand or contract in different transverse directions, the area of each grain transverse to the sample normal will remain the same. Thus we find that the product of the total strain in the two transverse directions remains the same–

$$F^e_x F^p_x F^e_y F^p_y = 1. \tag{C.10}$$

Inserting Equation C.9 into Equation C.10, we find–

$$(F^e_x)^2 F^p_x F^p_y = 1. \tag{C.11}$$

Substituting Equation C.11 into Equation C.8, we find–

$$F^p_z = (F^e_x)^2. \tag{C.12}$$

Substituting Equation C.9 into Equation C.7, we find–

$$(F^e_x)^3 = \frac{V}{V_0}. \tag{C.13}$$

Finally, by inserting Equation C.13 into Equation C.12, we find–

$$F^p_z = \left(\frac{V}{V_0}\right)^{2/3}. \tag{C.14}$$

Since we know that $\frac{l}{l_0} = (F_z^p)$, we find–

$$\frac{\cos\phi_0}{\cos\phi} = \left(\frac{V}{V_0}\right)^{2/3}, \tag{C.15}$$

$$\cos\phi = \cos\phi_0 \left(\frac{V}{V_0}\right)^{-2/3}. \tag{C.16}$$

Lastly, the rotation of the crystal ω is given by the difference of ϕ and ϕ_0–

$$\omega = \phi - \phi_0 = \arccos\left(\cos\phi_0 \left(\frac{V}{V_0}\right)^{-2/3}\right) - \phi_0. \tag{C.17}$$

If rotation due to slip is initially suppressed, for example by another plasticity mechanism, we can replace V_0 with the volume at which slip starts to occur (V_s)–

$$\omega = \phi - \phi_0 = \arccos\left(\cos\phi_0 \left(\frac{V}{V_s}\right)^{-2/3}\right) - \phi_0. \tag{C.18}$$

Plastic shear is given by the difference between F_z^p and F_x^p. Combining C.14 and C.8, and assuming $F_y^p = 1$–

$$F_x^p F_y^p \left(\frac{V}{V_0}\right)^{2/3} = 1, \tag{C.19}$$

$$F_x^p = \left(\frac{V}{V_0}\right)^{-2/3}. \tag{C.20}$$

This gives a plastic shear of–

$$\gamma^p = F_x^p - F_z^p \tag{C.21}$$

$$\gamma^p = \left(\frac{V_0}{V}\right)^{2/3} - \left(\frac{V}{V_0}\right)^{2/3}, \tag{C.22}$$

or alternatively–

$$\gamma^p = \frac{\cos\phi_0}{\cos\phi} - \frac{\cos\phi}{\cos\phi_0}. \tag{C.23}$$

APPENDIX D

Detector Fitting Routine

In order to fit the positions of the X-ray detectors, a series of diffraction images of calibration materials are taken. CeO_2 and LaB_6 are often used as calibrates as they give a diffraction pattern that has a number of well defined lines in the Q range that is relevant for X-ray diffraction. However, other calibrates such as MoO_3 and Silver behenate are also used, usually to fit detectors at lower scattering angles, as they have more lines at higher Q. Multiple diffraction images are summed together to provide a better signal to noise. Figure D.1 shows the image produced by summing 20 CeO_2 diffraction patterns at 9.6keV. The code requires an initial guess at the position and orientation of detector. This is given by a position vector from the sample to the centre of the detector and three Tait-Bryan angles defining yaw, pitch

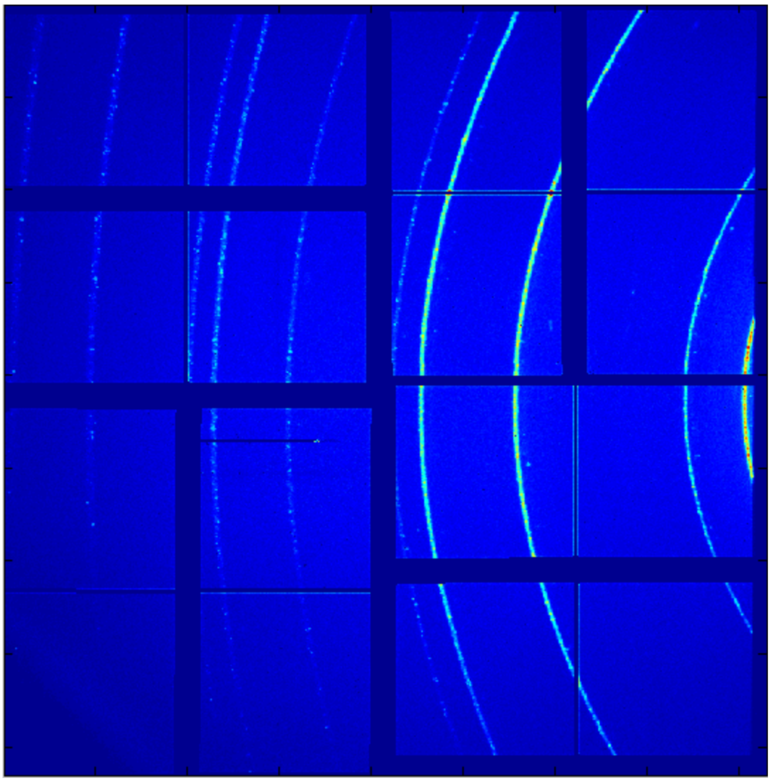

Figure D.1: The integrated diffraction pattern from a CeO_2 calibrant at 9.6 keV.

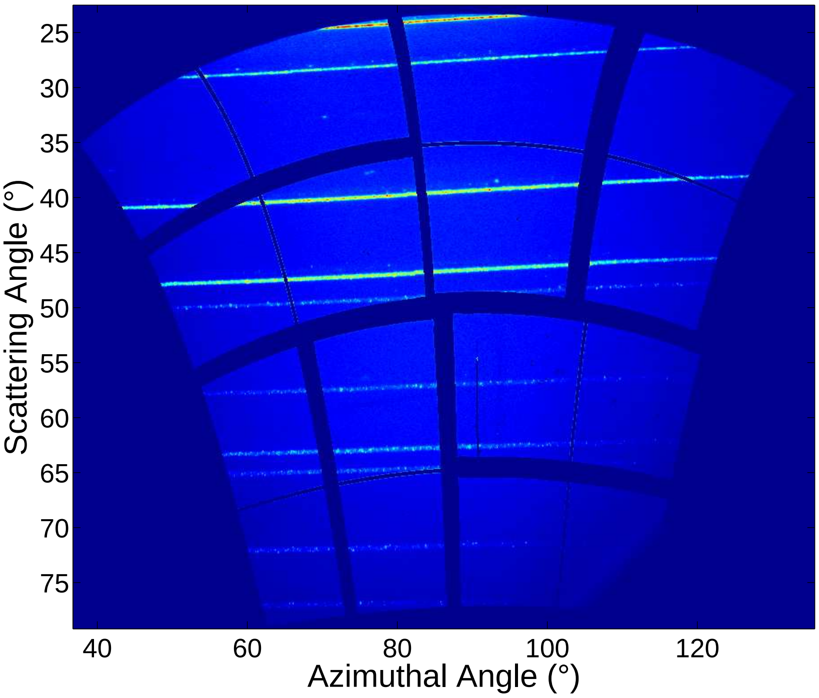

Figure D.2: The diffraction pattern warped into θ-ϕ space given the initial guess at the detector position and orientation.

and roll–

$$\mathbf{R} = \begin{pmatrix} \cos a & 0 & \sin a \\ 0 & 1 & 0 \\ -\sin a & 0 & \cos a \end{pmatrix} \begin{pmatrix} 1 & 0 & 0 \\ 0 & \cos b & \sin b \\ 0 & -\sin b & \cos b \end{pmatrix} \begin{pmatrix} \cos c & \sin c & 0 \\ -\sin c & \cos c & 0 \\ 0 & 0 & 1 \end{pmatrix}. \quad \text{(D.1)}$$

The code then bins the data in θ-ϕ space by assuming the initial guess at the detector position and orientation, as shown in figure D.2. The warped image is divided up into a number of sections that are equally distributed in ϕ which are then integrated to form lineouts. Since the d-spacings for each of the lines of the calibrants is known, the code attempts to fit a Pseudo-Voigt profile within a pre-defined range of where it expects each peak to be.

The code moves from the left to the right of the warped image, attempting to fit each lineout. To reduce the amount of erroneous fitting, the fit is only accepted if the following conditions are met–

- The width of the fitted peak is within an expected range
- The height of the peak is within a threshold value
- The RMS error is below a threshold value

Once the code detects a peak, it takes the peak centre to be the expect centre position for the next lineout. By fitting all the lineouts from left to right and then refitting the lineouts from right to left, the code has the ability to fit the position of each peak over the entire azimuthal range even if it only briefly crosses the expected scattering angle. Once the θ-ϕ positions of each diffraction peak is known, they can be converted back to position on the detector. Note that even with the conditions listed above, some features in the detector image will still incorrectly identified as a calibration line. Once the peak positions on the detector is known, the scattering angle and hence measured d-spacing of each of the lines can be calculated as a function of the three position coordinates of the detector centre and three Tait-Bryan angles to define the detector orientation. The code then uses a multiple variable fitting routine to minimise the difference between measured d-spacing and expected d-spacing as a function of these 6 variables. Figure D.4 shows the calibrant diffraction pattern warped in θ-ϕ space with the fitted detector position. It can often be useful to take use these position as an initial guess in the code and refit the positions to obtain a more accurate fit. By fitting several detectors it is possible to combine the data into a composite image. Figure D.5 and D.6 show the data from several CSPads warped into θ-ϕ and projected onto a plane respectively.

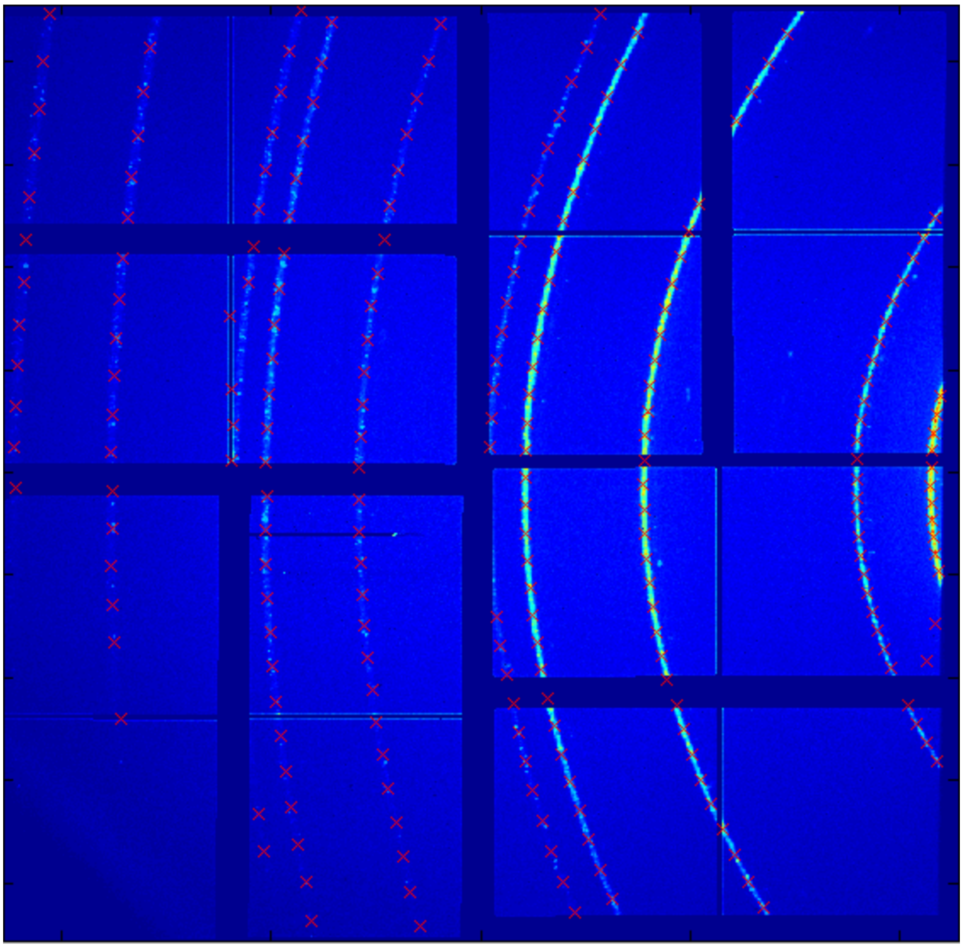

Figure D.3: The measured positions of the centre of each calibration line.

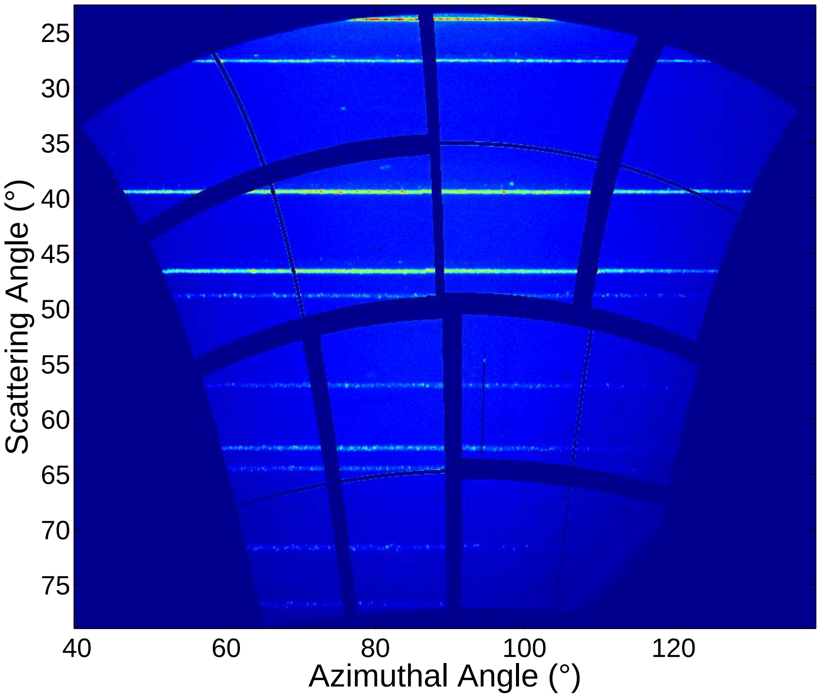

Figure D.4: The diffraction pattern warped into θ-ϕ space with the fitted detector position and orientation.

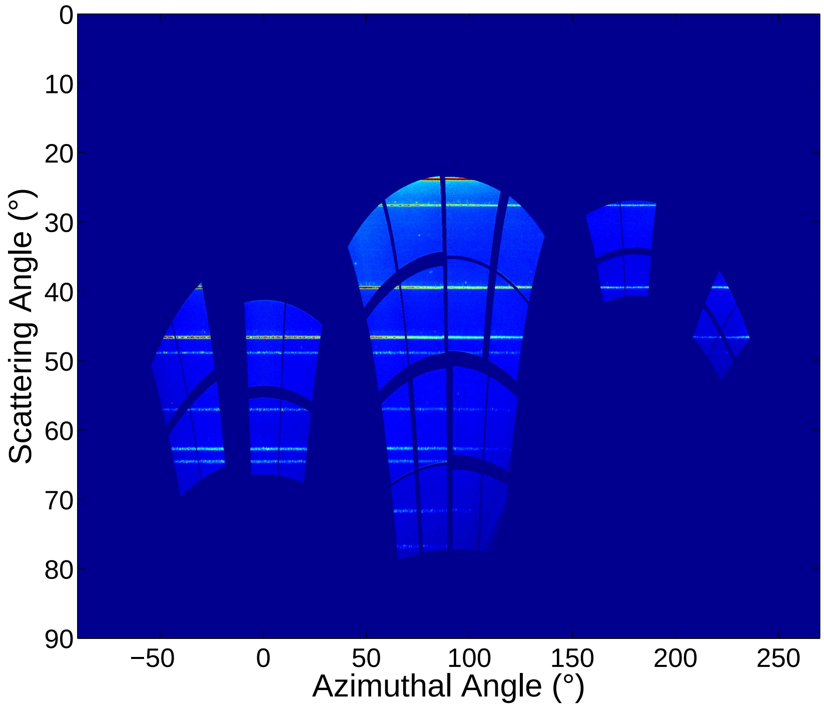

Figure D.5: All the CSPad images from a CeO_2 calibrant combined into a single θ-ϕ image.

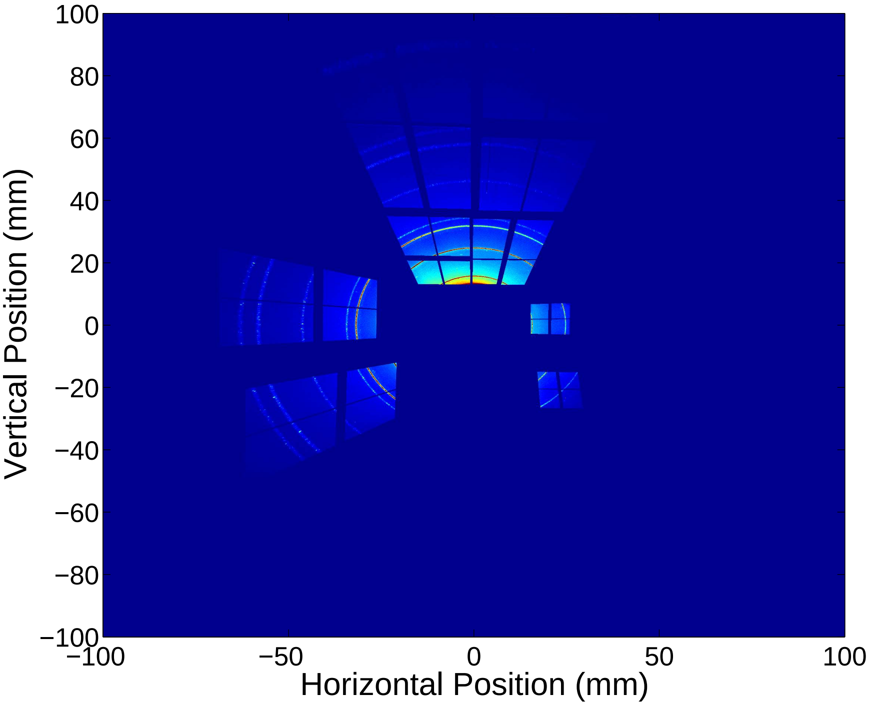

Figure D.6: All the CSPad images from a CeO_2 calibrant projected onto a flat plane 30 mm from the target along the X-ray direction.

References

[1] D Milathianaki, S Boutet, G J Williams, et al. Femtosecond visualization of lattice dynamics in shock-compressed matter. *Science*, 342 (6155):220–3, October 2013. ISSN 1095-9203. doi: 10.1126/science.1239566.

[2] W J Macquorn Rankine. On the thermodynamic theory of waves of finite longitudinal disturbance. *Philos. Trans. R. Soc. London*, pages 277–288, 1870.

[3] P H Hugoniot. Memoire sur la propagation des mouvements dans les corps et specialement dans les gaz parfaits (premier partie). *J. L'Ecole Polytech.*, pages 3–97, 1887.

[4] John M. Walsh and Russell H. Christian. Equation of State of Metals from Shock Wave Measurements. *Phys. Rev.*, 97(6):1544–1556, March 1955. ISSN 0031-899X. doi: 10.1103/PhysRev.97.1544.

[5] John M. Walsh, Melvin H. Rice, Robert G. McQueen, and Frederick L. Yarger. Shock-Wave Compressions of Twenty-Seven Metals. Equations of State of Metals. *Phys. Rev.*, 108(2):196–216, October 1957. ISSN 0031-899X. doi: 10.1103/PhysRev.108.196.

[6] A. H. Jones. Measurement of the Very-High-Pressure Properties of Materials using a Light-Gas Gun. *J. Appl. Phys.*, 37(9):3493, 1966. ISSN 00218979. doi: 10.1063/1.1708887.

[7] D. Batani, H. Stabile, A. Ravasio, et al. Ablation pressure scaling at short laser wavelength. *Phys. Rev. E*, 68(6):1–4, December 2003. ISSN 1063-651X. doi: 10.1103/PhysRevE.68.067403.

[8] R. F. Smith, J. H. Eggert, R. Jeanloz, et al. Ramp compression of diamond to five terapascals. *Nature*, 511(7509):330–333, July 2014. ISSN 0028-0836. doi: 10.1038/nature13526.

[9] L. M. Barker. Laser interferometer for measuring high velocities of any reflecting surface. *J. Appl. Phys.*, 43(11):4669, 1972. ISSN 00218979. doi: 10.1063/1.1660986.

[10] Quintin Johnson, A. Mitchell, R. Keeler, and L. Evans. X-Ray Diffraction During Shock-Wave Compression. *Phys. Rev. Lett.*, 25(16):1099–1101, October 1970. ISSN 0031-9007. doi: 10.1103/PhysRevLett.25.1099.

[11] Quintin Johnson. X-ray diffraction study of single crystals undergoing shock-wave compression. *Appl. Phys. Lett.*, 21(1):29, 1972. ISSN 00036951. doi: 10.1063/1.1654205.

[12] Quintin Johnson and A Mitchell. First X-Ray Diffraction Evidence for a Phase Transition during Shock-Wave Compression. *Phys. Rev. Lett.*, 29(20):1369–1371, November 1972. ISSN 0031-9007. doi: 10.1103/PhysRevLett.29.1369.

[13] E. Förster, K Goetz, K. Schäfer, and W D Zimmer. Laser generated plasma as a source for real time studies in X-ray crystal research: Part I: Fundamental remarks about source characteristics and requirements. *Laser Part. Beams*, 2(02):167, March 1984. ISSN 0263-0346. doi: 10.1017/S0263034600000744.

[14] K. Schäfer and W D Zimmer. Laser generated plasmas as a source for real time studies in X-ray crystal research: Part II: In search of an optimum choice of laser plasma coupling conditions. *Laser Part. Beams*, 2(02):187, March 1984. ISSN 0263-0346. doi: 10.1017/S0263034600000756.

[15] J. S. Wark, R. Whitlock, A. Hauer, et al. Shock launching in silicon studied with use of pulsed x-ray diffraction. *Phys. Rev. B*, 35(17):9391–9394, June 1987. ISSN 0163-1829. doi: 10.1103/PhysRevB.35.9391.

[16] Justin S. Wark, Robert Whitlock, Allan Hauer, et al. Subnanosecond x-ray diffraction from laser-shocked crystals. *Phys. Rev. B*, 40(8):5705–5714, September 1989. ISSN 0163-1829. doi: 10.1103/PhysRevB.40.5705.

[17] D. H. Kalantar, J. Belak, G. W. Collins, et al. Direct Observation of the α-ϵ Transition in Shock-Compressed Iron via Nanosecond X-Ray Diffraction. *Phys. Rev. Lett.*, 95(7):1–4, August 2005. ISSN 0031-9007. doi: 10.1103/PhysRevLett.95.075502.

[18] D.H. Kalantar, G.W. Collins, J.D. Colvin, et al. In situ diffraction measurements of lattice response due to shock loading, including direct observation of the α–ϵ phase transition in iron. *Int. J. Impact Eng.*, 33(1-12):343–352, December 2006. ISSN 0734743X. doi: 10.1016/j.ijimpeng.2006.09.050.

[19] M G Gorman, R Briggs, E E McBride, et al. Direct Observation of Melting in Shock-Compressed Bismuth With Femtosecond X-ray Diffraction. *Phys. Rev. Lett.*, 115(9):095701, August 2015. ISSN 1079-7114. doi: 10.1103/PhysRevLett.115.095701.

[20] A E Gleason, C A Bolme, H J Lee, et al. Ultrafast visualization of crystallization and grain growth in shock-compressed SiO2. *Nat. Commun.*, 6:8191, January 2015. ISSN 2041-1723. doi: 10.1038/ncomms9191.

[21] J M Walsh. Metal Equation of State from Shock Wave Studies. Technical report, Los Alamos Scientific Lab., 1953.

[22] Dennison Bancroft, Eric L. Peterson, and Stanley Minshall. Polymorphism of Iron at High Pressure. *J. Appl. Phys.*, 27(3):291, March 1956. ISSN 00218979. doi: 10.1063/1.1722359.

[23] Kai Kadau, Timothy C Germann, Peter S Lomdahl, and Brad Lee Holian. Microscopic view of structural phase transitions induced by shock waves. *Science*, 296(5573):1681–4, May 2002. ISSN 1095-9203. doi: 10.1126/science.1070375.

[24] Kai Kadau, Timothy Germann, Peter Lomdahl, et al. Shock Waves in Polycrystalline Iron. *Phys. Rev. Lett.*, 98(13):1–4, March 2007. ISSN 0031-9007. doi: 10.1103/PhysRevLett.98.135701.

[25] James Hawreliak, Bassem El-Dasher, Hector E Lorenzana, et al. In situ x-ray diffraction measurements of the c/a ratio in the high-pressure ϵ phase of shock-compressed polycrystalline iron. *Phys. Rev. B*, 83(14):1–6, April 2011. ISSN 1098-0121. doi: 10.1103/PhysRevB.83.144114.

[26] Matthew J Suggit, Andrew Higginbotham, James a Hawreliak, et al. Nanosecond white-light Laue diffraction measurements of dislocation microstructure in shock-compressed single-crystal copper. *Nat. Commun.*, 3:1224, January 2012. ISSN 2041-1723. doi: 10.1038/ncomms2225.

[27] C. E. Wehrenberg, A. J. Comley, N. R. Barton, et al. Lattice-level observation of the elastic-to-plastic relaxation process with subnanosecond resolution in shock-compressed Ta using time-resolved in situ Laue diffraction. *Phys. Rev. B*, 92(10):104305, September 2015. ISSN 1098-0121. doi: 10.1103/PhysRevB.92.104305.

[28] A. J. Comley, B. R. Maddox, R. E. Rudd, et al. Strength of Shock-Loaded Single-Crystal Tantalum [100] Determined using In Situ Broadband X-Ray Laue Diffraction. *Phys. Rev. Lett.*, 110(11):115501, March 2013. ISSN 0031-9007. doi: 10.1103/PhysRevLett.110.115501.

[29] Andrew Higginbotham and David McGonegle. Prediction of Debye-Scherrer diffraction patterns in arbitrarily strained samples. *J. Appl. Phys.*, 115(17):174906, May 2014. ISSN 0021-8979. doi: 10.1063/1.4874656.

[30] David McGonegle, Despina Milathianaki, Bruce A. Remington, et al. Simulations of in situ x-ray diffraction from uniaxially compressed highly textured polycrystalline targets. *J. Appl. Phys.*, 118(6):065902, August 2015. ISSN 0021-8979. doi: 10.1063/1.4927275.

[31] Marc Andre Meyers. *Dynamic Behavior of Materials.* John Wiley & Sons, Inc., Hoboken, NJ, USA, September 1994. ISBN 9780470172278. doi: 10.1002/9780470172278.

[32] Derek Hull and David J Bacon. *Introduction to dislocations*, volume 257. Pergamon Press Oxford, 1984.

[33] William F Hosford. *Mechanical behavior of materials.* Cambridge University Press, 2010.

[34] Neil W Ashcroft and N David Mermin. *Solid State Physics.* Harcourt, 1976.

[35] Anthony A Kelly and Kevin M Knowles. *Crystallography and crystal defects.* John Wiley & Sons, 2012.

[36] Charles Kittel. *Introduction to solid state physics.* Wiley, 2005.

[37] Bertram Eugene Warren. *X-ray Diffraction.* Courier Corporation, 1969.

[38] M H Rice, R G McQueen, and J M Walsh. Compression of solids by strong shock waves. *Solid state Phys.*, 6:1–63, 1958.

[39] Stanley Minshall. Properties of Elastic and Plastic Waves Determined by Pin Contactors and Crystals. *J. Appl. Phys.*, 26(4):463, 1955. ISSN 00218979. doi: 10.1063/1.1722019.

[40] G. R. Fowles. Shock Wave Compression of Hardened and Annealed 2024 Aluminum. *J. Appl. Phys.*, 32(8):1475, 1961. ISSN 00218979. doi: 10.1063/1.1728382.

[41] D. B. Hayes. Polymorphic phase transformation rates in shock-loaded potassium chloride. *J. Appl. Phys.*, 45(3):1208, 1974. ISSN 00218979. doi: 10.1063/1.1663391.

[42] J. W. Swegle and D. E. Grady. Shock viscosity and the prediction of shock wave rise times. *J. Appl. Phys.*, 58(2):692, 1985. ISSN 00218979. doi: 10.1063/1.336184.

[43] A. Reuss. Berechnung der Fließgrenze von Mischkristallen auf Grund der Plastizitätsbedingung für Einkristalle . *ZAMM - Zeitschrift für Angew. Math. und Mech.*, 9(1):49–58, 1929. ISSN 00442267. doi: 10.1002/zamm.19290090104.

[44] Woldemar Voigt. *Lehrbuch der kristallphysik:(mit ausschluss der kristalloptik)*. BG Teubner, 1928.

[45] E Orowan. Plasticity of crystals. *Z. Phys*, 89(9-10):605–659, 1934.

[46] M. Polanyi. Über eine Art Gitterstörung, die einen Kristall plastisch machen könnte. *Zeitschrift für Phys.*, 89(9-10):660–664, September 1934. ISSN 1434-6001. doi: 10.1007/BF01341481.

[47] G I Taylor. The Mechanism of Plastic Deformation of Crystals . 145 (855):362–387, 2015.

[48] H-R Wenk and P Van Houtte. Texture and anisotropy. *Reports Prog. Phys.*, 67(8):1367–1428, August 2004. ISSN 0034-4885. doi: 10.1088/0034-4885/67/8/R02.

[49] H R Wenk, F Heidelbach, D Chateigner, and F Zontone. Laue orientation imaging. *J. Synchrotron Radiat.*, 4(Pt 2):95–101, March 1997. ISSN 0909-0495. doi: 10.1107/S090904959601432X.

[50] H.-R. Wenk and S. Grigull. Synchrotron texture analysis with area detectors. *J. Appl. Crystallogr.*, 36(4):1040–1049, July 2003. ISSN 0021-8898. doi: 10.1107/S0021889803010136.

[51] H.-R. Wenk, G. Ischia, N. Nishiyama, et al. Texture development and deformation mechanisms in ringwoodite. *Phys. Earth Planet. Inter.*, 152(3):191–199, September 2005. ISSN 00319201. doi: 10.1016/j.pepi.2005.06.008.

[52] Gloria Ischia, Hans-Rudolf Wenk, Luca Lutterotti, and Florian Berberich. Quantitative Rietveld texture analysis of zirconium from

single synchrotron diffraction images. *J. Appl. Crystallogr.*, 38(2):377–380, March 2005. ISSN 0021-8898. doi: 10.1107/S0021889805006059.

[53] Nathan R. Barton and Joel V. Bernier. A method for intragranular orientation and lattice strain distribution determination. *J. Appl. Crystallogr.*, 45(6):1145–1155, November 2012. ISSN 0021-8898. doi: 10.1107/S0021889812040782.

[54] Sven C. Vogel, Helmut Reiche, and Donald W. Brown. High pressure deformation study of zirconium. *Powder Diffr.*, 22(02):113–117, March 2012. ISSN 0885-7156. doi: 10.1154/1.2737459.

[55] Norbert Stribeck. On the determination of fiber tilt angles in fiber diffraction. *Acta Crystallogr. A.*, 65(Pt 1):46–7, January 2009. ISSN 1600-5724. doi: 10.1107/S0108767308029772.

[56] M. Polanyi. Das Röntgen-Faserdiagramm (Erste Mitteilung). *Zeitschrift für Phys.*, 7(1):149–180, December 1921. ISSN 1434-6001. doi: 10.1007/BF01332786.

[57] M. Polanyi and K. Weissenberg. Das Röntgen-Faserdiagramm (Zweite Mitteflung). *Zeitschrift für Phys.*, 9(1):123–130, December 1922. ISSN 1434-6001. doi: 10.1007/BF01326961.

[58] Loup Verlet. Computer "Experiments" on Classical Fluids. I. Thermodynamical Properties of Lennard-Jones Molecules. *Phys. Rev.*, 159(1): 98–103, July 1967. ISSN 0031-899X. doi: 10.1103/PhysRev.159.98.

[59] Steve Plimpton. Fast Parallel Algorithms for Short-Range Molecular Dynamics. *J. Comput. Phys.*, 117(1):1–19, March 1995. ISSN 00219991. doi: 10.1006/jcph.1995.1039.

[60] J. E. Jones. On the Determination of Molecular Fields. II. From the Equation of State of a Gas. *Proc. R. Soc. A Math. Phys. Eng. Sci.*, 106(738):463–477, October 1924. ISSN 1364-5021. doi: 10.1098/rspa.1924.0082.

[61] Murray S Daw and M I Baskes. Semiempirical, Quantum Mechanical Calculation of Hydrogen Embrittlement in Metals. *Phys. Rev. Lett.*, 50(17):1285–1288, April 1983. doi: 10.1103/PhysRevLett.50.1285.

[62] R. J. Harrison, A. F. Voter, and S.-P. Chen. *Atomistic Simulation of Materials: Beyond Pair Potentials.* Springer US, Boston, MA, 1989. ISBN 978-1-4684-5705-6. doi: 10.1007/978-1-4684-5703-2.

[63] R. Ravelo, T. C. Germann, O. Guerrero, et al. Shock-induced plasticity in tantalum single crystals: Interatomic potentials and large-scale molecular-dynamics simulations. *Phys. Rev. B*, 88(13):134101, October 2013. ISSN 1098-0121. doi: 10.1103/PhysRevB.88.134101.

[64] Giles Kimminau, Bob Nagler, Andrew Higginbotham, et al. Simulating picosecond x-ray diffraction from shocked crystals using post-processing molecular dynamics calculations. *J. Phys. Condens. Matter*, 20(50):505203, December 2008. ISSN 0953-8984. doi: 10.1088/0953-8984/20/50/505203.

[65] C. Pellegrini. The history of X-ray free-electron lasers. *Eur. Phys. J. H*, 37(5):659–708, June 2012. ISSN 2102-6459. doi: 10.1140/epjh/e2012-20064-5.

[66] G Margaritondo and Primoz Rebernik Ribic. A simplified description of X-ray free-electron lasers. *J. Synchrotron Radiat.*, 18(Pt 2):101–8, March 2011. ISSN 1600-5775. doi: 10.1107/S090904951004896X.

[67] W. Ackermann, G. Asova, V. Ayvazyan, et al. Operation of a free-electron laser from the extreme ultraviolet to the water window. *Nat. Photonics*, 1(6):336–342, June 2007. ISSN 1749-4885. doi: 10.1038/nphoton.2007.76.

[68] K Tiedtke, A Azima, N von Bargen, et al. The soft x-ray free-electron laser FLASH at DESY: beamlines, diagnostics and end-stations. *New J. Phys.*, 11(2):023029, February 2009. ISSN 1367-2630. doi: 10.1088/1367-2630/11/2/023029.

[69] P Emma, R Akre, J Arthur, et al. First lasing and operation of an ångstrom-wavelength free-electron laser. *Nat. Photonics*, 4(9):641–647, August 2010. ISSN 1749-4885. doi: 10.1038/nphoton.2010.176.

[70] E Allaria, C Callegari, D Cocco, et al. The FERMI@Elettra free-electron-laser source for coherent x-ray physics: photon properties, beam transport system and applications. *New J. Phys.*, 12(7):075002, July 2010. ISSN 1367-2630. doi: 10.1088/1367-2630/12/7/075002.

[71] Tetsuya Ishikawa, Hideki Aoyagi, Takao Asaka, et al. A compact X-ray free-electron laser emitting in the sub-ångström region. *Nat. Photonics*, 6(8):540–544, June 2012. ISSN 1749-4885. doi: 10.1038/nphoton.2012.141.

[72] European XFEL website. URL `http://www.xfel.eu/`.

[73] SwissFEL website. URL `https://www.psi.ch/swissfel/`.

[74] LCLS website. URL `https://lcls.slac.stanford.edu/`.

[75] Creative Commons License. URL `https://creativecommons.org/licenses/by-nc/2.0/`.

[76] Bob Nagler, Brice Arnold, Gary Bouchard, et al. The Matter in Extreme Conditions instrument at the Linac Coherent Light Source. *J. Synchrotron Radiat.*, 22(3):520–525, April 2015. ISSN 1600-5775. doi: 10.1107/S1600577515004865.

[77] Daniel H Dolan. Characterizing the emissivity of materials under dynamic compression (final report for LDRD project 79877). *Sandia Natl. Lab. Tech. Rep.*, SAND2007-6(October), 2007.

[78] William J. Evans, Choong-Shik Yoo, Geun Woo Lee, et al. Dynamic diamond anvil cell (dDAC): A novel device for studying the dynamic-pressure properties of materials. *Rev. Sci. Instrum.*, 78(7):073904, 2007. ISSN 00346748. doi: 10.1063/1.2751409.

[79] Eugene Gregoryanz, Lars F Lundegaard, Malcolm I McMahon, et al. Structural diversity of sodium. *Science*, 320(5879):1054–7, May 2008. ISSN 1095-9203. doi: 10.1126/science.1155715.

[80] I Loa, R J Nelmes, L F Lundegaard, and M I McMahon. Extraordinarily complex crystal structure with mesoscopic patterning in barium at high pressure. *Nat. Mater.*, 11(7):627–32, July 2012. ISSN 1476-1122. doi: 10.1038/nmat3342.

[81] MI McMahon, O Degtyareva, and RJ Nelmes. Ba-IV-type incommensurate crystal structure in group-V metals. *Phys. Rev. Lett.*, 85(23): 4896–9, December 2000. ISSN 1079-7114. doi: 10.1103/PhysRevLett.85.4896.

[82] J R Rygg, J H Eggert, A E Lazicki, et al. Powder diffraction from solids in the terapascal regime. *Rev. Sci. Instrum.*, 83(11):113904–113907, November 2012. ISSN 0034-6748. doi: 10.1063/1.4766464.

[83] G. W. Collins. Private Communication, 2013.

[84] Virginie Dupont and Timothy C. Germann. Strain rate and orientation dependencies of the strength of single crystalline copper under compression. *Phys. Rev. B*, 86(13):134111, October 2012. ISSN 1098-0121. doi: 10.1103/PhysRevB.86.134111.

[85] A. Higginbotham, M. J. Suggit, E. M. Bringa, et al. Molecular dynamics simulations of shock-induced deformation twinning of a body-centered-cubic metal. *Phys. Rev. B*, 88(10):104105, September 2013. ISSN 1098-0121. doi: 10.1103/PhysRevB.88.104105.

[86] S. I. Ashitkov, M. B. Agranat, G. I. Kanel', et al. Behavior of aluminum near an ultimate theoretical strength in experiments with femtosecond laser pulses. *JETP Lett.*, 92(8):516–520, December 2010. ISSN 0021-3640. doi: 10.1134/S0021364010200051.

[87] Jonathan C. Crowhurst, Michael R. Armstrong, Kimberly B. Knight, et al. Invariance of the Dissipative Action at Ultrahigh Strain Rates Above the Strong Shock Threshold. *Phys. Rev. Lett.*, 107(14):144302, September 2011. ISSN 0031-9007. doi: 10.1103/PhysRevLett.107.144302.

[88] V. H. Whitley, S. D. McGrane, D. E. Eakins, et al. The elastic-plastic response of aluminum films to ultrafast laser-generated shocks. *J. Appl. Phys.*, 109(1):013505, 2011. ISSN 00218979. doi: 10.1063/1.3506696.

[89] Anil K. Singh. The lattice strains in a specimen (cubic system) compressed nonhydrostatically in an opposed anvil device. *J. Appl. Phys.*, 73(9):4278, 1993. ISSN 00218979. doi: 10.1063/1.352809.

[90] J Hawreliak, H E Lorenzana, B. A. Remington, et al. Nanosecond x-ray diffraction from polycrystalline and amorphous materials in a pinhole camera geometry suitable for laser shock compression experiments. *Rev. Sci. Instrum.*, 78(8):083908, August 2007. ISSN 0034-6748. doi: 10.1063/1.2772210.

[91] Jean-Pierre Tignol. *Galois' theory of algebraic equations*. World Scientific, 2001.

[92] Quitin Johnson, Arthur Mitchell, and L Evans. X-ray Diffraction Evidence for Crystalline Order and Isotropic Compression during the Shock-wave Process. *Nature*, 231(5301):310–311, June 1971.

[93] Robert R Whitlock and Justin S Wark. Orthogonal strains and onset of plasticity in shocked LiF crystals. *Phys. Rev. B*, 52(1):8–11, July 1995. doi: 10.1103/PhysRevB.52.8.

[94] Y. M. Gupta, K. A. Zimmerman, P. A. Rigg, et al. Experimental developments to obtain real-time x-ray diffraction measurements in plate impact experiments. *Rev. Sci. Instrum.*, 70(10):4008, 1999. ISSN 00346748. doi: 10.1063/1.1150026.

[95] P A Rigg and Y M Gupta. Real-time x-ray diffraction to examine elastic–plastic deformation in shocked lithium fluoride crystals. *Appl. Phys. Lett.*, 73(12):1655–1657, 1998. doi: http://dx.doi.org/10.1063/1.122236.

[96] T. D'Almeida and Y. M. Gupta. Real-time X-ray diffraction measurements of the phase transition in KCl shocked along [100]. *Phys. Rev. Lett.*, 85:330–333, 2000. ISSN 00319007. doi: 10.1103/PhysRevLett.85.330.

[97] A. Loveridge-Smith, A. Allen, J. Belak, et al. Anomalous Elastic Response of Silicon to Uniaxial Shock Compression on Nanosecond Time Scales. *Phys. Rev. Lett.*, 86(11):2349–2352, March 2001. ISSN 0031-9007. doi: 10.1103/PhysRevLett.86.2349.

[98] Daniel H. Kalantar, J. Belak, E. M. Bringa, et al. High-pressure, high-strain-rate lattice response of shocked materials. *Phys. Plasmas*, 10 (5):1569, 2003. ISSN 1070664X. doi: 10.1063/1.1565118.

[99] J. Hawreliak, J. Colvin, J. H. Eggert, et al. Analysis of the x-ray diffraction signal for the α-ϵ transition in shock-compressed iron: Simulation and experiment. *Phys. Rev. B*, 74(18):1–16, November 2006. ISSN 1098-0121. doi: 10.1103/PhysRevB.74.184107.

[100] W J Murphy, A Higginbotham, G Kimminau, et al. The strength of single crystal copper under uniaxial shock compression at 100 GPa. *J. Phys. Condens. Matter*, 22(6):065404, February 2010. ISSN 1361-648X. doi: 10.1088/0953-8984/22/6/065404.

[101] Daniel H. Kalantar, E. M. Bringa, M. Caturla, et al. Multiple film plane diagnostic for shocked lattice measurements (invited). *Rev. Sci. Instrum.*, 74(3):1929, 2003. ISSN 00346748. doi: 10.1063/1.1538325.

[102] Matthew J Suggit, Giles Kimminau, James Hawreliak, et al. Nanosecond x-ray Laue diffraction apparatus suitable for laser shock compression experiments. *Rev. Sci. Instrum.*, 81(8):083902, August 2010. ISSN 1089-7623. doi: 10.1063/1.3455211.

[103] Andrew Higginbotham, Shamim Patel, James A Hawreliak, et al. Single photon energy dispersive x-ray diffraction. *Rev. Sci. Instrum.*, 85 (3):033906, March 2014. ISSN 1089-7623. doi: 10.1063/1.4867456.

[104] L Lutterotti, S Matthies, and H R Wenk. MAUD: a friendly Java program for material analysis using diffraction. *IUCr Newsl. CPD*, 21 (14-15), 1999.

[105] R. Hielscher and H. Schaeben. A novel pole figure inversion method: specification of the MTEX algorithm. *J. Appl. Crystallogr.*, 41 (6):1024–1037, November 2008. ISSN 0021-8898. doi: 10.1107/S0021889808030112.

[106] Alexander M Korsunsky, Mengyin Xie, Nikolaos Baimpas, and Xu Song. X-ray texture analysis and imaging of engineering materials at Oxford HEX-lab. In *Proc. Int. MultiConference Eng. Comput. Sci.*, volume 2012, 2012.

[107] M. Y. Xie, N. Baimpas, C. Reinhard, and A. M. Korsunsky. Texture analysis in cubic phase polycrystals by single exposure synchrotron X-ray diffraction. *J. Appl. Phys.*, 114(16):163502, 2013. ISSN 00218979. doi: 10.1063/1.4825120.

[108] D.W. Brown, S.R. Agnew, M.A.M. Bourke, et al. Internal strain and texture evolution during deformation twinning in magnesium. *Mater. Sci. Eng. A*, 399(1-2):1–12, June 2005. ISSN 09215093. doi: 10.1016/j.msea.2005.02.016.

[109] R. F. Smith, R. W. Minich, R. E. Rudd, et al. Orientation and rate dependence in high strain-rate compression of single-crystal silicon. *Phys. Rev. B*, 86(24):245204, December 2012. ISSN 1098-0121. doi: 10.1103/PhysRevB.86.245204.

[110] Hongxiang Zong, Turab Lookman, Xiangdong Ding, et al. Anisotropic shock response of titanium: Reorientation and transformation mechanisms. *Acta Mater.*, 65:10–18, February 2014. ISSN 13596454. doi: 10.1016/j.actamat.2013.11.047.

[111] Eduardo M Bringa, Alfredo Caro, Yinmin Wang, et al. Ultrahigh strength in nanocrystalline materials under shock loading. *Science*, 309(5742):1838–41, September 2005. ISSN 1095-9203. doi: 10.1126/science.1116723.

[112] H. N. Jarmakani, E. M. Bringa, P. Erhart, et al. Molecular dynamics simulations of shock compression of nickel: From monocrystals to nanocrystals. *Acta Mater.*, 56(19):5584–5604, November 2008. ISSN 13596454. doi: 10.1016/j.actamat.2008.07.052.

[113] Eduardo M. Bringa, Sirirat Traiviratana, and Marc A. Meyers. Void initiation in fcc metals: Effect of loading orientation and nanocrystalline effects. *Acta Mater.*, 58(13):4458–4477, August 2010. ISSN 13596454. doi: 10.1016/j.actamat.2010.04.043.

[114] Nina Gunkelmann, Eduardo M. Bringa, Diego R. Tramontina, et al. Shock waves in polycrystalline iron: Plasticity and phase transitions. *Phys. Rev. B*, 89(14):140102, April 2014. ISSN 1098-0121. doi: 10.1103/PhysRevB.89.140102.

[115] M P Usikov and V. A. Zilbershtein. The orientation relationship between the α- and ω-phases of titanium and zirconium. *Phys. Status Solidi*, 19(1):53–58, September 1973. ISSN 00318965. doi: 10.1002/pssa.2210190103.

[116] D. Trinkle, R. Hennig, S. Srinivasan, et al. New Mechanism for the α to ω Martensitic Transformation in Pure Titanium. *Phys. Rev. Lett.*,

91(2):025701, July 2003. ISSN 0031-9007. doi: 10.1103/PhysRevLett.91.025701.

[117] S. G. Song and G. T. Gray. Microscopic and crystallographic aspects of retained omega phase in shock-loaded zirconium and its formation mechanism. *Philos. Mag. A*, 71(2):275–290, February 1995. ISSN 0141-8610. doi: 10.1080/01418619508244356.

[118] J.M Silcock. An X-ray examination of the to phase in TiV, TiMo and TiCr alloys. *Acta Metall.*, 6(7):481–493, July 1958. ISSN 00016160. doi: 10.1016/0001-6160(58)90111-1.

[119] G. Jyoti, K. D. Joshi, Satish C. Gupta, and S. K. Sikka. Crystalography of the alpha-omega transition in shock-loaded zirconium. *Philos. Mag. Lett.*, 75(5):291–300, May 1997. ISSN 0950-0839. doi: 10.1080/095008397179543.

[120] L.E. Murr, M.A. Meyers, C.-S. Niou, et al. Shock-induced deformation twinning in tantalum. *Acta Mater.*, 45(1):157–175, January 1997. ISSN 13596454. doi: 10.1016/S1359-6454(96)00145-0.

[121] L.M. Hsiung and D.H. Lassila. Shock-induced deformation twinning and omega transformation in tantalum and tantalum–tungsten alloys. *Acta Mater.*, 48(20):4851–4865, December 2000. ISSN 13596454. doi: 10.1016/S1359-6454(00)00287-1.

[122] Jeffrey N. Florando, Nathan R. Barton, Bassem S. El-Dasher, et al. Analysis of deformation twinning in tantalum single crystals under shock loading conditions. *J. Appl. Phys.*, 113(8):083522, 2013. ISSN 00218979. doi: 10.1063/1.4792227.

[123] B Pang, I Jones, Y Chiu, et al. Orientation dependence of shock induced dislocations in tantalum single crystals. *J. Phys. Conf. Ser.*, 522:012029, June 2014. ISSN 1742-6588. doi: 10.1088/1742-6596/522/1/012029.

[124] C.H. Lu, B.A. Remington, B.R. Maddox, et al. Laser compression of monocrystalline tantalum. *Acta Mater.*, 60(19):6601–6620, November 2012. ISSN 13596454. doi: 10.1016/j.actamat.2012.08.026.

[125] C.H. Lu, B.A. Remington, B.R. Maddox, et al. Laser compression of nanocrystalline tantalum. *Acta Mater.*, 61(20):7767–7780, December 2013. ISSN 13596454. doi: 10.1016/j.actamat.2013.09.016.

[126] X D Dai, Y Kong, J H Li, and B X Liu. Extended Finnis–Sinclair potential for bcc and fcc metals and alloys. *J. Phys. Condens. Matter*, 18(19):4527–4542, May 2006. ISSN 0953-8984. doi: 10.1088/0953-8984/18/19/008.

[127] E M Bringa, K Rosolankova, R E Rudd, et al. Shock deformation of face-centred-cubic metals on subnanosecond timescales. *Nat. Mater.*, 5(10):805–9, October 2006. ISSN 1476-1122. doi: 10.1038/nmat1735.

[128] Diego Tramontina, Paul Erhart, Timothy Germann, et al. Molecular dynamics simulations of shock-induced plasticity in tantalum. *High Energy Density Phys.*, 10:9–15, March 2014. ISSN 15741818. doi: 10.1016/j.hedp.2013.10.007.

[129] Robert E Rudd, A. J. Comley, James Hawreliak, et al. Theory and simulation of 1D TO 3D plastic relaxation in tantalum. volume 1379, pages 1379–1382, 2012. ISBN 9780735410060. doi: 10.1063/1.3686538.

[130] Sven Herrmann, Sébastien Boutet, Brian Duda, et al. CSPAD-140k: A versatile detector for LCLS experiments. *Nucl. Instruments Methods Phys. Res. Sect. A Accel. Spectrometers, Detect. Assoc. Equip.*, 718: 550–553, August 2013. ISSN 01689002. doi: 10.1016/j.nima.2013.01.057.

[131] Justin S Wark, Andrew Higginbotham, Despina Milathianaki, and Arianna Gleason. Combined Hydrodynamic and Diffraction Simulations of Femtosecond X-ray Scattering from Laser-Shocked Crystals. *J. Phys. Conf. Ser.*, 500(15):152016, May 2014. ISSN 1742-6596. doi: 10.1088/1742-6596/500/15/152016.

[132] Paul G Stubley, Justin S Wark, and Andrew Higginbotham. Simulations of the Inelastic Response of Silicon to Shock Compression. *Paper in Preparation.*

[133] Jon T. Larsen and Stephen M. Lane. HYADES—A plasma hydrodynamics code for dense plasma studies. *J. Quant. Spectrosc. Radiat. Transf.*, 51(1-2):179–186, January 1994. ISSN 00224073. doi: 10.1016/0022-4073(94)90078-7.

[134] Bertram Alexander Auld. *Acoustic fields and waves in solids.* 1973.

[135] E Orowan. Problems of plastic gliding. *Proc. Phys. Soc.*, 52(1):8–22, January 1940. ISSN 0959-5309. doi: 10.1088/0959-5309/52/1/303.

[136] Y. Horie. Numerical Integration of Plane Elastic-Relaxing Plastic Shock Waves by a Two-Step Method. *J. Appl. Phys.*, 40(13):5368, 1969. ISSN 00218979. doi: 10.1063/1.1657396.

[137] H.L. Chang. Analysis of plane shock structures in 606-T6 aluminum. *J. Appl. Phys.*, 43(8):3362, 1972. ISSN 00218979. doi: 10.1063/1.1661720.